The possibility of hybridizing collective electronic motion with mid-infrared photons in so-called surface polaritons has redefined the limit for nano-optical circuitry. In graphene, surface polaritons have been extensively studied as they provide a link between electronic motion and light, leading to strong light-matter coupling with extreme light confinement. To achieve ultrafast polaritonic logic, surface plasmons have been successfully modulated in gapless graphene. The absence of a finite bandgap, however, inhibits good switching contrast.

In this thesis, the femtosecond photo-activation of a hybrid interface polariton is observed in real space, for the first time. The polariton is created in custom-tailored black phosphorus/silicon dioxide heterostructures, where the semiconductor black phosphorus features key advantages for ultrafast switching. Using a worldwide unique ultrafast near-field microscope, the polariton is traced in real space and frequency during a complete switching cycle. Intriguingly, the energy and momentum of the polariton remain almost constant throughout this time, which is a very favorable property for future device integration. This is in stark contrast to the behavior of pure surface plasmon polaritons, where a distinct change of the dispersion due to carrier recombination is expected. The unusual dispersion of the investigated heterostructure originates from the coupling of surface plasmon polaritons in black phosphorus to surface phonon polaritons in the surrounding silicon dioxide. From this hybridization the novel phonon-plasmon polariton mode originates, which inherits the high tunability of its plasmonic part and the long propagation distances of the phononic contribution.

Finally, the advantages of the hybrid mode are outlined also in terms of potential device integration. In this context, the potential of two other material systems for future opto-electronic devices is elucidated. The strain-tailored, prototypical phase change material vanadium dioxide might serve as a future information storage and the protected surface states of topological insulators could lead to polariton logic with strongly reduced damping.

Cover: An optical near field (golden vortex) launches polaritons (waves) at the interface between silicon dioxide (top) and black phosphorus (bottom). The distortion of the silicon dioxide atoms visualizes the interacting phonons in the material.

Universität Regensburg
Institut für Experimentelle und Angewandte Physik
Lehrstuhl Prof. Dr. Rupert Huber

Markus A. Huber

Femtosecond mid-infrared nanoscopy of photo-activated interface polaritons

Markus A. Huber

Femtosecond mid-infrared nanoscopy of photo-activated interface polaritons

Femtosecond mid-infrared nanoscopy of photo-activated interface polaritons

Dissertation
zur Erlangung des Doktorgrades der Naturwissenschaften
(Dr. rer. nat.)
der Fakultät für Physik der Universität Regensburg

vorgelegt von
Markus Andreas Huber
aus Tegernsee
im Jahr 2018

Das Promotionsgesuch wurde eingereicht am: 16.01.2018.
Die Arbeit wurde angeleitet von: Prof. Dr. Rupert Huber.

Prüfungsausschuss:	Vorsitzender:	Prof. Dr. Klaus Richter
	1. Gutachter:	Prof. Dr. Rupert Huber
	2. Gutachter:	Prof. Dr. Tobias Korn
	weiterer Prüfer:	Prof. Dr. Franz J. Gießibl

Contents

Chapter 1

Introduction

For the great [...] is a succession of little things that are brought together.

— Vincent Van Gogh [Gog82]

Solids consist of an enormous density of charged particles ($\approx 10^{23}\,\mathrm{cm}^{-3}$), which all interact via the Coulomb force. As a consequence, one of the omnipresent principles in solid state physics is the fact that the dynamics of individual elementary constituents often entails collective motion. Famous representatives of this effect are, for example, the coupled oscillation of quasi-free electrons in a solid – a so-called plasmon – or the vibrational modes of the atomic lattice – the so-called phonons.

These oscillations are often accompanied by a local imbalance in the charge density leading to a transient polarization of the material. Such a polarization can be detected and also controlled by an external electromagnetic field (i.e. light), which directly couples to this local charge imbalance. As a consequence of this interaction, new fascinating light-matter modes can emerge – so called polaritons [Kit96]. Intriguingly, such an interaction does not only appear when light passes through a solid, but it can also lead to an excitation that exists solely at the surface of the material, with a vanishing extension inside. These light-matter-coupled modes are called surface polaritons and propagate only along the surface of the material. Their unique composition of charge oscillations in the material with the external light field allows one to combine the virtues of both worlds: The light part leads to a high

polariton propagation velocity, whereas the matter part induces a strong confinement of the radiation field [Bas16]. Due to the trapping of the electric field on a length scale much smaller than the free space wavelength, the local electric field is strongly enhanced, which amplifies light matter coupling and can ultimately be used for strong-field physics on the nanoscale. As a result, surface polaritons hold great potential for strong light absorption [Rod15], optoelectronic devices [Bar03] and sensing applications [Ank08]. Studying these modes also allows one to learn about the dielectric function and hence the conductivity of the material, which constitutes the matter part.

Experimentally, the confinement of light to the nanoscale happens naturally at interfaces between materials with opposite signs of their dielectric functions. Prime examples are surface plasmon polaritons on metals [Sch10]. Here, the quasi-free electrons in the material form a plasma, which can couple to an external light field. Owing to the high carrier density in a metal, the characteristic plasma frequency resides in the visible or ultraviolet spectral range [Mai07], meaning that the electrons can respond approximately in phase with the external field up to this frequency. This leads to a negative real part of the dielectric function for all frequencies below the plasma edge. In this regime surface plasmon polaritons can form. Historically, surface plasmon polaritons hosted in gold particles have been used technologically for centuries to produce, for example, colorful windows [Bro03] or the famous Lycurgus Cup [Leo07]. However, the physical origins of the phenomena have only been discovered in the beginning of the 20th century [Mie08] and are still subject to intense research [Pel08].

Due to the intrinsically high carrier density in metals, tuning the properties of surface plasmon polaritons by influencing the carrier density is challenging. Yet, this would be of importance for future applications, where one wants to tailor the properties of the polaritons or, ultimately, selectively switch surface plasmon polaritons on and off, like one does with electric currents in a conventional transistor or logic element. So far, surface plasmon polaritons on metals have unfortunately only been modulated in the one-digit percent range by using femtosecond laser pulses to disturb their propagation [Mac09]. A further impediment for polaritonic devices made of metals is the limited polariton propagation distance due to dissipative losses. This is the

reason for current advances towards active metamaterials to reduce such damping in metal nanostructures [Hes12].

In response to the drawbacks of metal plasmonics, one focus of polaritonic research in recent years has become mid-infrared surface polaritons in the newly discovered class of two-dimensional van der Waals layered materials [Low17, Bas16]. As bulk crystals these materials are composed of individual two-dimensional layers, which are only bound by weak van der Waals forces. Hence, they can be exfoliated down to the monolayer limit, yielding a sample that is only a single to a few atoms in height [Nov05, CG14a]. Many different types of materials have been found, ranging from insulators, to semiconductors, to the semimetal graphene [Xia14]. Since none of these materials feature dangling bonds at their surface, they are prime candidates to build heterostructures. Such atomically precise heterostructuring can be used to tune the properties of individual layers [Ste18], or even combine the assets of different materials [Nag17], with the ultimate goal being to create three-dimensional heteromaterials with entirely new properties [Gei13].

Especially graphene and its heterostructures have attracted immense attention for polaritonic control, as it can easily be doped by electrostatic gating, features large mobilities, has a Dirac-like electron dispersion relation and hosts strongly confined surface plasmon polaritons with long polariton propagation distances [Low14a]. In pioneering work, G. X. Ni and coworkers demonstrated that it is even possible to tune the surface plasmon polariton dispersion by modulating the carrier density in graphene over ultrafast timescales using a femtosecond pump laser [Ni16]. The laser pulses heated the carrier distribution and led to a change of the polariton dispersion that they could trace spectrally. On the other hand, the absence of a bandgap in graphene made it difficult to obtain a high switching contrast between the on and off state of the surface plasmon polaritons [Bas17].

In this work, I will introduce the new two-dimensional material black phosphorus to study surface plasmon polaritons and show the first real-space movie of an actively switched polariton mode on ultrafast timescales [Hub17]. Black phosphorus features a tunable direct bandgap [Lin15] and thus carriers can be photo-injected to reach a state where it supports a surface plasmon polariton mode in the mid-infrared spectral range.

Experimentally, this mode is characterized using ultrafast mid-infrared near-field microscopy - a technique that has been developed contemporaneously in our group [Eis14, Hub16] and the group of D. N. Basov [Wag14b, Wag14a]. We use near-infrared pump lasers to excite the black phosphorus and probe its local conductivity with ultrashort mid-infrared pulses, thereby resolving nanoscale phenomena on ultrashort timescales. Furthermore, the use of near-field microscopy is perfectly suited to study polaritons in real space [Che12, Fei12] as the sharp metallic tip of the setup provides the necessary momentum to launch and image these strongly confined surface modes. Sample heterostructuring is used to create a structure composed of black phosphorus in combination with silicon dioxide, which features a strong phonon in the same spectral range where the surface plasmon polariton exists. This phonon can also couple to mid-infrared radiation to form a surface phonon polariton. From the interplay of these two different dipole oscillations a new hybrid surface phonon-plasmon polariton is created with the advantages of both its constituents: The high quality factor of the surface phonon polariton leads to a long propagation distance for the hybrid mode of several micrometers, while the switchable character of the surface plasmon polariton is also imparted onto the hybrid mode. Furthermore, the hybrid mode is strongly confined in energy and momentum, making it an ideal candidate for future polaritonic switching devices.

For a thorough interpretation of the measured data, the basis of surface polaritons is reviewed in chapter 2 and a numerical way of calculating the dispersion of surface polaritons is shown (section 2.1.1). This technique is used to discuss the properties of surface plasmon polaritons (section 2.1.2) and surface phonon polaritons (section 2.1.3), the constituents of the investigated hybrid mode. Subsequently, the control of surface polaritons is outlined (section 2.2) in the context of near-field microscopy experiments, which are used to visualize these bound surface modes. Next, black phosphorus – our material of choice for ultrafast surface polariton switching – is discussed, with particular attention paid to its unique properties (section 2.3).

Armed with a theoretical description of surface polaritons from chapter 2, the experimental observations are presented in chapter 3, starting with a characterization of the custom tailored heterostructures (section 3.1), then directly moving towards the real-space observation of a switchable polariton (section 3.2). We trace the evolu-

tion of the mode and determine its switch-on time in section 3.3. Here a strong and unexpected confinement of the momentum distribution of the polariton is seen. To unravel the origin of this confinement and learn about the composition of the mode, its spectral signature is investigated (section 3.4). The results are explained in a straightforward model (section 3.5.1), which gives a good qualitative understanding but lacks quantitative agreement. Therefore a more sophisticated approach is chosen to explain the effects of the sample thickness on the polariton dispersion (section 3.5.2) and simulate the modes hosted by the structure (section 3.5.3). The model provides new insights into how the mode evolves for increasing levels of pump excitation fluence, which are verified in the experiment.

As further corroboration of the validity of the model, the full dispersion of the mode is measured experimentally for the relevant frequency range in section 3.6. With the new understanding gained from the studies described above, we return to characterize one of the most exceptional properties of the hybrid mode – its long propagation length. The data can be fit with a nominally undamped propagation over several micrometers. To underpin these observations, the imaginary in-plane momentum of a pure phonon polariton, which governs the damping, is calculated and compared to the experimental data (section 3.7). From the propagation length, the polariton lifetime can be estimated. The lifetime of the mode and the lifetime of the carriers lead to an interesting dynamical process which is absent in steady-state measurements and will be described with a straightforward oscillator model in section 3.8. It can even result in plasmon amplification in principle, but it will be shown that for the hybrid mode observed in this thesis this effect does not occur. Furthermore, the section addresses the theoretical difference between the damping rates of the hybrid mode and a pure plasmon polariton.

In the experiment, the observed polariton is not hybridized in the region outside the silicon dioxide Reststrahlen band. Therefore, we study the bare surface plasmon polariton at lower probe frequencies (section 3.9) to support the predictions of section 3.8.

Before concluding, the perks of the hybrid switchable mode are discussed in terms of potential device integration (chapter 4). In the same discussion other potentially complementary approaches towards polariton devices are described. Special focus is

put on phase change materials and topological insulators. Phase change materials might serve as potential candidates for persistent storage of information. In vanadium dioxide nanostructures strain plays an essential role in tailoring the switching susceptibility of the material. In section 4.1 it is shown how near-field microscopy can be used to predict the switching susceptibility on a single wire [Hub16].

Another pathway towards hybrid modes which can be optically controlled is based on topological insulators. This new class of materials features Dirac fermions in protected surface states where backscattering is prohibited. These states should support plasmon polaritons with exceptional propagation lengths. Furthermore, the material is semiconducting in the bulk. This allows for a direct excitation of free carriers in the bulk, which can influence the surface states, allowing for ultrafast control of the surface polaritons. Initial measurements on three dimensional topological insulators are shown, demonstrating that near-field microscopy is able to differentiate the quality of samples on the nanoscale. Large-scale inhomogeneities are seen across the samples, indicating that techniques with nanoscale spatial resolution like near-field microscopy are essential for resolving important features that do not show up in pure topographic imaging (section 4.2).

Chapter 5 contains a short summary of the experimental findings and the exciting properties of the hybrid polariton mode.

Chapter 2

Surface polaritons and the assets of black phosphorus for polariton photo-activation

When light with its linear dispersion couples to a material which offers a dipole resonance at a certain frequency, there is an avoided crossing behavior between the bare dispersion curves leading to a new combined dispersion of the system (Fig. 2.1). The polar excitation in the material is typically a quasiparticle, e.g. a phonon, plasmon or exciton [Low17, Bas16]. The combined excitation itself is also a quasiparticle with bosonic character. Depending on the matter resonance, the name of the polariton is adapted: A hybrid of a photon and a plasmon, for example, is called a plasmon polariton.

Furthermore, there are special excitations appearing at the surface of materials with a strong quasiparticle resonance, which are called surface polaritons. These propagating surface modes show intriguing effects, which make them interesting for scientific studies as well as technological applications. Owing to their light part, they feature a high phase velocity – much higher than typical drift velocities in conventional electronics. Hence, they can be used for future ultrafast information transfer and – if the polariton can be tuned – signal processing. Furthermore, due to the strong resonant behavior at the level crossing point, the dispersion curves off strongly from the free space light line, which leads to polaritons with high values of in-plane momentum [Nov06, Mai07]. Accordingly, the polariton wavelength, which goes inversely proportional to the wavevector, is strongly decreased, leading to a

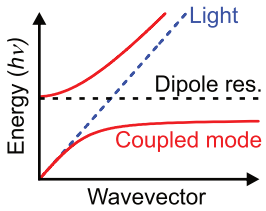

Figure 2.1. | Sketch of light-matter coupling. In the dispersion diagram, the coupling of light (blue dashed line) and a dipole resonance in a material (black dashed line) lead to new light-matter-coupled modes (red lines), which show an anticrossing behavior.

strong confinement of the light to a short length scale. As a result, the local electric field of the polariton is strongly enhanced - a trait that is very useful for sensing applications [Rod15] and also superlensing [Feh15], where the high fields increase the detectivity of a device.

From a material point of view, a big leap in polaritonic research was made with the discovery of graphene [Nov05] and the class of two-dimensional materials that followed soon after. These single atomic layers provided the perfect matrix for the ultimate limit of surface polaritons. Especially the semi-metal graphene with its Dirac-like dispersion has led to a plethora of publications investigating surface plasmon polaritons [Che12, Fei12, Bas16, Low17, Gri12]. Its appeal was the easy tunability of the Fermi level and thus dispersion relation of the polariton in the mid-infrared spectral range.

Additionally, the weak coupling to adjacent layers in the whole class of van der Waals bonded materials allows one to easily form heterostructures of different materials and thus tailor the dielectric surroundings of the polaritonic layer. It was found, for example, that the encapsulation of graphene in hexagonal boron nitride greatly improved the polariton propagation length [Woe15]. Furthermore, this approach was used to create new polaritonic hybrids, where instead of a single resonance in one material forming a polariton, multiple excitations that existed in different layers (but at the same energy) combined to form more complicated light-matter polaritons whose properties were different from those of their uncoupled polariton counterparts [Cal16, Dai15]. Recently, other exotic polaritons such as acoustic plasmon polaritons [AG16] and hyperbolic polaritons [Dai15, Nik16, Yox15] have also been found.

The most prominent excitations coupling to mid-infrared light at the surfaces of these two-dimensional materials are plasmons and phonons. Therefore, we will

briefly review the theoretical details of surface polaritons and then investigate the dispersion relations of surface plasmon polaritons and surface phonon polaritons.

2.1. Surface polaritons

Surface polaritons are bound solutions of Maxwell's equations that can appear at the interface of materials with different dielectric functions ε_1 and ε_2. The relative permeability in both media is assumed to be unity ($\mu_1 = \mu_2 = 1$), which is a good description of the materials studied in this work, as they are non-magnetic. The electric field distribution $\vec{E}(\vec{r}, \omega)$ of the polaritons fulfills the wave equation

$$\nabla \times \nabla \times \vec{E}(\vec{r}, \omega) - \frac{\omega^2}{c^2} \varepsilon_{\mathrm{i}}(\omega) \vec{E}(\vec{r}, \omega) = 0 \tag{2.1}$$

where c is the speed of light. To simplify the solution, we assume a preferential axis along which the polaritons will propagate and define it as the x-axis. The axis perpendicular to the interface will be z and the interface will be positioned at $z = 0$, leading to halfspaces with dielectric function of either ε_1 or ε_2 (see Fig. 2.2a). Furthermore, the dielectric functions should be isotropic and only depend on the frequency. In this work, ν always denotes the frequency and $\omega = 2\pi\nu$ is used when referring to the angular frequency.

To solve the equation, we can use an ansatz similar to the reflection of an electromagnetic plane wave at an interface (see Fig. 2.2b). To account for the propagation direction and the direction of possible exponential damping for the chosen coordinate system correctly, all k-vectors (k, k_x, $k_{z,\mathrm{i}}$) are defined as being of the form $k_\triangle = \alpha_\triangle + i\beta_\triangle$, with $\alpha_\triangle > 0$ and $\beta_\triangle > 0$. The defining properties of a surface polariton mode are its propagation along the interface between medium one and two and its exponential decay perpendicular to it (Fig. 2.2a). For the chosen k-vector convention, it is easy to see that such an exponential decay away from the interface is only possible for the "reflected" wave (sketched by the ray with $-k_{z,1}$ in Fig. 2.2b) and the "transmitted" wave (given by the ray with $k_{z,2}$ in Fig. 2.2b). Therefore the "incident" wave (dashed line in Fig. 2.2b) is not needed for the description of the surface polariton field distribution, leading to only one plane wave in each material.

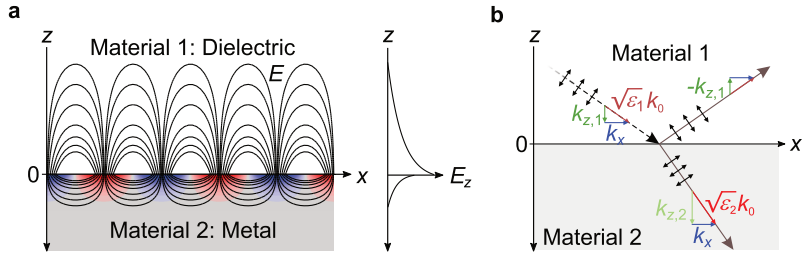

Figure 2.2. | Sketch of surface polaritons. **a)** Field distribution of a surface polariton at the interface of a dielectric material and a metal. Plotted are the electric field lines (black) and the areas of high (red) and low (blue) carrier concentration. The fields decay exponentially in z-direction away from the interface. **b)** Sketch of a ray of p-polarized light going across the boundary between two materials, including a reflected wave. Shown are the wavevectors of the incident, the reflected and the transmitted wave ($\sqrt{\varepsilon_\mathrm{i}}\,\omega/c = \sqrt{\varepsilon_\mathrm{i}}\,k_0$, red), and their components k_x (blue) and $\pm k_{z,\mathrm{i}}$ (green). Surface polaritons appear without the existence of an incident field, which is why the incident wave is shown dashed.

A stable, bound mode at the interface for such a configuration can only be found using p-polarized electromagnetic waves. For s-polarization, the solution is not confined to the interface. As a result, the electric field distribution in material one can be described via

$$\vec{E}_1 = \begin{pmatrix} E_{x,1} \\ 0 \\ E_{z,1} \end{pmatrix} e^{ik_x x - i\omega t} e^{-ik_{z,1} z}. \tag{2.2}$$

The electric field distribution in material two is described similarly to the one in material one and only differs in the direction of propagation in z-direction

$$\vec{E}_2 = \begin{pmatrix} E_{x,2} \\ 0 \\ E_{z,2} \end{pmatrix} e^{ik_x x - i\omega t} e^{ik_{z,2} z}. \tag{2.3}$$

The wavevector k_x must be conserved at the interface for both halfspaces i = 1,2. Therefore, only the z-component of the wavevector $k_{z,\mathrm{i}}$ depends on the material. To calculate $k_{z,\mathrm{i}}$, we can insert equation 2.2 (for i = 1) and 2.3 (for i = 2) into the wave

equation (2.1). Using the free space wavevector $k_0 = \omega/c$, we obtain the following equation for $k_{z,\mathrm{i}}$ in each halfspace:

$$k_x^2 + k_{z,\mathrm{i}}^2 = \varepsilon_{\mathrm{i}}(\omega) k_0^2 = \varepsilon_{\mathrm{i}}(\omega) \frac{\omega^2}{c^2}. \tag{2.4}$$

Furthermore, Maxwell's equations lead to three conditions, which must be fulfilled for the surface waves. Firstly, the electric fields in our scenario are source-free. Hence, the divergence of the electric displacement field in each halfspace (i $\in \{1,2\}$) must vanish:

$$\nabla \cdot \vec{D}_{\mathrm{i}} = \nabla \cdot \varepsilon_0 \varepsilon_{\mathrm{i}} \vec{E}_{\mathrm{i}} = 0, \qquad \mathrm{i} = 1, 2, \tag{2.5}$$

where ε_0 is the permittivity of free space. Inserting the chosen ansatz of the electric field in each halfspace (equations 2.2 and 2.3) yields

$$\begin{aligned} E_{z,1} &= \frac{k_x}{k_{z,1}} E_{x,1} \\ E_{z,2} &= -\frac{k_x}{k_{z,2}} E_{x,2}. \end{aligned} \tag{2.6}$$

Secondly, the parallel component of the electric field at the boundary must be conserved:

$$\vec{E}_1^{\parallel} = \vec{E}_2^{\parallel} \leftrightarrow E_{x,1} = E_{x,2}. \tag{2.7}$$

Finally, the perpendicular component of the electric displacement fields at the boundary must be continuous, which leads to

$$\vec{D}_1^{\perp} = \vec{D}_2^{\perp} \leftrightarrow \varepsilon_1(\omega) E_{z,1} = \varepsilon_2(\omega) E_{z,2}. \tag{2.8}$$

From this set of equations (2.6 to 2.8) one obtains two solutions. One solution requires $k_x = 0$ and is, therefore, not physically relevant for an excitation traveling along the interface. The other solution leads to

$$\varepsilon_1(\omega) k_{z,2} + \varepsilon_2(\omega) k_{z,1} = 0 \tag{2.9}$$

and can be used in conjunction with equation 2.4 to calculate a dispersion relation

between the in-plane wavevector k_x and the angular frequency ω:

$$k_x(\omega) = \sqrt{\frac{\varepsilon_1(\omega) \cdot \varepsilon_2(\omega)}{\varepsilon_1(\omega) + \varepsilon_2(\omega)}}\, k_0. \tag{2.10}$$

Additionally, an expression for the normal component k_z is found:

$$k_{z,\mathrm{i}} = \pm \frac{\varepsilon_{\mathrm{i}}(\omega)}{\sqrt{\varepsilon_1(\omega) + \varepsilon_2(\omega)}}\, k_0. \tag{2.11}$$

Here, the $\pm$ sign must be chosen such that each $k_{z,\mathrm{i}}$ is positive in its real and imaginary part to obey the initially imposed constraints. As a result of the two positive $k_{z,\mathrm{i}}$, the dielectric functions of material one and two must have opposite signs, to fulfill equation 2.9.

Furthermore, reconsidering the prerequisites for a surface polariton, namely a traveling wave along an interface, which decays exponentially perpendicular to the boundary, the range of available k-vectors can be limited to the ones with non-vanishing k_x and purely imaginary $k_{z,\mathrm{i}}$ values. From these considerations it is obvious that, for a 'typical' dielectric material in the upper halfspace (Fig. 2.2a) with positive real part and negligible imaginary part of the dielectric function, strong limitations on the dielectric function of material two are imposed:

$$\begin{aligned} \varepsilon_1(\omega) \cdot \varepsilon_2(\omega) &< 0 \\ \varepsilon_1(\omega) + \varepsilon_2(\omega) &< 0. \end{aligned} \tag{2.12}$$

Generally, the real part of the dielectric function of material two needs to be negative and larger in absolute magnitude than the corresponding real part of the dielectric function of material one. This happens around resonances of the material, for example plasma oscillations, phonon vibrations or excitonic resonances (for more exotic excitations, also see [Bas16]). In the black phosphorus/silicon dioxide (SiO_2) structures investigated in this work, the relevant processes are plasma oscillations of the photo-doped black phosphorus as well as phonon resonances in the polar SiO_2 layers. However, before discussing these polaritons in greater detail, a short digression is made to show how the dispersion relations of such polaritons can be calculated numerically, a concept which can later be expanded to more complicated structures.

2.1.1. Calculating polariton dispersions numerically

We have seen that the dispersion relation for bound surface polaritons can be obtained analytically from Maxwell's equations. However, we needed to make some assumptions (e.g. that one material is a dielectric with no imaginary part in the dielectric function) and the situation gets even more complicated when the real physical system consists of more than two layers. Therefore, in the literature a different approach is used to extract the dispersion of surface polaritons. Namely, the Fresnel reflection coefficient of the system serves as an indicator for dielectric resonances. For surface polaritons, this works particularly well because of the correlation between the reflection coefficient and the characteristic equation, which defines the existence of the polariton (equation 2.9). We have seen in the previous section, that the ansatz to calculate the polaritons can be seen as analogous to the reflection of a *p*-polarized wave at an interface – only without the incident wave. Incorporating, the incident wave into the ansatz by modifying the electric field in material one to

$$\vec{E}_1 = \begin{pmatrix} E_{x,1} \\ 0 \\ E_{z,1} \end{pmatrix} e^{ik_x x - i\omega t} \left(e^{ik_{z,1} z} + r_\mathrm{p} e^{-ik_{z,1} z} \right), \tag{2.13}$$

where r_p denotes the reflection coefficient, one can use equations 2.5, 2.7 and 2.8 to solve for the reflection coefficient r_p. Following a calculation similar to the one we have performed in the previous section, we find a formula for the Fresnel reflection coefficient for *p*-polarized light

$$r_\mathrm{p} = \frac{\varepsilon_2 k_{\mathrm{z},1} - \varepsilon_1 k_{\mathrm{z},2}}{\varepsilon_2 k_{\mathrm{z},1} + \varepsilon_1 k_{\mathrm{z},2}}. \tag{2.14}$$

Comparing this equation with the characteristic equation of a surface polariton (equation 2.9)

$$\varepsilon_1(\omega) k_{z,2} + \varepsilon_2(\omega) k_{z,1} = 0, \tag{2.15}$$

we see that the reflection coefficient diverges at the position in (k,ω)-space, where a surface polariton mode exists. This can also be understood intuitively, when comparing the two mathematical approaches. The surface polariton has been described using a field distribution, which decays exponentially as a function of distance per-

pendicular to the interface. We, therefore, removed the field that has a k_z component corresponding to an incident wave. However, we kept a field that has the same k_z direction as the reflected wave in the deduction of the Fresnel reflection coefficient. This means, that there is a reflected wave without incident field. Since the reflection coefficient can also be described as the ratio between reflected and incident field amplitude

$$r_{\mathrm{p}} = \frac{E_{\mathrm{reflected}}}{E_{\mathrm{incident}}}, \tag{2.16}$$

we see that this quantity must diverge for a finite reflected field and zero incident field. For this reason, false color plots of the imaginary part of r_{p} as a function of frequency and in-plane wavevector k_x are a common means in the near-field community to visualize the dispersion of polaritonic modes in complex systems (see e.g. Refs. [Fei11, Che12, Dai15]). The advantage of this approach lies in the fact that the reflection coefficient can be calculated numerically in a straightforward way from the dielectric functions of the different layers for multi-layered systems using a transfer matrix method (see appendix B). The imaginary part is used for aesthetic reasons. The resonance at the position of the surface polariton leads to a divergence with a sign change in the real part of the Fresnel reflection coefficient, which makes the local surrounding of the resonance show very high function values. For complex dielectric functions (i.e. including damping) a zero crossing along the dispersion of the polariton appears. On the other hand, since r_{p} is a physical function that describes the reflection of a wave, it must obey causality and, hence, fulfill the Kramers-Kronig relations. For this reason, the imaginary part of r_{p} shows the characteristic peak at the resonance positions of the surface polariton. Tracing this maximum allows one to visualize the dispersion of the surface polariton more clearly than in the real part of r_{p}.

In the following, this type of visualization will be used to show the dispersion of surface bound modes in different systems, including the full silicon dioxide/black phosphorus heterostructure. For models that have an analytical solution, it will also be visible that the maxima in the imaginary part of the Fresnel reflection coefficient overlap perfectly with the analytical solutions. Plots of the real part are omitted in this thesis because they do not contribute additional information about the dispersion of the surface polariton mode. Nevertheless, there are two

interesting other modes that I want to address here shortly, which are characterized by a particular value in the real part of the Fresnel reflection coefficient (i.e. $r_\mathrm{p} = 0$ and $r_\mathrm{p} = 1$).

The first one is the **Brewster mode** [Bro82]. It is characterized by the positions in frequency and k_x, where r_p goes to zero. The dispersion of this mode can be calculated using the same approach as in the previous section. However, as ansatz for the electric field distribution in material one the vector-field given in equation 2.13 has to be used, where r_p is set to zero. One can easily see, that the electric field distribution in material one is then very similar to the one of the previous section (equation 2.2), only with opposite propagation direction. That means, we have an incident field and a transmitted field, however, no reflected field. Solving the problem, yields exactly the same equation for the k_x-vector of the Brewster mode as the one for a surface polariton (equation 2.10, [Fan41]). The difference appears in the $k_{z,\mathrm{i}}$-vectors, which now have the same sign to show the correct propagation direction. As a result, this mode only appears in places where the the dielectric functions of both materials have the same sign.

Furthermore, the excitation of (bulk) **polaritons** is possible [Kit96]. The dispersion of these propagating modes is given by the free space dispersion modified by the refractive index of material two $n_2 = \sqrt{\varepsilon_2}$:

$$k_\mathrm{P} = \sqrt{\varepsilon_2}\,\frac{\omega}{c} = \sqrt{\varepsilon_2}\,k_0. \tag{2.17}$$

Since polaritons are not surface bound modes, the k_x and k_z components of the polariton wavevector k_P can assume various real values, depending on the angle of incidence. As a result, polaritons occupy a region rather than a line in the (k_x, ν)-dispersion diagrams shown in this thesis. The low-k_x-vector limit is $k_x = 0$ and the high-k_x boundary is given by $k_x = k_\mathrm{P}$ (i.e. $k_{z,2} = 0$). At the latter boundary r_p goes to unity since it corresponds to the angle from which on total internal reflection appears. In this work, this characteristic line with $r_\mathrm{p} = 1$ will be labeled upper polariton boundary in the dispersion diagrams.

In the next two sections we discuss these modes for two special cases. We will look at an interface from air to a material, whose dielectric response is once determined by the motion of free charge carriers and once by polar phonons.

2.1.2. Surface plasmon polaritons

Calculating the imaginary part of the Fresnel reflection coefficient provides a useful tool to visualize different types of surface polaritons (e.g. surface plasmon polaritons, surface phonon polaritons, ...). The only necessary ingredient is the frequency dependent dielectric function for each type. In the case of a surface plasmon polariton, a dielectric function is needed that describes the interaction of the light field and the plasma response of a material - the collective motion of free charge carriers.

In the Drude-Sommerfeld description [Dru00], the motion of a single particle with charge q and mass m is assumed to be free apart from the force it acquires from the driving electric field $E(t)$ and an additional phenomenological damping term with damping rate γ, which accounts for energy loss from various effects (e.g. inelastic scattering at impurities or phonons). The equation of motion for a driving electric field with amplitude E_0 and angular frequency ω is then given by

$$m\ddot{x}(t) - m\gamma\dot{x}(t) = qE(t) = qE_0e^{i\omega t}. \tag{2.18}$$

The ansatz of a complex exponential function for $x(t)$ leads to a periodic oscillation of the particle along the axis of the electric field polarization. The collective dipole oscillation of N particles in the material creates an effective polarization $P(t) = N \cdot q \cdot x(t)$, which responds to the external light field in an analogous way to a classical driven harmonic oscillator. Using the identity $D(t) = \varepsilon_0 E(t) + P(t) = \varepsilon_0 \varepsilon_\mathrm{r} E(t)$ for the dielectric displacement field $D(t)$ yields an analytical expression for the dielectric function of a material with a plasma resonance:

$$\varepsilon_\mathrm{r}(\omega) = 1 - \frac{Nq^2}{\varepsilon_0 m} \cdot \frac{1}{\omega^2 + i\gamma\omega} \tag{2.19}$$

$$= 1 - \frac{\omega_\mathrm{Pl}^2}{\omega^2 + i\gamma\omega}. \tag{2.20}$$

Here, the plasma angular frequency $\omega_\mathrm{Pl} = \sqrt{Nq^2/\varepsilon_0 m}$ was introduced as a parameter to combine the sometimes unknown quantities of N, q and m, leading to only two free parameters (ω_Pl and γ). The characteristic shape of the resulting dielectric

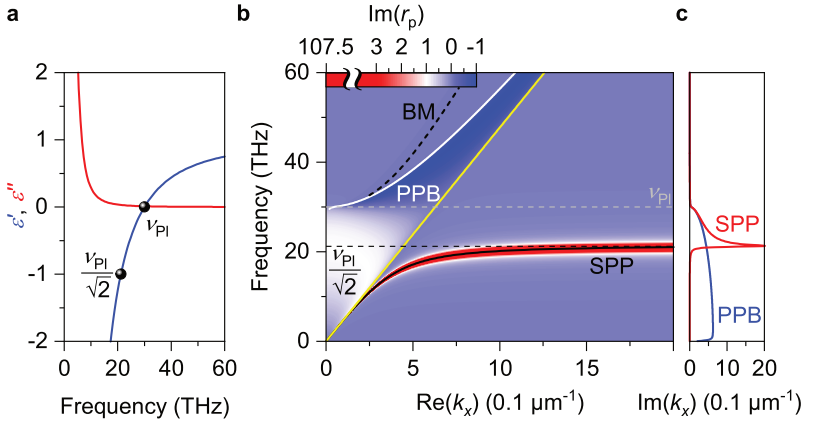

Figure 2.3. | Plasmon polaritons and the surface plasmon polariton. **a)** Real part ε' (blue) and imaginary part ε'' (red) of an example Drude dielectric function. The plasma frequency ν_{Pl} is chosen to be 30 THz and the scattering rate γ is 2 THz. Black spheres mark the function values of ε' at the plasma frequency ν_{Pl} and $\nu_{\mathrm{Pl}}/\sqrt{2}$. **b)** The imaginary part of the Fresnel reflection coefficient is color-coded as a function of in-plane wavevector k_x and frequency for an interface from air to a material with the dielectric function given in **a**. The color plot is overlaid with the analytically obtained lines for the surface plasmon polariton (SPP, black solid), the Brewster mode (BM, black dashed) and the upper boundary for plasmon polaritons (PPB, white). The free space light line is shown in yellow. **c)** To visualize regions of high damping of the modes the imaginary part of the propagation wavevector k_x of the SPP (red) and bulk polaritons at the PPB (blue) are plotted for different frequencies.

function is shown in Fig. 2.3a. In this work, the results are typically shown as a function of frequency ν, not angular frequency ω. The plasma angular frequency ω_{Pl} hence translates into the plasma frequency ν_{Pl} via $\nu_{\mathrm{Pl}} = \omega_{\mathrm{Pl}}/2\pi$. As is visible, the plasma frequency has a physical meaning in the system as it is exactly the frequency where the real part of the dielectric function vanishes.

The given dielectric function can now be used to calculate the imaginary part of r_{p} at an interface to air to visualize the different modes in such an idealized system dominated by free carrier motion. The result is shown in Fig. 2.3b. The value of the

imaginary part of r_p is color-coded as a function of frequency and real part of the in-plane wavevector k_x for a Drude dielectric function with a plasma frequency of 30 THz and a damping rate of $\gamma = 2$ THz. Very prominently, an anticrossing is seen where the extrema of the imaginary part of r_p curve off from the light line (yellow line, $\nu_\mathrm{Light}(k_x) = c \cdot k_x/2\pi$, where c is the speed of light in free space). The avoided frequency range reaches from $\nu_\mathrm{Pl}/\sqrt{2}$ to ν_Pl (black spheres in Fig. 2.3a highlight the real part of the dielectric function for the two frequencies). For this simple system, the dispersion of the **surface plasmon polariton** (SPP), the **Brewster mode** (BM) and the high-k_x-vector boundary for **plasmon polaritons** (PPB) can be calculated analytically and the resulting curves are plotted in black and white. All these modes are discussed separately in the next paragraphs.

The **surface plasmon polariton** is characterized by the maxima in the imaginary part of r_p. It corresponds to the solution of Maxwell's equations for one wave in each material, where the k_z-vectors are each pointing away from the interface. Following its dispersion, we see that it curves off the light line to larger k_x-vectors. This leads to a very localized electric field distribution and can be described using the model for surface polaritons introduced in section 2.1. Inserting the Drude dielectric function (equation 2.20) into equation 2.10 as ε_2 and choosing the other medium to be air (i.e. $\varepsilon_1 = 1$) results in the black curve in Fig. 2.3b. As expected, we see that the maxima of the calculated imaginary part of r_p lie along this curve. For very high k_x-vectors and a low scattering rate ($\gamma \to 0$) the surface plasmon polariton's frequency goes to $\nu_\mathrm{Pl}/\sqrt{1+\varepsilon_1}$, where ε_1 is the dielectric function of the non-Drude material. At this point the real part of the dielectric function of the Drude material equals the negative value of the dielectric function of the neighboring material (i.e. minus one for our example case of air, marked by a black sphere in Fig. 2.3a). This is consistent with the equation set 2.12, which defines that surface plasmon polaritons can only exist in regions where $\varepsilon_2(\nu) < -\varepsilon_1(\nu)$. As a result the dielectric function of medium one (ε_1) determines the splitting ratio between the upper and lower polariton branches. In Fig. 2.3c, the analytically obtained imaginary k_x-vector of the mode is plotted as a function of frequency (red line). For high values of $\mathrm{Im}(k_x)$, the mode is strongly damped. It can be seen, that the mode is practically undamped in the regions outside the avoided crossing. Inside

the area, the strongest damping appears right at the lower boundary $\nu_{\mathrm{Pl}}/\sqrt{1+\varepsilon_1}$ and decreases strongly for increasing frequencies towards the plasma frequency.

The **Brewster mode** follows the same dispersion in k_x as the surface plasmon polariton. However, the $k_{z,i}$ for this mode point in the same direction. As a result, it can only exist for frequencies, where the dielectric functions of both materials show the same sign. For a material with a Drude response and air, this condition is true for frequencies larger than the plasma frequency. In this frequency range the mode can also be plotted from the analytical formula (dashed black line in Fig. 2.3b). The imaginary part of r_{p} along the mode does not feature any extraordinary features. However, the real part of r_{p} is zero at all frequencies (not shown). The reason is, that there is no reflected wave when light hits an interface at Brewster's angle (which is determined by k_x and $k_{z,1}$). Furthermore, the k_z-vectors for this mode are not purely imaginary but have a real component leading to a propagating wave, which hits the interface and is transmitted. It is hence, not a surface bound mode.

Plasmon polaritons, on the other hand, cannot be described using the (k_x,ν)-dispersion of the surface polariton or Brewster mode. As discussed in the previous section, they occupy a region in the dispersion diagram ranging from $k_x = 0$ to $k_x = k_{\mathrm{P}}$, where the polariton wavevector k_{P} is given by the free space dispersion modified by the refractive index $n = \sqrt{\varepsilon(\nu)}$ of the Drude material (see equation 2.17):

$$\nu = \frac{ck_{\mathrm{P}}}{2\pi \cdot \sqrt{\varepsilon(\nu)}} = \frac{ck_{\mathrm{P}}}{2\pi \cdot \sqrt{1-\nu_{\mathrm{Pl}}^2/\nu^2}}. \tag{2.21}$$

For simplicity, the damping term γ has been neglected in the equation above. It is then easy to see that the polariton wavevector k_{P} is only real for frequencies above the plasma frequency. Below ν_{Pl} the wavevector is imaginary. This is also true at the upper k_x boundary for plasmon polaritons (PPB, blue curve in Fig. 2.3c) leading to a mode that is strongly damped. When considering only the region above ν_{Pl}, neglecting γ is a good approximation. The equation can be solved for ν and we obtain the dispersion of the plasmon polariton

$$\nu = \frac{1}{2\pi}\sqrt{(2\pi\nu_{\mathrm{Pl}})^2 + c^2k_{\mathrm{P}}^2}. \tag{2.22}$$

From the upper k_x-vector boundary in the figure and analytically, when solving for the polariton k-vector

$$k_{\mathrm{P}} = \frac{2\pi}{c}\sqrt{\nu^2 - \nu_{\mathrm{Pl}}^2} = \sqrt{k_0^2 - \left(\frac{2\pi\nu_{\mathrm{Pl}}}{c}\right)^2}, \tag{2.23}$$

we see, that the mode always stays at smaller wavevectors than the free space wavevector k_0 (i.e. the light line). As discussed in the previous section, the real part reaches a maximum at the upper plasmon polariton boundary - as expected for the angle between k_x and k_z that defines the starting point for total internal reflection.

2.1.3. Surface phonon polaritons

In solid state physics, phonons are the elementary excitations of a periodic, elastic lattice of atoms. In a material with differently charged atoms at different lattice sites, an oscillation of these atoms can lead to an oscillating polarization inside the material. This polarization can couple to an external light field and form polaritons.

To describe such an interaction, we can proceed analogously to the case of free carriers in the previous section. However, this time, the charged particles are the heavy atomic cores and they cannot move freely but are bound to an oppositely charged counterpart, which leads to a restoring force. Therefore, in the description of a Lorentz oscillator, an additional term of $m\omega_0^2 x$ has to be added to the equation of motion (equation 2.18). Here, ω_0 is the angular eigenfrequency of the undamped harmonic oscillation of the bound particles and m is the reduced mass of the constituents. Following the same approach as in the previous chapter, we can extract the dielectric function for a material with bound charged particles,

$$\varepsilon_{\mathrm{r}}(\omega) = 1 + \frac{\sigma^2}{\omega_0^2 - \omega^2 - i\beta\omega}, \tag{2.24}$$

where $\sigma^2 = \frac{Nq^2}{\varepsilon_0 m}$ acts similarly to the plasma angular frequency in the plasmon case. An example Lorentzian dielectric function is shown in Fig. 2.4a. The function has two physically important frequencies, which can be calculated most easily for negligible damping (i.e. $\beta \to 0$). For one, at the angular frequency ω_0 the dielectric

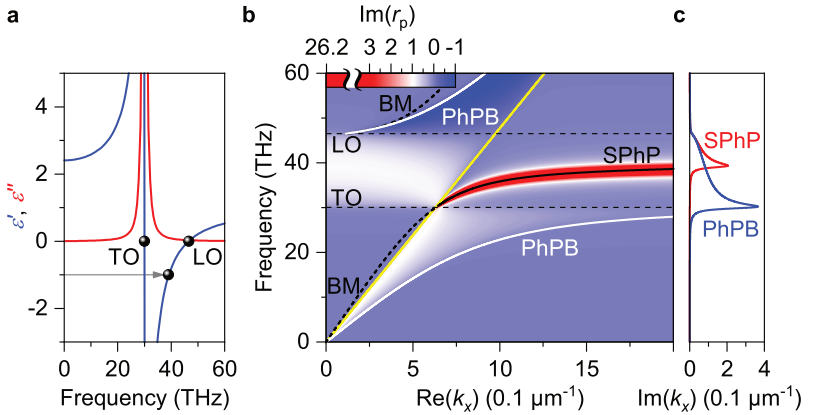

Figure 2.4. | Phonon polaritons and the surface phonon polariton. a) Real part ε' (blue) and imaginary part ε'' (red) of an example dielectric function featuring a Lorentz-type resonance. The parameters for the Lorentz curve were chosen to be $\omega_0 = 2\pi \cdot 30\,\mathrm{THz}$, $\beta = 5\,\mathrm{THz}$ and $\sigma = 2\pi \cdot 35.588\,\mathrm{THz}$. Black spheres mark the positions of ε' at the TO and LO frequencies as well as on the point, where ε' crosses minus one with a positive slope. **b)** Color-coded imaginary part of the Fresnel reflection coefficient r_p as a function of in plane wavevector k_x and frequency for an interface between air and a material with the dielectric function given in **a**. The false-color plot is overlaid with curves of the surface phonon polariton dispersion (SPhP, black solid), the Brewster mode (BM, black dashed) and the upper boundary for phonon polaritons (PhPB, white). **c)** To visualize regions of high losses for the modes, the theoretical curves of the imaginary part of the propagation wavevector k_x for the SPhP (red) and polaritons at the PhPB (blue) are plotted for different frequencies.

function diverges. This angular frequency corresponds to the transverse optical (TO) phonon resonance frequency $\nu_\mathrm{TO} = \omega_0/2\pi$ [Fox10]. When damping is included the divergence is suppressed, leading to a zero crossing of the dielectric function close to the TO phonon frequency. The second angular frequency of interest is at $\omega_\mathrm{LO} = \sqrt{\omega_0^2 + \sigma^2}$ where the dielectric function crosses zero a second time. This frequency corresponds to the longitudinal optical (LO) phonon frequency $\nu_\mathrm{LO} = \omega_\mathrm{LO}/2\pi$.

The LO and TO resonances divide the dielectric response into three frequency regimes and, analogous to the plasma resonance in the Drude model, lead to anticrossing points in the corresponding dispersion diagram. The different modes in the structure are visualized in Fig. 2.4b using the imaginary part of the Fresnel reflection coefficient r_{p}, as was done for the plasmonic resonances (see Fig. 2.3b).

Considering first only the region of the plot with frequencies larger than the TO phonon frequency, the behavior of the modes looks very comparable to the results on (surface) plasmon polaritons (see Fig. 2.3b). We obtain phonon polaritons in the region from $k_x = 0$ up to the phonon polariton boundary (PhPB, white line in Fig. 2.4b and blue line in Fig. 2.4c) analogous to the plasmon case. Phonon polaritons are damped below the LO phonon frequency.

Using the surface polariton formula, we obtain the analytical dispersion relation of the surface phonon polariton (SPhP) and the Brewster mode (BM) in their respective frequency regime. The surface phonon polariton starts at the TO phonon frequency at the wavevector of the free space dispersion and curves towards higher k_x-vectors for increasing frequencies. The curvature leads to an avoided region comparable to the surface plasmon polariton case starting at $\approx 40\,\mathrm{THz}$ (Fig. 2.4b). The border is given by equation 2.12, which determines the boundaries for surface polariton propagation. It corresponds to the point where the real part of the dielectric function approaches the negative of the dielectric value of air (i.e. $\varepsilon_2 = -\varepsilon_1 = -1$, highlighted by a black sphere in Fig. 2.4a). At this frequency strong damping sets in (see Fig. 2.4c), which reduces for increasing frequencies until it reaches zero at the LO phonon frequency.

Above the LO phonon frequency, the dielectric function of the phonon material becomes positive, which leads to the emergence of the Brewster mode, analogous to the discussion of the Brewster mode above the plasma frequency for the plasmon case (previous section).

Due to the additional resonance at the TO phonon, additional branches appears in the region from zero frequency to the TO phonon frequency. The dielectric functions of both materials are positive in this region, leading to the same modes as in the regime above the LO phonon frequency. However, for the low frequency

regime, the real part of the dielectric function of the material with the Lorentz resonance surpasses the real part of the other material (i.e. air). This leads to a slight modification of the mode structure.

The Brewster mode now appears at a boundary from an optical thinner to a thicker material, which leads to a different refraction than for the high frequency case. Furthermore, it is interesting to see, how the Brewster mode turns into the surface phonon polariton mode at the TO phonon frequency. The reason is that the dielectric function of the Lorentz-type material changes sign, which leads to a reversal of the k_z-vector direction. Hence, the situation is equal to the description using two waves with positive k-vectors pointing in opposite directions, which we used to model the surface polariton dispersion.

Additionally to the Brewster mode, there are also phonon polaritons below the TO phonon frequency. They occupy a region in the (k_x,ν)-dispersion diagram from $k_x = 0$ to the high-k_x-vector boundary (PhPB), which is analytically fully captured by the phonon polariton boundary formula $k_x = k_\mathrm{P}$. A difference is, however, that in the low frequency range, the possible k_x-vector distribution can exceed the light line. Thus, imaginary k_z vectors can occur. This can be easily seen by combining equation 2.17 at the phonon polariton boundary ($k_x = k_\mathrm{P}$) and equation 2.4 and solving for $k_{z,1}$

$$k_{z,1} = \sqrt{\varepsilon_1 - \varepsilon_2}\, k_0. \tag{2.25}$$

As stated above, ε_1 in this frequency range is smaller than ε_2 in the real part and both functions feature a negligible imaginary part, as there are no resonances nearby. Hence, $k_{z,1}$ is in this case purely imaginary. As a consequence, polariton modes with $k_x > k_0$ feature an increase of the electric field away from the surface and will not be considered further.

Nevertheless, the possibility of achieving polaritons – especially the surface polaritons – with k_x-vectors larger than the light line k-vector is in itself intriguing as it is the reason for strong light confinement. The confinement makes these modes interesting for future applications in nano-optics. However, the advantage comes at the price that light cannot simply couple to these modes: There is a pronounced wavevector mismatch, which means that for a given frequency the momentum of the

surface polariton modes lies far beyond the momentum of light (given by the light line). Therefore, one needs to use smart techniques to overcome this discrepancy to launch and ultimately control these surface polaritons.

2.2. Control of surface polaritons

In the above discussion of surface polaritons, we found that the dispersion of strongly confined surface polaritons curves off strongly from the free space light line. As a consequence, these modes cannot be excited by plain far-field illumination, which can only contribute momenta up to the light line. Therefore, one has to find a way to provide the necessary momenta in order to launch these polaritons. There are several ways to achieve this wavevector matching and a good overview of the different approaches is given in reference [Bas16]. The methods range from electron tunneling and grating coupling to wave mixing schemes. Another typical optical approach is to exploit electric near fields. A field that decays exponentially along the z-direction is characterized by a purely imaginary k_z vector component. Inserting such a purely imaginary k_z vector into equation 2.4 leads to

$$k_x^2 = \varepsilon_\mathrm{i} k_0^2 + |k_z|^2, \tag{2.26}$$

which clearly shows that this field distribution offers an in-plane wavevector k_x larger than the free space wavevector k_0 in a material. For a proper choice of materials and a near field which decays strongly (i.e. large $|k_z|$) it is possible to excite surface polaritons. These evanescent waves can be obtained at the boundaries of materials with total internal reflection (see e.g. prism coupling in Otto [Ott68] or Kretschmann [Kre71] configuration). In this approach, surface polariton resonances show up in absorption measurements as strong dips in the reflected spectrum and are commonly used for biological sensing applications [Guo12]. However, this method relies on far-field optics which fundamentally prevents a spatial resolution below the Abbe diffraction limit [Abb73]. The smallest resolvable features are thus given by roughly half the wavelength of the probing radiation. Due to the strong confinement of the surface polaritons, this is not sufficient to map out the individual oscillation periods of the surface wave. Therefore, to gain deeper insights into the

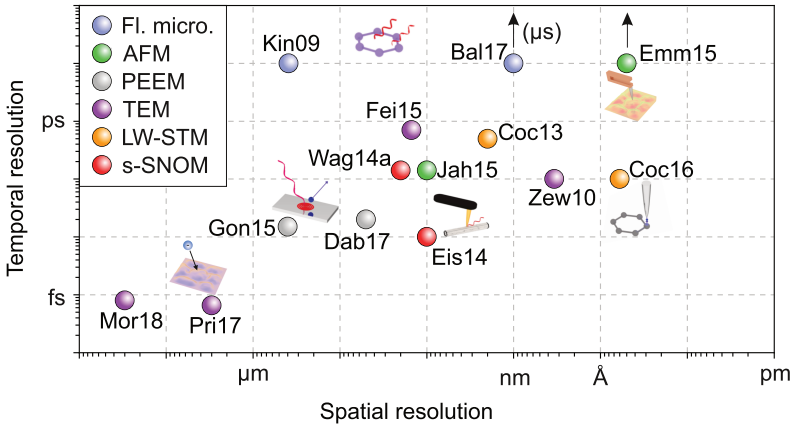

Figure 2.5. | Ultrafast microscopy techniques. Different experimental approaches to observe dynamics in real space are sketched at positions corresponding to their reported resolution in time and space. The methods include, flourescence microscopy (Fl. micro., blue spheres [Kin09, Bal17]), ultrafast atomic force microscopy (AFM, green spheres [Jah15, Emm15]), ultrafast transmission electron microscopy (TEM, purple spheres [Zew10, Fei15, Pri17, Mor18]), ultrafast photo-emission electron microscopy (PEEM, gray spheres [Gon15, Dąb17]), light-wave scanning tunneling microscopy (LW-STM, orange spheres [Coc13, Coc16]) and ultrafast scattering-type scanning near-field optical microscopy (s-SNOM, red spheres [Eis14, Wag14a]).

local, nanoscale behavior of surface polaritons, different techniques are needed. An incomplete summary of available experimental methods to obtain the necessary spatial and temporal resolution is sketched in Fig. 2.5. At the forefront in terms of temporal resolution are currently ultrafast photo-emission electron microscopy (PEEM), ultrafast scattering-type scanning near-field optical microscopy (s-SNOM), ultrafast transmission electron microscopy (TEM) and light-wave scanning tunneling microscopy (LW-STM), where LW-STM can even resolve the vibrations of a single molecule on the femtosecond timescale [Coc16]. To resolve the dielectric changes associated with surface polaritons, PEEM and s-SNOM show great promise. PEEM can directly trace the propagation of surface plasmons [Kah14, Gon15, Dąb17] with a temporal resolution down to a few tens of femtoseconds. The imaging process,

however, poses quite strict limitations on the experimental setup. The full electron optics including the sample under investigation must be kept in vacuum to achieve long enough electron mean free paths for imaging. Additionally, plasmonic research with PEEM has so far mostly focused on metal plasmons.

In this thesis, scattering-type near-field optical microscopy is used to study surface polaritons. The technique combines high spatial resolution in optical and topographic measurements with the perks of a near-field excitation of the sample [Kno99, Hil02, vdV02, Ras03, Kei04, Qaz07]. A sharp metallic tip of an atomic force microscope is used to raster-scan the sample of interest to obtain the height profile of the sample. Apart from the topography, illumination of the tip by probe radiation in the mid-infrared spectral range induces a dipole in the tip, which acts as a local probe to the sample dielectric function beneath the tip (see also appendix A.2). Hence, the intensity of the fields scattered by the tip-sample system strongly depends on the local carrier behavior, e.g. the local carrier density [Sti10, Eis14], optically active resonances [Gov13] or phase transitions [Qaz07, Liu13, Liu14, Hub16].

The lateral resolution of the microscope can be determined by considering a sum of plane waves emitted from the point-like source (the tip dipole). The electric field intensity distribution $I(x)$ can be calculated using the complex-valued k_x-vector distribution $G(k_x)$ that the tip provides. In this estimate of the lateral resolution, we only take the x-component of the k-vector into account. The intensity is given by

$$I(x) = \left| \int_{k_x} G(k_x) \cos(k_x \cdot x) dk_x \right|^2 . \tag{2.27}$$

Using a symmetric flat top distribution $\mathrm{G}(k_x)$ for k_x-vectors smaller than a maximum k_x-vector $k_{x,\max}$ provided by the tip

$$G(k_x) = \begin{cases} 1 & \text{for } |k_x| \leq k_{x,\max} \\ 0 & \text{elsewhere} \end{cases} \tag{2.28}$$

results in

$$I(x) = \left| \frac{\sin(k_{x,\max} \cdot x)}{x} \right|^2 . \tag{2.29}$$

According to the Rayleigh resolution criterion, the minimal resolvable structure has to be larger than the distance of the first zero crossing to the center of the interference pattern. The zero crossing of x and thus minimal resolvable length d_{min} for this case is

$$d_{\mathrm{min}} = \frac{\pi}{k_{x,\mathrm{max}}}. \tag{2.30}$$

This relation links the best resolution in x to the maximum of the k_x-vector in a fashion that is similar to the Heisenberg uncertainty principle. As a sidenote, inserting the maximum obtainable wavevector for light in a material with refractive index n into the equation yields

$$d_{\mathrm{min}} = \frac{\pi}{n \cdot 2\pi/\lambda} = \frac{\lambda}{2n}, \tag{2.31}$$

i.e. the best obtainable resolution in far-field measurements according to Abbe's diffraction limit $d_{\mathrm{Abbe}} = \lambda/(2n\sin(\theta))$ with $\sin(\theta) = 1$, where θ is half of the opening angle of the microscope objective.

This limitation, however, does not hold for SNOM since the field below the tip is an evanescent field, which provides a maximal $k_{x,\mathrm{max}}$ much larger than the free space wavevector (equation 2.26). In the field of s-SNOM, resolutions down to ten nanometers can be achieved even in the mid-infrared spectral region [Eis14, Yox15]. To extract only the near-field information from the scattered signal, the distance between tip and sample is varied sinusoidally, which leads to a modulation of the strongly nonlinear near-field contributions in the scattered field. Using a signal demodulation technique allows one to selectively detect only the near-field components of the scattered radiation (for more information see appendix A.2).

The setup used for the experiments in this thesis has achieved a lateral optical resolution down to ten nanometers at a probe illumination with a wavelength of eight micrometers – an enhancement in resolution of almost three orders of magnitude [Eis14].

The technique is therefore optimally suited to study the local charge density oscillations of surface polaritons far below the diffraction limit. Additionally, the dipole fields of the tip simultaneously provide the necessary k_x-vector to launch surface polaritons in a controlled fashion.

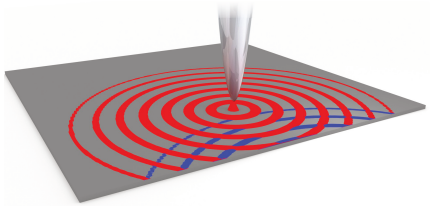

Figure 2.6. | Near-field launching and detection of surface polaritons. The apex of the SNOM tip can launch surface polaritons (red waves) which are reflected at the edges of the structure (blue waves), leading to an interference pattern.

Steady-state near-field microscopy has already been successfully employed to launch and detect surface polaritons in graphene [Fei11, Che12, Fei12], and silicon carbide [Hub08, Hub09] as well as hyperbolic phonon polaritons in hexagonal boron nitride [Dai14, Dai15]. A particularly intriguing feature of the technique in this case is that, at the same time as launching the surface wave, it allows for an exact extraction of the polariton wavelength and thus wavevector. The only prerequisite is a sharply defined feature of the sample where the polaritons can reflect (e.g. the edge of the sample). A sketch of the procedure is detailed in Fig. 2.6: The tip launches a surface polariton, which extends as a circular wave away from the tip (concentric red circles indicate the peaks of the electric field). At the sharp edge of the sample (gray square), these waves are reflected and subsequently propagate back (blue arcs in Fig. 2.6). If the tip is close enough to the edge that the amplitude of the returning wave is significant, the out-going and in-coming waves will noticeably interfere. Depending on the exact distance of the tip to the edge, constructive or destructive interference of the two waves will occur, which depends on the polariton wavelength λ_P. This interference is experimentally measured via the scattered radiation. When the tip is scanned perpendicular to the edge of the sample, an image of a wave pattern with a wavelength of λ_Exp is revealed in the scattered intensity profile. From the experimentally obtained wavelength, which is half as long as the actual polariton wavelength due to the double path geometry, the in-plane wavevector $k_{x,\mathrm{P}}$ of the surface polariton can be determined via

$$\lambda_\mathrm{Exp} = \frac{1}{2} \cdot \lambda_\mathrm{P} = \frac{\pi}{k_{x,\mathrm{P}}}. \tag{2.32}$$

Varying the probe wavelength and recording the experimentally obtained interference pattern thus enables a direct mapping of the polariton dispersion (for a more detailed discussion, see section 3.6 and especially the description of Fig. 3.15).

This approach has been highly successful in determining polariton properties in a variety of different systems [Cal15], most prominently van der Waals materials [Bas16, Low17]. Within these studies, theoretical simulations of the corresponding polariton dispersion have been a critical complementary element. Additionally, the decay length of the experimentally measured pattern allows for an extraction of the polariton damping.

As a next step in polariton research with near-field microscopy, means of active control of surface waves and their properties are actively being investigated. Within this context, three schemes have recently appeared.

One version of tailoring the properties of the surface modes is to couple them to different dielectrics or other polaritons [Cal16] to modify the dielectric surrounding of the polariton or to form completely new hybrid modes out of two excitations that can be detected in steady-state near-field imaging.

Another possible way to tune the dispersion of a polariton mode is to change the intrinsic material properties of its host. For surface plasmon polaritons an easy knob to turn is the carrier density, which shifts the plasma frequency and thus the polariton dispersion (see section 2.1.2). Most work in this regard has been done using surface plasmon polaritons on graphene, as the semimetal-character of graphene allows for a continuous tuning of the carrier density by electrostatic gating (Fig. 2.7a and, e.g., references [Fei12, Che12]). This approach has allowed researchers to tune the polariton wavelength with the applied gate voltage. The timescale over which the wavelength can be tuned by this technique, however, is limited by the speed of the electronic control. For future plasmonic devices that surpass the limitations of today's electronics, one would wish for a faster method of control.

One way to achieve high speed polariton modulation is to use ultrafast laser pulses for optical control. It has been shown that the Drude weight of the carriers in graphene can be modified on ultrashort timescales using a near-infrared pump laser [Wag14a]. Only recently, this idea has been exploited in an experiment by G. X. Ni

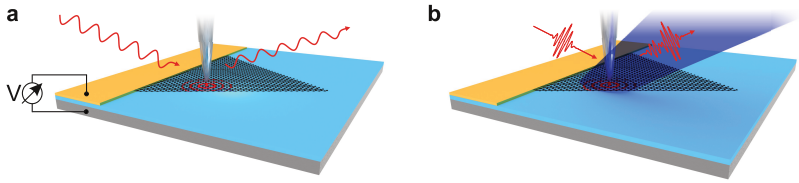

Figure 2.7. | Polariton control schemes for near-field microscopy. a) Slow control of the carrier density in a graphene flake is possible by gating the device with a gold contact on top and the substrate as back-gate. The tip is illuminated with monochromatic probe radiation (red arrow in) and launches a plasmon. The scattered radiation (red arrow out) contains information about the near-field interaction of tip and sample. **b)** Ultrafast control can be achieved using pump-probe detection. A pump pulse (blue shaded cone indicates the pump beam) impinges on the flake and a probe pulse (red waveform incoming) launches a polariton. The photo-induced changes to the polariton can be extracted from the change in the scattered probe pulse off the tip (red pulse outgoing) as a function of delay time between the pump and probe pulses.

and colleagues [Ni16] to show that in a specifically conditioned graphene flake (which shows no surface plasmons in equilibrium) surface plasmon polaritons can be induced and detected after optical excitation (a schematic is shown in Fig. 2.7b). This proof-of-principle result shows the way towards future ultrafast plasmonic devices.

Nevertheless, due to the persistence of carriers in the semi-metal graphene, high-contrast polariton switching should be more easily achieved in a material with a bandgap and very few free carriers in equilibrium. Such a material would have no mid-infrared surface plasmon polariton modes in equilibrium, but such modes could be switched on by interband excitations on ultrafast timescales, where a femtosecond optical pump pulse generates the free carrier density needed to support them.

In the scope of this work, the first real space images of an actively switched polariton based on a semiconductor will be shown for different times after photo-activation. For this purpose an ultrafast near-field microscope is essential to visualize the ultrafast dynamics with nanoscale resolution. Fortunately, the setup in Regensburg (for technical details see appendix A and [Eis14, Eis15]) is perfectly suited for this task: The probe pulses are centered in the mid-infrared and can be tuned between 15 and

60 THz depending on the requirements of the sample. This frequency range contains interesting low-energy elementary excitations like plasmons or phonons, which can form surface polaritons. Moreover, the frequency is sufficiently low to also match the region in which the plasma frequency of semiconductors can be tuned by photo-excitation. The pulse duration of the probe pulses is 60 fs full width at half maximum (FWHM), slightly dependent on the exact center frequency. Additionally, the setup provides ultrashort near-infrared pump pulses with a center wavelength of 1550 nm (40 fs FWHM) to photo-excite the investigated sample. These pulses can also be frequency doubled to 780 nm to excite samples with larger bandgaps. This temporal resolution in intensity-resolved mid-infrared near-field measurements is currently world-leading and is ideally suited to measure the short-lived excitations of photo-activated polaritons. Furthermore, the system is outstanding in the current near-field microscopy landscape, as it is the only setup that also can resolve the electric field of the scattered mid-infrared probe radiation by electro-optic sampling, yielding insights in the real-time evolution of physical processes.

With these tools at hand, it is possible to expand on the previously mentioned results and introduce a new material for surface polariton control, namely black phosphorus.

2.3. Black phosphorus as a plasmonic switch

Black phosphorus is a layered van der Waals bonded material with very favorable properties for the endeavor of this work: demonstrating a switchable polaritonic device similar to a transistor in electronics. The different layers in top view resemble the honeycomb lattice of graphene. However, it has a puckered structure in the in-plane axis, where two rows are vertically offset from the neighboring two rows (see Fig. 2.8a). Independent of the number of layers, black phosphorus is a direct bandgap semiconductor. In its bulk form it features a bandgap of 0.3 eV (Fig. 2.8b). As a consequence, the carrier density in the unexcited material is relatively low. Hence, the plasma frequency of free carriers is small compared to the frequency range of the mid-infrared probe pulses. Owing to the small bandgap it is, however, possible to inject free carriers into the material by an ultrafast near-infrared pump pulse.

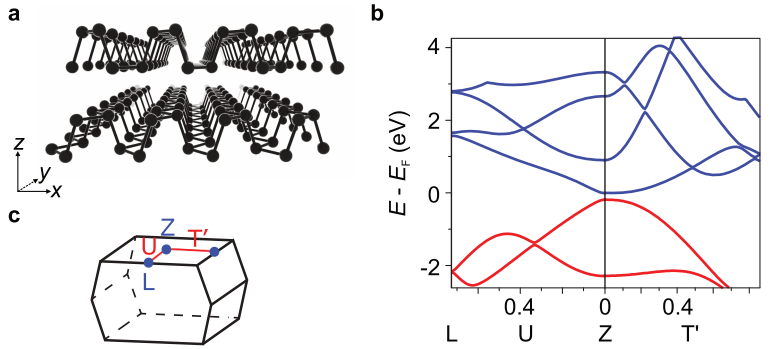

Figure 2.8. | Black phosphorus crystal properties. **a)** Crystal structure of black phosphorus. **b)** Band structure of bulk black phosphorus along the red lines in **c**, adapted from reference [Li14]. **c)** Reciprocal lattice of black phosphorus including the high symmetry points Z and L and the crystal directions T' and U.

These free carriers will be created near the Z point of the Brillouin zone (plotted in Fig. 2.8c) and form a plasma. One can therefore assign a plasma frequency to the system, and this plasma frequency can easily enter the mid-infrared spectral range thanks to the small in-plane effective masses in the material (electron masses: $m_{\mathrm{e},x} = 0.096 \cdot m_0$, $m_{\mathrm{e},y} = 1.14 \cdot m_0$ and hole masses: $m_{\mathrm{h},x} = 0.091 \cdot m_0$, $m_{\mathrm{h},y} = 0.625 \cdot m_0$, where m_0 is the bare electron mass [Mad04] and the axes are chosen according to Fig. 2.8a). According to section 2.1.2, this plasmon can hybridize with the mid-infrared radiation of the probe pulses and a surface plasmon polariton can be launched below the tip of the near-field microscope. These properties make black phosphorus a promising candidate for the ultrafast switching and control of surface polaritons.

Furthermore, the material features more very interesting properties, which come in handy for polaritonic studies and applications. The most obvious point of interest is the strong in-plane anisotropy of the material [Qia14, Mad04]. A closer look at the band structure diagram in Fig. 2.8b reveals that the two in-plane axes of the material differ by almost one order of magnitude in their effective masses. The resulting inequality of the dielectric functions in the two directions can lead to

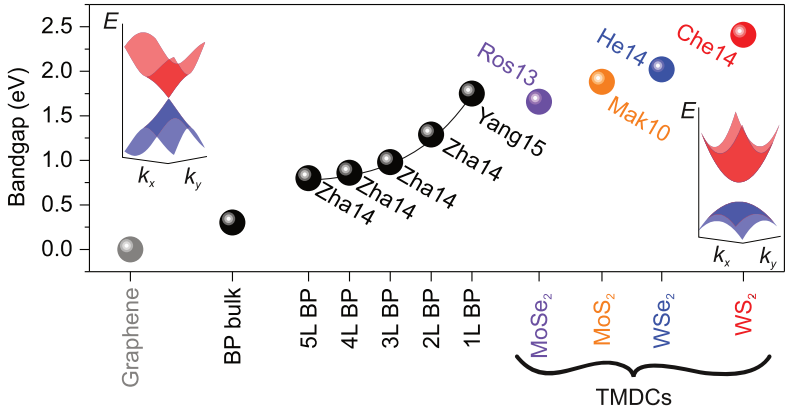

Figure 2.9. | Bandgaps of different two-dimensional materials. The bandgaps of graphene, various thicknesses of black phosphorus (one to five layers and bulk), and selected monolayer transition metal dichalcogenides (TMDCs) is depicted. Next to each data point is the corresponding literature source from which the value was taken. For black phosphorus the values are from [Zha14, Yan15]. For the transition metal dichalcogenides the references are [Che14, He14, Mak10, Ros13]. Insets: Schematic band structures of gapless graphene (left) and a direct bandgap semiconductor (right).

new physics, with one exciting prospect being the directional mode splitting of surface polaritons. Moreover, being a van der Waals layered material puts black phosphorus in the category of materials which can be exfoliated using the famous scotch-tape technique initially invented for graphene [Nov05, CG14b]. This class of two-dimensional materials is currently the focus of intense scientific investigation, as these systems allow one to construct single atomic layers of the compounds that are stable and inert. The lack of dangling bonds is a great advantage for the fabrication of van der Waals heterostructures out of different materials on the atomic level [Gei13]. One can therefore use black phosphorus as a plasmonic material inside a larger structure where the surroundings will strongly influence the polariton modes and lead to new physics, as is the case in this thesis. Additionally, it has been shown that the bandgap of black phosphorus depends on the number of layers in the

crystal. From the bulk bandgap of 0.3 eV the bandgap increases for fewer and fewer layers, reaching almost 2 eV for the monolayer [CG14b, Zha14, Yan15]. The scaling behavior is shown in Fig. 2.9 alongside other typical two-dimensional materials and their bandgaps. Plotted are the experimental values from the literature. Depending on the exact experimental technique, these correspond in some cases to the electronic bandgap and in others to the optical bandgap. Nevertheless, one can easily see that the tuning range of black phosphorus exactly covers the open area between the zero-bandgap material graphene and the large bandgap semiconductors of the transition metal dichalcogenides [CG15, Lin15]. Therefore, bandgap engineering by tailoring the number of layers turns black phosphorus into a very versatile platform for surface polariton studies. Recently, the excitons of black phosphorus have also attracted interest [Wan15b, Sur16] and make it a potential system for exciton-polaritons.

There is, however, one significant drawback to the material: Even though black phosphorus is one of the stable allotropes of phosphorus, it is highly reactive to humidity. Exposed to ambient conditions, it will degrade rapidly [Gam16]. The degradation makes it a tough material to work with in near-field microscopy, which is typically performed under ambient conditions. However, the approach of heterostructuring can be highly beneficial to avoiding this effect. Covering the material with a protecting layer can reduce the degradation significantly [Woo14, Dog15] and in this work it was found that the heterostructures introduced in the next chapter were stable over multiple months without any effects of degradation.

Chapter 3

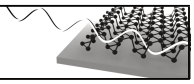

Ultrafast switching and real-space observation of interface polaritons in black phosphorus/silicon dioxide heterostructures

3.1. Custom-tailored heterostructures of black phosphorus and silicon dioxide

For the direct measurement of interface polaritons, custom tailored heterostructures based on thin black phosphorus flakes are used. The samples were fabricated in the group of M. S. Vitiello in Pisa by collaborators experienced in the design and manufacturing of black phosphorus nanostructures and devices [Vit15, Vit16]. A schematic representation of the typical composition of the heterostructures is shown in Fig. 3.1a and an artistic depiction of one particular heterostructure investigated with ultrafast near-field microscopy is shown in Fig. 3.1b. The substrate is a 0.38 mm-thick silicon wafer, which is capped by a 300-nm-thick silicon dioxide (SiO_2) buffer layer. Individual flakes of black phosphorus with different thicknesses ranging from 50 to 200 nm are deposited on the substrate using mechanical exfo-

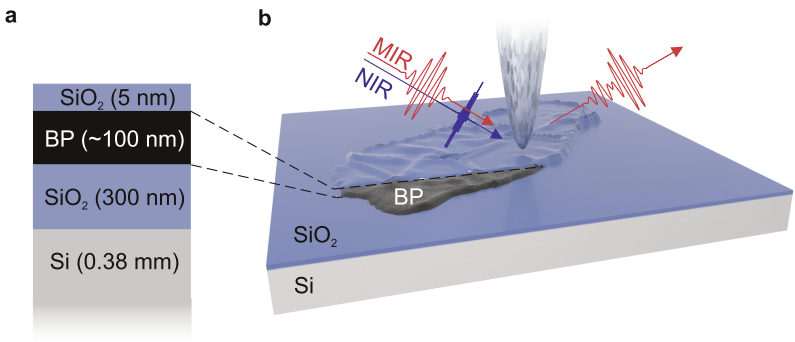

Figure 3.1. | Schematic of the sample and measurement technique. **a)** Sketch of the layered structure consisting of 5 nm silicon dioxide (SiO_2), black phosphorus (BP) flakes of heights on the order of 100 nm on a SiO_2 covered silicon (Si) wafer. **b)** Schematic of the experimental approach. The flakes are investigated using a near-field microscope with probe pulses in the mid-infrared (MIR) which are scattered off an atomic force microscopy tip. The sample is excited with near-infrared (NIR) pump pulses.

liation. For such flake heights, the physical properties of black phosphorus can be assumed to be identical to its bulk form. Therefore, the flakes have a bandgap of roughly 0.3 eV, such that the near-infrared pump pulse centered at a wavelength of 1560 nm (photon energy: 0.8 eV, blue waveform in Fig. 3.1b) can drive interband excitations, inducing a free carrier density in the structure and switching it to a state that supports surface plasmon polaritons. The mid-infrared probe pulses (red waveform) can then excite a polariton. The mid-infrared dipole oscillation of the coupled tip-sample system depends not only on the material properties underneath the tip, but also on interference between direct excitation and polaritons that have been launched by the tip, propagated to the edge of the structure, reflected, and then propagated back to the tip. The total dipolar response is scattered into the far field (red outgoing wave) where the local near-field contribution can be decoupled from background scattering using demodulation techniques (see appendix A.2). To prevent degradation of the samples, an additional cover layer of 5 nm silicon diox-

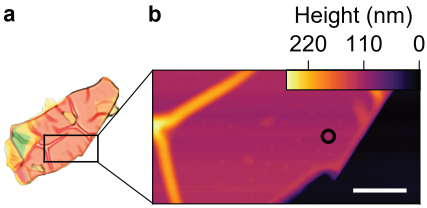

Figure 3.2. | Exemplary SiO_2/BP/SiO_2 heterostructure. **a)** Optical microscopy image of the heterostructure. **b)** AFM image of the area marked in **a** showing the homogeneous height of the flake and the sharp edges. The circle is a marker to indicate where experiments later on in this thesis are performed. Scale bar: 2 µm.

ide has been sputtered onto the sample using an argon plasma with a pressure of $2.5 \cdot 10^{-3}$ mbar and a radio frequency power of 70 W. The thickness of 5 nm has proven to be ideal for our measurements, as on one hand it is thick enough to prevent degradation for several months and on the other hand is thin enough, such that our near-field probe can still resolve features from the black phosphorus layer. Furthermore, silicon dioxide itself is an interesting material as it contains a phonon band in the spectral range of the experiment, where surface phonon polaritons can form. The interaction of these modes with the transient surface plasmon modes in the black phosphorus layer is a key subject of this work and leads to intriguing new features in the dispersion of the combined polariton.

A typical flake is presented in Fig. 3.2. An image of the flake under an optical microscope is shown in Fig. 3.2a. The structure is not black as one might assume from the name of black phosphorus but rather rose/pink-colored with some yellow/green exceptions at the lower left side. These colors are the result of thin-film interference of light in the visible spectrum inside the multilayer structure. Depending on the exact thickness of the flake, different colors are observed. The pink color is thereby characteristic for a height on the order of 100 nm. Investigation of the sample in our near-field microscope allows for a more exact determination of the structure's height profile. The built-in atomic force microscopy capabilities of the microscope directly show the topography of the flake at selected locations. In Fig. 3.2b, a topographic map is shown of the region bounded by the black box in the optical image (Fig. 3.2a) with the height color-coded as a function of tip position. The continuous magenta color across the majority of the flake indicates that the flake has a very homogeneous height of 110 nm across the investigated area. Only at the left and top edge, there

are two folds of increased height. These folds have been seen on many flakes and are most likely due to encapsulation of molecules occurring either during exfoliation (and therefore below the black phosphorus layer) or during sputtering (and, hence, between the black phosphorus flakes and the silicon dioxide cover layer). Support for this hypothesis is provided by the observation that heating the flake with high intensities of the pump laser leads to an increase of these folds, which likely occurs due to the thermal expansion of the encapsulated material. Subsequent cooling can reverse the process to a certain extent. However, excessively high pump intensities lead to permanent damage of the flakes. The flakes then also degrade over time. This is possibly due to ruptured cover layers, as such an effect would expose the black phosphorus to ambient conditions. Therefore, all experiments in this thesis are carried out with a reduced repetition rate of the pump laser (10 MHz) and a pump fluence of $1\,\mathrm{mJ{\cdot}cm^{-2}}$, unless specifically stated otherwise. At these intensities, the heterostructures either exhibited no observable changes, or the changes were limited to slight, mostly reversible modifications to the topography. This has proven to be an acceptable trade-off between the durability of the heterostructures and the injected carrier density, which is necessary to form a plasma response in the frequency spectrum of the probe pulses.

An important feature of the flake depicted in Fig. 3.2 is, that it contains two sharp edges at its right hand side with different angles with respect to the horizontal axis of the graphic. As discussed in section 2.2, these edges are prime candidates for the study of surface polaritons, as they can lead to a strong reflection of the surface waves, giving rise to an interference pattern from which the dispersion of the modes can be extracted. As a next step, we want to investigate the change of this particular structure upon photo-activation because the injection of free carriers is the first necessary step towards a switchable polariton mode.

3.2. Photo-activation of a polaritonic mode in the structure

The most important question for photo-switching of polaritons in the heterostructure is whether the pump pulses can induce a sufficiently high carrier density in the black phosphorus layer. Only then can the mid-infrared radiation of the probe pulse hybridize with the resulting plasmon to form a polariton. In previous work, a good indicator of the plasma frequency and therefore carrier concentration has been the strength of the scattered near-field intensity [Sti10, Eis14]. A characteristic nonlinear evolution of the scattered intensity as a function of carrier concentration has previously been observed [Sti10]. Specifically for high carrier densities, where the plasma frequency resides within or above the probe spectrum, a high scattered intensity is observed. Generally, in a pump-probe experiment, where the carrier density is modified transiently, one moves along this nonlinear curve as a function of time. The curve typically has a slight decrease followed by a rapid increase of the scattered signal at the point where the plasma frequency surpasses the center frequency of the probe spectrum [Hub14, Eis15].

To study if carriers can successfully be injected into the black phosphorus layer, a pump-probe measurement is performed on the flake shown in the previous section. To this end, the tip is placed at the position of the black circle in Fig. 3.2 and the scattered near-field intensity is recorded while varying the pump-probe delay time t_{pp}, which results in a temporal shift of the pump pulses with respect to the probe pulses[1]. The results for the fourth demodulation order I_4 are plotted in Fig. 3.3. The subscript four indicates that the signal is measured that oscillates with the fourth harmonic frequency of the tip tapping frequency. Using these high demodulation orders (I_3, I_4, ...) is a way to suppress unwanted background radiation, as empirically only the nonlinear near-field interaction of the tip-sample system as a function of tip-sample distance produces such high harmonic signals (for more details see appendix A.2). Normalizing the signal to a value at negative delay times

[1] The timing zero-point for all experiments in this work is defined by half the rise in the pump-probe response of an indium arsenide reference sample. It features a sharp onset [Eis14], which allows to correlate the relative timing of all measurements.

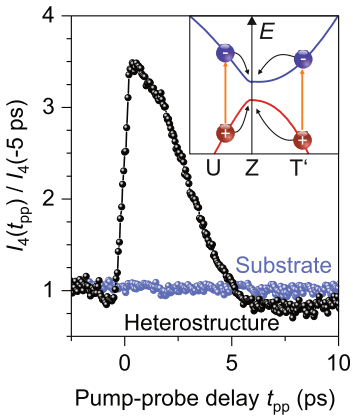

Figure 3.3. | Pump-induced change to the scattered near-field intensity on the substrate and the heterostructure. The scattered mid-infrared near-field intensity I_4 is plotted as a function of pump-probe delay time on the substrate (blue points and line) and for the spot on the heterostructure marked in Fig. 3.2 (black points and line). The signal is normalized to the values at negative delay times ($t_{pp} = -5$ ps). Inset: Band structure of bulk black phosphorus from Fig. 2.8b. Orange arrows show where the pump pulses can create electron hole pairs (blue and red spheres), which subsequently move towards the band extrema due to carrier cooling (black arrows).

allows us to quantify the photo-induced change. At a reference position on the substrate, no change is measured (blue points). However, on the heterostructure (black points) a strong modification by a factor of ≈ 3.5 appears following the pump excitation. The onset of the signal has a rise time of 380 fs (from 20% to 80% of its maximum) followed by a slower decay that decreases to unity after 5 ps. Subsequently, the intensity drops below the baseline and takes roughly 20 ps to fully recover to the initial value (not shown). On a microscopic level, the pump pulses induce electron-hole pairs in the black phosphorus (see blue and red spheres in the inset of Fig. 3.3). Due to the small bandgap in bulk black phosphorus (0.3 eV) and the comparably high pump photon energy (0.8 eV), the carriers are injected in states far above the bandgap (orange arrows in the inset of Fig. 3.3) that feature relatively large effective masses. The subsequent intraband relaxation towards the low-effective-mass states at the bandgap (black arrows in the inset of Fig. 3.3) leads to a decrease in the effective masses of the carriers and hence the conductivity of the electron-hole plasma increases over time. As a result, the scattering signal shows a delayed increase following the arrival of the pump pulse, which is the reason for the 380-fs-long rise time of the pump-probe signal. Subsequently, the electron-hole pairs at the Z point (see inset in Fig. 3.3 as well as Fig. 2.8b and c) recombine and cause a monotonic decrease of the measured scattered near-field intensity until $t_{pp} \approx 5$ ps.

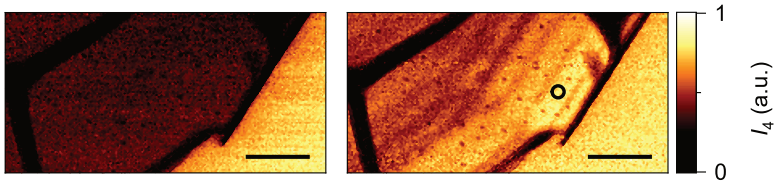

Figure 3.4. | Excitation of localized polaritons on a photo-excited black phosphorus heterostructure. Color-coded is the scattered near-field intensity I_4 as a function of position in the region shown in Fig 3.2 for the unexcited sample (left panel) and 250 fs after excitation with a near-infrared pump pulse (right panel). A circle marks the position of the pump-probe measurement in Fig. 3.3. Scale bars: 2 µm.

The experimentally observed decrease of the intensity below the baseline for delay times $5\,\mathrm{ps} < t_{\mathrm{pp}} \leq 20\,\mathrm{ps}$ is due to the suppression of surface phonons in the silicon dioxide buffer layer, which are screened by the remaining dilute electron-hole plasma (see section 3.5.3 and especially Fig. 3.13 and its description). The observed 3.5-fold maximum modification to the scattered intensity relative to the equilibrium value is unexpectedly strong. In previous near-field measurements, typical changes of a few percent up to unity were observed on semiconducting materials [Eis15, Hub16]. Nonetheless, this strong tunability of the material response is good news for active control.

As a next step, the spatial distribution of the scattered intensity across the flake is investigated for the unexcited and the excited structure (Fig. 3.4). Plotted is the scattered near-field intensity I_4 as a function of tip position across the region, where the topography scan in Fig. 3.2 was taken. In the left panel of Fig. 3.4, I_4 is measured without pump excitation. There is a clear contrast between the substrate, which displays a high value, equal to a high scattering signal, and the heterostructure, which is dark and mostly homogeneous in the central region. Only the folds in the structure and the edges show a lower signal. This low scattered intensity is expected as the equilibrium carrier density is low in the black phosphorus, whereas the silicon dioxide features a strong phonon resonance in the frequency bandwidth of the probe pulse, which manifests itself in a high scattering response (compare to e.g. [Fei11]).

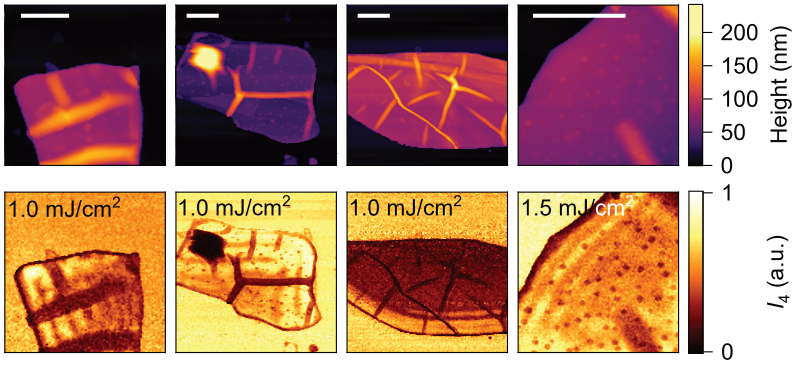

Figure 3.5. | Selection of flakes with interference patterns. The top row shows the measured topography of four different heterostructures. Below, the scattered near-field intensity I_4 for each flake is depicted at a positive pump-probe delay time (where the maximum pump-induced change is recorded). The pump fluence is written in the top left corner of the near-field images. Each scalebar is 3 µm long.

Mapping the scattered intensity again, but this time 250 fs after the sample has been photo-excited by the pump pulses (corresponding roughly to the maximum of the pump-induced change in Fig. 3.3) shows a clearly different response of the heterostructure (right panel in Fig. 3.4). The scattered intensity of the substrate is unchanged in accordance with the absence of any pump-induced change in Fig. 3.3. However, the intensity of the heterostructure has increased drastically to a value equal to what is observed over the silicon dioxide substrate. Moreover, the intensity across the flake is not uniform. There is a clear trend from a high scattering response to a low response the further the tip moves away from the edges. Superimposed on this trend is a periodic modulation of the signal, where the maxima align parallel to the closest edge. This behavior is reminiscent of surface plasmon polaritons in graphene and shows that there is an interference pattern of a polariton in the structure, which can be activated by photo-excitation.

In further measurements on different flakes it is verified that the switching behavior is not a unique property of the one flake that is shown here as a representative. In

fact, on practically all flakes that have sufficiently well-defined long edges and are not degraded, such fringe patterns are found. A selection of flakes is collected in Fig. 3.5. In the top row, the measured height profile of each flake is depicted, color-coded as function of tip position. Below each topography image, the simultaneously recorded near-field signal of the flake for a pump-probe delay of maximum signal change is portrayed. Depending on the heterostructure, sometimes a slightly modified pump fluence has to be used to obtain similarly strong effects as on the exemplary structure in Fig. 3.4. As one can see, the pattern always follows the edges of the topography and sometimes has a preference for one edge over another. In some cases the fringe pattern prevails even through the folds which have been mentioned before. This might be an indication that the contamination of the fold is located above the black phosphorus flake and the polariton can pass below it.

Having found these very prominent features reminiscent of polaritons, the question arises of how fast the structures can actually be photo-activated and how long the polariton response lasts following excitation before it is no longer supported by the system due to carrier relaxation. The pump-probe experiment in Fig. 3.3 gives a rough estimate of the relevant timescales because it indicates the black phosphorus carrier lifetimes but in the next section the emergence and decay of the polariton will be measured in real space to see the evolution of the mode in time.

3.3. Determination of switching speeds

In the previous section we have seen that the polariton mode is already activated at the peak of the pump-probe trace, demonstrating very prominent interference fringes in the scattered intensity. To determine the full evolution of the mode upon photo-activation, more snapshot images have to be recorded for varying delay between the probe and the pump pulses. From these images, a movie of the excitation can be constructed.

An eight-frame film-strip of the heterostructure of Fig. 3.4 is shown in Fig. 3.6. The scan area has been decreased to include only the fringe pattern of the top right edge of the previous scan and the orientation has been rotated in such a way that the edge

of the flake lies parallel to the vertical axis of the images. The delay times range from -5 ps to 10 ps. The negative time value signifies that the pump pulse arrived later than the probe pulse, which means that the probe experiences an unexcited sample. Accordingly, the scattered intensity I_4, which is again plotted as function of tip position, is uniform and low. Right at the temporal overlap of the pump and probe pulses ($t_{\mathrm{pp}} = 0$ ps) a well defined standing wave pattern is seen with four prominent bright fringes, spanning the flake from the edge to approximately half of the visible scan window. The number of fringes increases at the peak of the pump-probe trace at $t_{\mathrm{pp}} = 250$ fs (compare to Fig. 3.3). Additionally, an increase in intensity and a smearing of the pattern appears, reducing the visibility of the pattern closer to the edge. From this maximum onwards, a decay of the modulation sets in, analogous to the signal decrease in the pump-probe measurement. This behavior continues for the times of 1.5 ps, 2.25 ps and 3 ps until, at $t_{\mathrm{pp}} = 4$ ps, only the two first intensity maxima can be seen as a faint increase in the scattered intensity. Interestingly, the periodicity of the standing wave pattern is fixed for all delay times from 0 ps to 4 ps. That means the polariton wavelength does not significantly change during the whole switching process - a very intriguing property that will be discussed in more detail in section 3.5.3. At later times, e.g. 10 ps after excitation, the structure becomes homogeneously dark again, with an absolute value even smaller than the value at negative times. This is in good agreement with the pump-probe response in Fig. 3.3, as there the intensity also drops below the equilibrium value and only recovers after 20 ps.

Strikingly, the standing wave pattern caused by the polariton is already present at zero pump-probe delay time, meaning further experiments at smaller time intervals are required to retrieve the switch-on time of the mode. Therefore, an investigation of the interference pattern is performed in the temporal region between $t_{\mathrm{pp}} = -50$ fs and 190 fs. Here, single line scans are taken of the scattered near-field intensity perpendicular to the edge, rather than full images. The scan direction is from the substrate onto the flake. The curves are offset vertically for a better visibility and shown in Fig. 3.7a. At $t_{\mathrm{pp}} = -50$ fs the intensity profile is flat meaning that there is no polaritonic effect yet. Moving closer towards the pump-probe time overlap $t_{\mathrm{pp}} = 0$ fs, a slight modification becomes discernible and is truly visible at $t_{\mathrm{pp}} = -15$ fs.

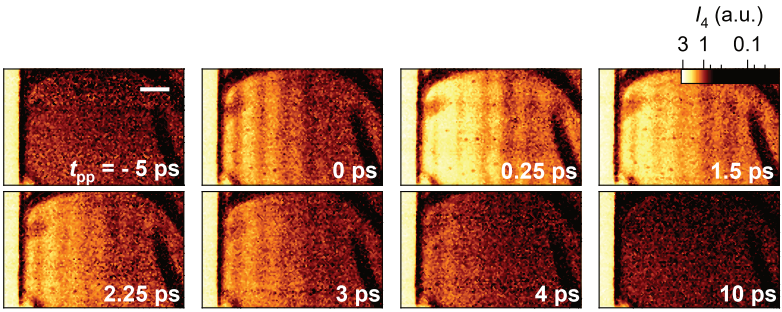

Figure 3.6. | Temporal evolution of the polariton fringe pattern. Plotted is the spatially resolved scattered near-field intensity I_4 as a function of pump-probe delay time including one edge of the heterostructure shown in Fig. 3.4. Scale bar: 1 µm.

This is not unreasonable as the pulses of the experiment have a finite temporal extension (60 fs FWHM for the probe pulses and 40 fs FHWM for the pump pulses) allowing for a non-zero overlap integral between the two already before delay time zero. From this point onwards the fringe amplitude increases drastically towards 70 fs and then increases more slowly until $t_{\mathrm{pp}} = 190\,\mathrm{fs}$. To get a more quantitative measure of the rate of increase of the fringe amplitude, the discernible modulations were fitted with sine waves. For each maximum at a single delay time, the fitting was performed leading to a selection of slightly different fringe amplitudes. The mean of these amplitudes as a function of delay time is plotted in Fig. 3.7b. The error bars signify the maximum and minimum deviation of the amplitudes extracted from the fitting routine. Furthermore, the root mean square (RMS) amplitude of the noise in the measurement is marked with a red bar below which the results are not easily distinguishable from noise. Nevertheless, already at $t_{\mathrm{pp}} = -15\,\mathrm{fs}$, the mean fringe amplitude surpasses the noise significantly. For later delay times it rises monotonically and tends to saturate for the latest delay time, at $t_{\mathrm{pp}} = 190\,\mathrm{fs}$. Normalizing the sine wave amplitudes to the value at $t_{\mathrm{pp}} = 190\,\mathrm{fs}$, we see that half of the rise is already completed within only 50 fs. On roughly the same timescale the fringe amplitude also rises from zero to the first detectable signal above the noise floor. This proves that the mode can be activated on ultrafast timescales, in this

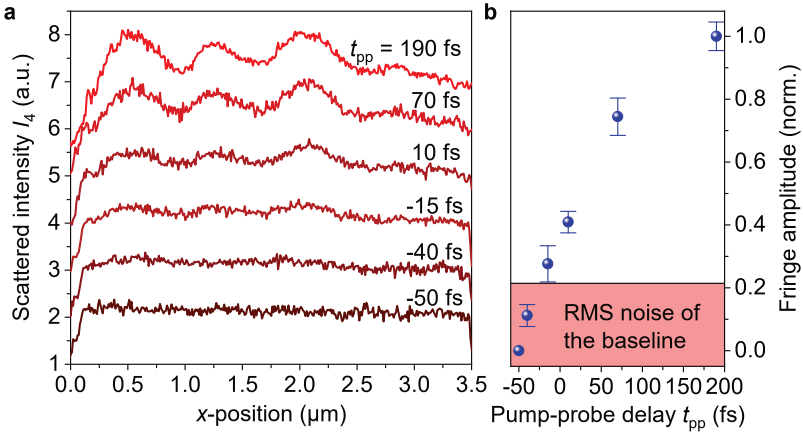

Figure 3.7. | Evolution of the fringe pattern on ultrafast timescales. **a)** Spatial modulation of the scattered near-field intensity I_4 for a linecut perpendicular to the edge of the heterostructure as a function of pump-probe delay time. **b)** From the data in **a** one can extract the amplitude of each individual oscillation and compare them to the noise on the baseline. The error bars signify the largest error of the amplitude for each delay time as determined by the fitting routine.

case even faster than our probe pulse duration. To check whether such a timescale is reasonable for a polariton, the findings of R. Huber *et al.* on the build-up of screening in gallium arsenide [Hub01] and the formation of a coupled phonon-plasmon mode in indium phosphide should be considered [Hub05]. In both cases, the switching time scales with the inverse of the dominant mode frequency. For the electron-hole plasma, this is the plasma frequency. For the coupled phonon-plasmon mode, the frequency ν_{P+} of the higher polariton branch of the coupled system determined the timescales. In the latter case, R. Huber *et al.* have been able to fit their data using a buildup time $\tau \approx 1.6/\nu_{P+}$. For the mode observed in this thesis the frequency is around 33 THz (see e.g. Fig. 3.16 in section 3.6) leading to a buildup time of ≈ 48 fs. This theoretical value based on measurements for a coupled phonon-plasmon mode is in good agreement with the experimental findings and might be a first hint that the phonons in our system play an essential role in the mode structure of the polariton.

Coming back to the overall temporal evolution of the standing wave pattern (i.e. Fig. 3.6), we actually find further evidence that the polariton is not a bare surface plasmon polariton as has been suggested earlier. Firstly, the mode shows a propagation length of $\approx 6\,\mu m$ (considering propagation including reflection at the edge). Such long propagation distances have not yet been reported for surface plasmon polaritons in the mid-infrared regime at room temperature. For high quality graphene samples encapsulated in hexagonal boron nitride, the longest surface plasmon propagation has been on the order of $1.6\,\mu m$ [Woe15]. As a sidenote, very recently, an intrinsic plasmonic propagation length exceeding $10\,\mu m$ has been reported for encapsulated graphene at liquid-nitrogen temperatures [Ni18]. However, since the measurements in this thesis are all carried out at room temperature, also the literature values for room temperature should be used for a direct comparison.

The second proof of a more complex polariton composition is the observed fixed wavevector distribution for all pump-probe delay times. In contrast to most other experiments resolving polaritons in real space with near-field microscopy, we use broadband pulses as our probe rather than a monochromatic wave in order to achieve ultrafast temporal resolution. Using a broadband probe means that the measured intensity is actually a superposition of multiple frequencies and therefore – depending on the polariton dispersion – different wavevectors.

From section 2.1.2 and especially Fig. 2.3b we know that the dispersion of a surface plasmon polariton curves off strongly from the light line, leading to a broad distribution of different k_x-vectors for a selected frequency range. Hence, for a bare surface plasmon polariton, a broadband mid-infrared probe pulse would be expected to excite surface waves with a broad distribution of k_x-vectors, which would correspond to standing wave patterns with different periodicities. The experimentally observed pattern would be the superposition of all of these and would not result in a standing wave pattern in the scattered intensity image with a single fringe periodicity. Taking these considerations into account, it is very intriguing why such a standing wave pattern is even observed with a broadband probe pulse in the first place.

The observed slight smearing of the fringe pattern in Fig. 3.6 can be understood in this picture as the result of a weakly frequency dependent dispersion, which leads to a narrow but not infinitesimal k_x-vector bandwidth contributing to the overall

interference pattern. From the observation that the fringes only broaden at the maximum of the pump-probe scan, diffusion of carriers can be ruled out as the leading cause of the smearing, since that would lead to a continued broadening with increasing pump-probe delay, which is not observed.

Another indication that the mode is not a bare surface plasmon polariton is that the plasmon polariton dispersion is crucially dependent on the plasma frequency and therefore carrier density in the system. The pump-probe measurement clearly showed an increase and decrease of the scattered intensity, which originates from an increase and decrease of the carrier concentration, i.e. the evolution of the plasma frequency over time [Eis14]. This should result in a change to the dispersion of the surface plasmon polariton, which – even in a monochromatic experiment – would yield a change in the periodicity of the standing wave pattern (compare e.g. [Fei12, Che12] for experiments using electrostatic gating). Nevertheless, in Fig. 3.6 and Fig. 3.7a the wavelength is fixed to one center wavelength and only the amplitude of the excitation evolves with time – very atypical for a pure surface plasmon polariton.

To unravel the observed complexity, one has to spectrally resolve the changes to the scattered probe radiation. The intensity resolved measurements that have been shown so far, are not capable of differentiating between the evolutions of each spectral component of the probe pulses. They rather give an averaged response of the heterostructure. In the next section, for a more diversified picture and to resolve the dominant frequency components of the polariton activation, the spectral response of the system will be disentangled using ultrafast Fourier transform infrared spectroscopy on the nanoscale.

3.4. Time-resolved spectral analysis of the hybrid mode

The polariton movie in the previous section revealed that the surface mode in the heterostructure mostly contains a single in-plane momentum corresponding to a single wavelength, which stays fixed across all delay times. To obtain an insight into the full dispersion of the polariton the evolution of the energy of the mode

also needs to be determined. To this end, the spectral response of the substrate and the spectral response of the heterostructure with and without photo-excitation are measured in this section using ultrafast Fourier-transform infrared spectroscopy (FTIR) on the nanoscale. The method is detailed in appendix A.4 and allows us to spectrally resolve the scattered near fields of the probe pulses in amplitude and phase (relative to the probe pulses without sample and near-field interaction).

In near-field measurements, the spectrum interacting with the sample is not simply the spectrum of the probe pulse. The tip-sample system can scatter different frequencies with different efficiencies, for example due to dipole resonances in the tip. Consequently, the scattered near-field spectrum might deviate from the spectrum of the probe pulses that are focused on the tip [Eis15]. To account for such effects, a reference spectrum off a gold sample is taken for each new tip. The scattering of gold in the mid-infrared frequency range can be seen as uniform across the probe pulse bandwidth, such that the scattered spectrum truly reflects the spectral shape of the radiation coupled to the sample. Such a reference spectrum is shown in Fig. 3.8a. The scattered near-field amplitude s_3 is plotted as a function of frequency. Similar to the intensity resolved measurements, the subscript indicates the demodulation order of the signal and provides a means to suppress background radiation not originating from the near field below the tip. Apart from one local maximum around 37.5 THz, the spectrum follows a Gaussian line shape with a center frequency of 36.3 THz and a width of 6.8 THz (FWHM).

Since the black phosphorus flake is encapsulated in SiO_2 layers in our heterostructures (see Fig. 3.1), the spectral signal of SiO_2 is important to be known for further evaluation of the heterostructure's response. Therefore, the scattered amplitude spectrum $s_3(\nu)$ of the SiO_2 substrate, away from any heterostructure is depicted in Fig. 3.8b in blue. The gold spectrum of Fig. 3.8a is shown for comparison and is shaded in red. There are strong differences between the SiO_2 response and the gold spectrum. Most notably, the spectrum is much narrower, only selecting frequencies around 33.8 THz. At this frequency point, the scattered amplitude is as large as the one on gold. The line shape around this point is not Gaussian as for the probe spectrum, but follows a Lorentzian distribution – typical for a homogeneously broadened material resonance. The width is 2.3 THz, i.e. only a third of the incoupled band-

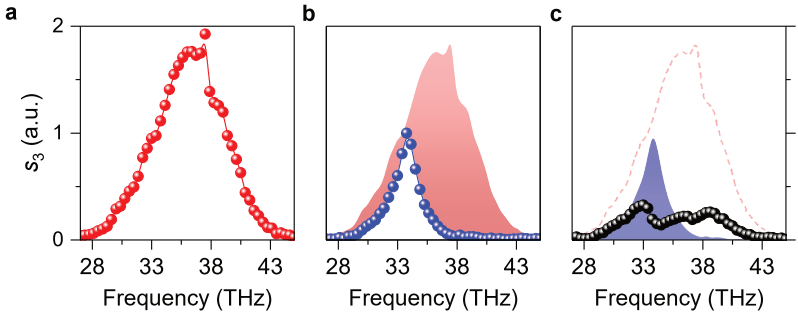

Figure 3.8. | Equilibrium spectral response of gold, the heterostructure and the substrate. Plotted is the scattered spectral amplitude s_3 for different materials. **a)** The scattered response from a spectrally-flat gold surface is shown, closely corresponding to the near-field probe spectrum. **b)** On the SiO_2-covered silicon wafer the response is narrowed strongly (blue points and connecting line) compared to the gold spectrum (red shaded area) due to a phonon resonance at 33.8 THz. This maximum value of the spectrum is used as a normalization for all spectra. **c)** The black phosphorus heterostructure shows a distinctly different spectral response even prior to photo-excitation (black points) than the SiO_2 (blue shaded area) and the gold spectrum (red dashed line).

width. This resonance in the near field has already previously been reported (e.g. by [Fei11]) and attributed to the surface phonon in SiO_2. A practical advantage of the strong scattering of the substrate caused by a resonance in near-field microscopy is that it can be used to enhance the near-field signal and, hence, the contrast in the spectral vicinity [Aiz08].

Even though the black phosphorus flakes are encapsulated in silicon dioxide, the spectrum of the full heterostructure differs significantly from the bare SiO_2 spectrum even in the unexcited case. Figure 3.8c shows the spectral amplitude as a function of frequency taken on the spot circled in Fig. 3.2 and Fig. 3.4. In addition to the heterostructure data (black points) the sharp resonance of the SiO_2 substrate (blue shading) and the gold spectrum (red dashed curve) are visualized. For low frequencies, the amplitude follows the shape of the SiO_2 resonance. There is still a resonance close to the one of the SiO_2 substrate. However, its shape is no longer

Lorentzian and the peak is shifted to lower frequencies ($\approx 33\,\mathrm{THz}$). Furthermore, the spectral weight does not decrease for frequencies above the SiO_2 surface phonon, but instead continues to rise and shows two more local maxima at 36.8 THz and 38.6 THz before it falls off towards high frequencies. Due to this flat shape, the FWHM measured from the lowest frequency maximum is 9 THz and therefore much broader than the resonance of the substrate.

As a next step, we want to see the dynamical change of the spectrum upon photo-excitation because these changes will yield insight into the properties of the surface polariton imaged in Fig. 3.6, which is absent in equilibrium. For this reason, the tip is kept on the same position where the equilibrium response of the heterostructure in Fig. 3.8c has been recorded. In these new measurements, though, the pump pulses illuminate the sample and spectra are recorded as a function of the delay time between the pump and probe pulses. The results are displayed in Fig. 3.9. The complex-valued spectral data obtained via FTIR are normalized to a dataset taken at negative delay times ($t_{\mathrm{pp}} = -10\,\mathrm{ps}$) to only show the pump-induced change to the signal. In the left column the amplitude of the change as a function of frequency is plotted and in the right column the change in the phase. The data are offset vertically for better visibility and the delay times match the ones of the ultrafast real-space snapshots in Fig. 3.6 (except for the latest delay time), which allows us to correlate the evolution of the mode's frequency and wavevector throughout its entire lifetime.

Concentrating on the pump-induced changes to the scattered amplitude first, we see two dominant processes going on. The first is the emergence of a prominent peak at around 34 THz (indicated by red shading). This effect is prominently visible for delay times from 0 to 3 ps. In this time window the maximum redshifts slightly towards 33.8 THz for increasing delay times. The second major feature is a suppression of the scattered amplitude (blue shaded areas) at frequencies above the (red shaded) enhancement region. The suppression is fairly uniform for all high frequency components with a minimum that is much less prominent than the maximum in the region of increased scattered amplitude. The suppression takes place for times from 0 to 4 ps and is present longer than the increase of the scattered intensity near 34 THz. At negative times there is no change – as expected. Furthermore,

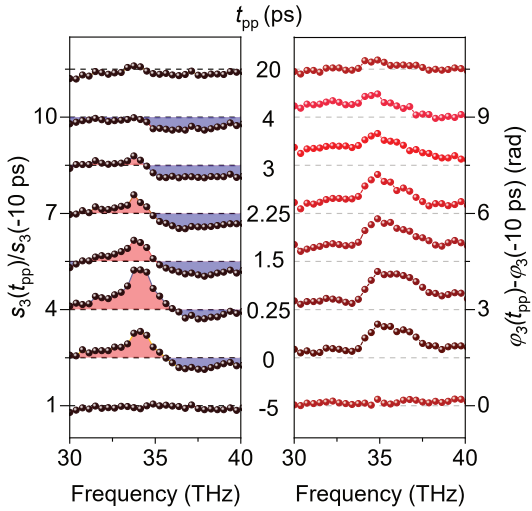

Figure 3.9. | Spectral evolution of the photo-excited sample. The photo-induced spectral change to the amplitude s_3 and relative phase ϕ_3 of the near field scattered off the heterostructure is plotted. The data are normalized to the values at pump-probe delay time t_{pp} of -10 ps and are taken at the position marked in Fig. 3.4. Additionally, the curves are offset for clarity.

20 ps after photo-excitation any changes with respect to the equilibrium response have again decayed, which is in perfect agreement with the timescales observed in the intensity-resolved pump-probe measurement (Fig. 3.3).

As a consequence of the two opposite effects of enhancement and suppression in the different regions of the spectrum there is one intermediate frequency ν_{0C} at which the pump-induced change is zero (i.e. the divided spectra show a value of 1). This point shifts from 35.7 THz at $t_{pp} = 0$ up to 36.2 THz at the maximum signal of the pump-probe scan (i.e. $t_{pp} = 250$ fs) and subsequently redshifts for increasing delay time down to 34.5 THz at $t_{pp} = 3$ ps. Such a behavior is typical for a resonance like the plasma frequency shifting into the probe spectrum and back, as it leads to an enhancement below the resonance and a suppression above (see [Eis14] or [Eis15] for more details). However, the pinning of the maximum enhancement at a single frequency of ≈ 34 THz is unexpected and another indicator that the phonon in the SiO_2 layers have an additional impact on the polaritonic mode of the system. Taking the unexcited spectra of SiO_2 and the heterostructure into account, the photo-activation seems to strengthen the response close to the SiO_2 phonon resonance, which is suppressed in the unexcited heterostructure.

The change in phase follows the assumption of an optically coupled mode, as it features the typical dispersive shape associated with a resonance. Correlating the amplitude and phase, one sees that for delay times from 0 to 4 ps the spectral position of ν_{0C} is close to the maximum in the phase for each delay time. This evidence corroborates the existence of a shifting plasmonic resonance in the structure.

In the next section a theoretical model is developed that allows us to fully understand the experimental findings shown above. It explains the existence of the peculiar polariton mode, which has both a plasmonic and a phononic character and can be switched on ultrafast timescales via photo-excitation. Also the strong confinement of the polariton mode in momentum and frequency, which has been observed throughout the lifetime of the mode, is elucidated.

3.5. Theoretical description of the mode as a hybrid interface phonon-plasmon polariton

In this section, a theoretical model will be developed step by step to calculate and understand the dispersion of the switchable polariton mode observed in experiments. As a starting point, I will introduce an intuitive picture of the switching process based on the theory of surface bound modes developed in chapter 2. This intuitive picture is conceptually useful, but is not sufficient to quantitatively explain all of our observations. These shortcoming highlight that further theoretical sophistication is required for a full description of the experimental phenomena. For example, one prominent (and crucial) new aspect introduced below is the splitting of polariton modes in thin films. With this new knowledge, the dispersion relations of the mid-infrared polariton modes in the heterostructure are calculated. These are then discussed in detail and the unexplained experimental features are resolved.

3.5.1. An intuitive picture

From our discussion about surface polaritons we know that an essential part determining the existence of surface polaritons is the sign change of the dielectric

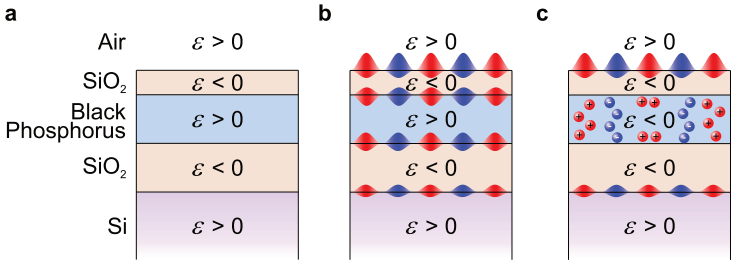

Figure 3.10. | Intuitive picture of mode switching. The layered structure of the heterostructure is sketched including the overall sign of the dielectric function in each layer. **a)** A description of the layers including the sign of the dielectric functions ε. **b)** Potential interfaces at which surface polaritons can form in the unexcited structure. **c)** Change to the polariton composition upon photo-excitation.

functions across interfaces. Equation set 2.12 states that for the existence of a polariton, the two dielectric functions need opposite signs and the negative one must be larger than the positive one in absolute magnitude. As a first approach, we can use this information to treat each interface in our heterostructure separately and check where surface bound modes can exist. In Fig. 3.10a, the layers are shown schematically and each layer has been assigned a sign of the dielectric function for the unexcited case. The dielectric functions of air and silicon are flat in our spectral range and always positive. For the silicon dioxide layers, a prominent phonon resonance has been measured in the spectral bandwidth of the probe pulses. Between the TO and LO phonon frequencies the dielectric function is therefore negative. A model dielectric function based on literature references is shown in appendix C, including pictographs of the characteristic motion of different phonon modes. Modeling the black phosphorus as a Drude material with very few free carriers leads to a positive dielectric function in our probe bandwidth in the unexcited case. From this estimate and without detailed consideration whether the difference between the dielectric functions is large enough, the interfaces which potentially support surface waves can be determined and are shown in Fig. 3.10b. In this schematic the wavelengths, magnitudes and relative phases between the modes are not to scale but serve to visualize the concept. As can be seen, surface phonon polaritons are possible at each SiO_2 interface. Probing only the near fields at the surface and having the

two silicon dioxide layers separated by a thick black phosphorus layer with only a positive dielectric response, we can neglect the influence of the lower SiO_2 polaritons in our consideration for the unexcited case. Despite the expectation that surface phonon polaritons are present, we do not see a fringe pattern on the unexcited sample in our experiments. There are different possible explanations. The most likely explanation is that the mode cannot be probed due to a missing dielectric contrast at the edge. This inhibits a reflection of the mode and renders the detection using the near-field echolocation measurement impossible. Another possible explanation might be that the broadband probe pulse launches surface phonon polaritons with a broad bandwidth of in-plane momenta. These polaritons potentially do not interfere constructively at a distinct wavelength but lead to a homogeneous scattering signal.

Upon photo-excitation of the black phosphorus, the only quantity changing in our simple picture is the dielectric function of the black phosphorus layer. Assuming we induce a sufficiently high carrier density to shift the plasma frequency inside our probe spectrum, near-infrared photo-excitation leads to a negative dielectric function for certain mid-infrared probe frequencies. This assumption seems reasonable since in the experiment the spectral shape of the scattered probe amplitude changed as a function of time after pump photo-excitation, including a shift of the zero change position ν_{0C} (Fig. 3.9), reminiscent of what has been observed for ultrafast near-field spectroscopy of a photo-excited semiconductor [Eis14]. As a consequence, the possible interface modes in the structure change drastically with near-infrared photo-excitation (Fig. 3.10c): The polaritons at the silicon dioxide/black phosphorus interfaces that existed in the unexcited structure vanish, as the necessary conditions for surface polaritons are no longer fulfilled (equation 2.12). The only remaining polariton above the black phosphorus is the surface phonon polariton at the top surface. Surface phonon polaritons have a rather long wavelength compared to surface plasmon modes and travel typically farther due to the high quality factor of the phonon resonance. This could explain the long propagation lengths measured in the experiment as well as why the spectral changes in the amplitude upon photo-activation take place close to the SiO_2 phonon resonance of the substrate. Following the argument above, surface waves with a single wavevector can now be measured for two reasons. Due to the strong change in the dielectric function of black phosphorus,

the dielectric contrast at the edge increases and leads to a measurable reflection of the polariton. Additionally, a specific k_x-vector must be favored in the combined structure to see a standing wave pattern in the excited case. This selection happens due to the plasmonic contributions in the Drude material, which break the symmetry between the different k_x-vectors supported by the surface phonon polariton. The full mode is, hence, a combination of the surface phonon polariton and the plasmonic response in the black phosphorus layer. Only the coupling of both contributions can qualitatively explain the observed standing wave pattern with a fixed in-plane momentum.

Summarizing, this straightforward model based on the sign of the dielectric functions in the unexcited and photo-excited case can qualitatively explain why a surface polariton mode with an unexpected long travel distance is seen upon photo-activation. However, at the current level the model can explain the selection of k_x-vectors in the experiment (snapshot images in Fig. 3.6 and line profiles in Fig. 3.7a) as well as the exact spectral response only in a hand-waving fashion. Nevertheless, the overall idea is sound and will be underpinned with quantitative calculations in the following subsections.

3.5.2. Thin-film effects

As an intermediate step before calculating the dispersion of the full heterostructure, it is essential to understand the intricate interplay of multiple surface polaritons in layered structures. This is an exciting topic in both the mid-infrared and terahertz spectral domain, for example when the formation of an acoustic plasmon has been reported by coupling of a surface polariton in graphene to a metal [AG16]. However, the same physical effects can also be studied at the surfaces of a single material.

In the theoretical description so far only one interface has been considered with infinite half-spaces of material one and two at each side. However, visualizing the dispersion via the imaginary part of the Fresnel reflection coefficient allows one to obtain the dispersion for multi-layered systems. A straightforward extension of the analytical model describing two semi-infinite media is a single medium with thickness d sandwiched between two infinite half-spaces with the same dielectric

function. An example would be a thin metal plate in air. In this case, surface plasmon polaritons can form on either side of the metal and the dispersion of the system changes depending on the thickness of the slab. For a large thickness, the two surface polaritons can be treated separately and the semi-infinite half-space approximation is valid. This leads to the well known dispersion of a surface plasmon polariton as discussed in section 2.1.2 for the modes on each interface. The analytical dispersion for such a material whose dielectric function is described by the Drude model is depicted in Fig. 3.11a as orange line. For a thin metallic film, the electric fields of the surface waves on adjacent interfaces can interact with one another. The resulting dispersion is visualized via an $\mathrm{Im}(r_\mathrm{p})$ calculation for a 500-nm-thick sheet in Fig. 3.11a as a false-color plot. To show the qualitative trend, the k_x-axis is given in units of the inverse of the material thickness.

Comparing the solution for an infinitely thick material (orange line) with the dispersion for a thin sample, visualized via the maxima in $\mathrm{Im}(r_\mathrm{p})$, a splitting of the surface polariton into two branches is seen for the thin film. The two branches start at the same origin as the bare surface plasmon polariton. For increasing in-plane k-vector, however, they strongly separate in frequency towards the plasma wavevector k_Pl, which is marked by a vertical white dashed line. The plasma wavevector is defined by $k_\mathrm{Pl} = 2\pi\nu_\mathrm{Pl}/c$ and only depends on the plasma frequency of the material ν_Pl and the speed of light c. For even larger in-plane wavevectors k_x the splitting of the two polariton branches decreases again until they finally asymptotically tend towards $\nu_\mathrm{Pl}/\sqrt{2}$ for infinitely large momenta.

E. N. Economou solved this problem analytically, giving equations that describe the dispersion of each branch at low and high k-vectors [Eco69]. The corresponding lines – calculated for the thickness and dielectric function of the metal slab described above – are added to the graph as black curves. The good agreement with the numerical calculation shows that the visualization of polaritonic modes via $\mathrm{Im}(r_\mathrm{p})$ is also valid for thin films.

It has been seen, that the product $k_\mathrm{Pl} \cdot d$ determines the strength of the splitting. For $d \ll 1/k_\mathrm{Pl}$ the branches diverge strongly whereas for $d \gg 1/k_\mathrm{Pl}$ they converge to the bare surface plasmon dispersion. For very thin samples the upper branch can even reach the plasma frequency ν_Pl at k_Pl. Furthermore, his study shows that

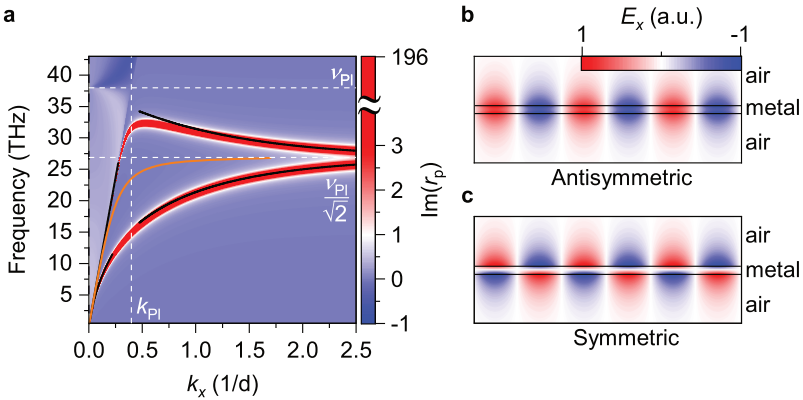

Figure 3.11. | Thin-film effects on surface plasmon polaritons. a) The splitting of the surface plasmon polariton at a single interface (orange line) due to the hybridization of two surface polaritons in a material slab with thickness $d = 500\,\text{nm}$ is visualized using the imaginary part of r_p. The branches can also be modeled analytically [Eco69] for small and large k-vectors and the resulting lines are plotted in black. A Drude dielectric function with a plasma frequency $\nu_\text{PI} = 38\,\text{THz}$ and a damping $\gamma = 1.5\,\text{THz}$ was used. The white dashed lines indicate the plasma frequency ν_PI and $\nu_\text{PI}/\sqrt{2}$ as well as the plasma wavevector k_PI. **b), c)** Schematic field profile E_x of the antisymmetric (symmetric) higher (lower) energy branch in b (c).

the difference between the upper and lower branch is in fact the symmetry of the polaritons' electric and magnetic field distributions. The higher frequency branch is called antisymmetric, where the nomenclature originates from the magnetic field distribution. In Fig. 3.11b a schematic of the x-component of the electric field distribution of the coupled antisymmetric mode is shown for one representative k_x-vector. The horizontal black lines indicate the interfaces between which the metal is located, with air above and below. The field is color-coded, where blue indicates negative fields and red positive fields. In this configuration positive (negative) fields in the top layer align with positive (negative) fields in the bottom layer. As the fields inside the material are correlated to an area with an effective charge surplus or shortfall, the alignment of two of these areas with the same sign of the electric field at both sides of the material leads to an additional repulsive force, which is the

reason why the mode is shifted towards higher frequencies. For the lower polariton branch, which is sketched in Fig. 3.11c, the arrangement of charges is such that at one location both surfaces show opposite signs, leading to an attractive interaction, which reduces the energy and thus frequency of the mode. In an intuitive picture, a stronger overlap of the surface mode field distribution leads to a larger splitting. This can either be achieved by minimizing the thickness of the material or by changing the wavelength of the surface plasmons. For small k_x the wavelength increases naturally, leading to a stronger splitting for smaller k_x because the extension of the evanescent field along the z-direction increases (see equation 2.26). For in-plane momenta below k_{Pl} both branches curve towards the light line.

Surface phonon polaritons on the adjacent interfaces of a thin dielectric film can also interact, forming an analogous coupled oscillator system similarly characterized by two separate branches in the dispersion diagram of the film. This is the case for the 5-nm-thick cover layer of SiO_2 on the heterostructures (see Fig. 3.1). As a consequence, all surface polaritons in the heterostructure that originate from a coupling of light to an LO phonon are energetically split into lower and upper polariton branches. Therefore, in our intuitive model from the previous section, the switching of the black phosphorus and – in the simple picture – elimination of the surface phonon polariton at the black phosphorus/SiO_2 interface changes the thin-film splitting in the top SiO_2 layer and, hence, the dispersion of the full structure. To understand this process in more detail, and especially at what wavevector the change appears, the possible polariton branches and full polariton dispersion of the heterostructure is calculated in the next section.

3.5.3. Dispersion of the full heterostructure

For an exact description of the potential polariton modes hosted by the black phosphorus heterostructures all constituent layers have to be incorporated in the modeling.

To visualize points in frequency and in-plane wavevector where optically active resonances appear, the imaginary part of r_{p} is calculated for a five-layer structure using a transfer-matrix method (see appendix B). In this formalism, the reflection

coefficient can be calculated for layers of known thickness between two infinite half-spaces. These top and bottom half-spaces are air and silicon in the experiment, as the extension of the silicon waver is much larger than the other relevant length scales (0.38 millimeter compared to 1 to 100 nanometers). Moving upwards from the silicon wafer, the 300-nm-thick SiO_2 buffer layer is included, followed by the black phosphorus flakes (see Fig. 3.1 for the full structure). The height of the black phosphorus layer is chosen such that it matches the experimentally measured height of the particular heterostructure it is compared to. Finally, the 5-nm-thick capping layer of SiO_2 above the flake is added before the interface to air. For air and silicon, constant values of the dielectric function are used ($\varepsilon_{\mathrm{Air}} = 1$ and $\varepsilon_{\mathrm{Si}} = 11.9$ [Mad04]) and for silicon dioxide literature values [Gun00] are chosen with a slightly reduced damping to reproduce experimental data [Fei11]. The black phosphorus is modeled using the previously described Drude model with a variable plasma frequency defined by the number of free carriers in the black phosphorus, which is affected by the pump fluence and pump-probe delay time (see section 3.2). The precise details of the dielectric functions can be found in appendix C.

Calculating the dispersion of the heterostructure in the unexcited and photo-excited case

To obtain the polaritonic modes of the system in the unexcited state a low plasma frequency ($\nu_{\mathrm{Pl}} = 10\,\mathrm{THz}$) is used. The resulting dispersion is shown in Fig. 3.12a. Here, the flake height was set to 110 nm, which corresponds to the height of the heterostructure shown in Fig. 3.2. In the dispersion graph there are three areas of interest. At very low frequencies (0 to 10 THz) the surface plasmon response of the thin black phosphorus layer can be seen by tracing the maxima in the imaginary part of r_{p}. The surface plasmon polariton response is split into two branches (marked by SPP^+ and SPP^- in Fig. 3.12a) as discussed in the previous section. Because the flake is relatively thin, the upper polariton branch SPP^+ almost touches the plasma frequency of $\nu_{\mathrm{Pl}} = 10\,\mathrm{THz}$ and is notably stronger in its response than the low frequency branch SPP^-.

Slightly above, in the range from 13 THz to 15 THz, there are two modes associated with the lower Reststrahlen band in SiO_2. The almost horizontal mode at small

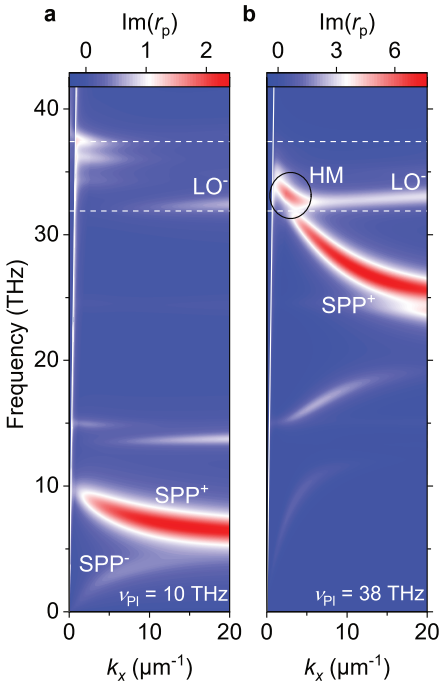

Figure 3.12. | Dispersion of the full heterostructure. Color-coded is the imaginary part of r_p as a function of frequency and in-plane wavevector k_x. **a)** To simulate the unexcited structure a low black phosphorus plasma frequency is used ($\nu_{Pl} = 10\,\mathrm{THz}$). The black phosphorus surface plasmon polaritons split into a lower energy (SPP^-) and a higher energy (SPP^+) branch at low energies. Each of the multiple phonon polaritons in the different SiO_2 layers are seen, where some are split into upper and lower energy branches. The lowest energy branch of the lowest energy LO phonon in the upper Reststrahlen band (dashed lines) is labeled (LO^-). **b)** The excited sample is modeled with a high plasma frequency of $\nu_{Pl} = 38\,\mathrm{THz}$. In this case the hybrid mode (HM) emerges, which is indicated by the black ellipse.

in-plane wavevectors is due to the phonon in the thick buffer layer. At large k_x-vectors the slightly dispersive polariton is the lower branch of a thin-film-split surface phonon polariton in the 5-nm-thick SiO_2 cover layer. A very faint influence of another split phonon can be seen at 24 THz where another phonon is located in amorphous SiO_2.

Finally, the most important part in the dispersion is the region where our probe spectrum resides (30 to 40 THz). A very rich mode spectrum is already visible in the unexcited case due to the wide upper Reststrahlen band of SiO_2, extending from 31.9 THz to 37.4 THz (white dashed lines [Gun00]). Analogous to the lower Reststrahlen band, at small wavevectors the influence of three unsplit modes due to

phonons in the SiO_2 substrate is seen. Additionally, one prominent mode is located at the lower edge of the Reststrahlen band for larger k_x-vectors. This mode is the lower branch (LO^-) of the lowest-lying split surface phonon polariton mode in the top layer. In the real-space imaging experiments the mode is not seen, potentially because of its broad k_x-vector distribution and low oscillator strength compared to the surface plasmon polariton, which renders it undetectable using the echolocation method of launching and detecting of the polaritons via interference with near-field microscopy (see explanation in section 3.3 and also section 3.5.1 regarding the missing dielectric contrast for polariton-reflection).

Photo-excitation using the near-infrared pump radiation generates free carriers in the black phosphorus layer. This effect can also be modeled theoretically by increasing the plasma frequency within the Drude model used to describe the black phosphorus layer in the calculation. Setting the plasma frequency to 38 THz results in the mode profile shown in Fig. 3.12b. Generally speaking, the split plasmon branches move towards higher frequencies as the plasma frequency is increased. The upper mode remains close to the plasma frequency as it increases, such that the upper mode occupies the SiO_2 Reststrahlen band (31.9 THz to 37.4 THz) for a plasma frequency of 38 THz. The lower surface plasmon polariton, meanwhile, curves towards $\approx$ 22 THz, which is a smaller value than the plasma frequency divided by $\sqrt{2}$ ($\approx$ 26.9 THz). This is because the SiO_2 layers surrounding the black phosphorus, which have a larger dielectric constant than air, lead to a different dielectric screening. Interestingly, the lower plasmon polariton shows an anticrossing behavior with the lower frequency phonons and avoids the frequency range from 11.5 THz to 15 THz.

The exact opposite happens at the high-frequency Reststrahlen band. Here, the upper surface plasmon polariton branch not only enters the band, but it also couples strongly to the lower split surface phonon polariton branch LO^-. The oscillator strength of the LO^- branch is strongly enhanced, which can directly be seen by the increase in magnitude of $\mathrm{Im}(r_p)$. At the intersection point a strongly confined region of high oscillator strength is created at $k_x \approx 2.8\,\mu m^{-1}$ and a frequency of 33 THz. This new hybrid mode between the surface plasmon polariton and the surface phonon polariton LO^- also involves the lowest of the phonon resonances

at around 33.9 THz, which stems from the phonons in the thick substrate oxide layer below the black phosphorus. The difference between the anticrossing behavior in the region from 13 THz to 15 THz and the coupling for higher frequencies is founded in the different electric field overlap and depends on the mode profiles of the contributing excitations. Similar effects have already been described in graphene coupled to hexagonal boron nitride and silicon dioxide [Cal16]. There, the coupling of surface plasmons on graphene to phonon polaritons in hexagonal boron nitride and silicon dioxide layers has been theoretically explained. However, the resulting coupled modes show a broad extension in frequency and strong dispersion. Localized regions of enhanced oscillator strength in frequency and wavevector are so far unique to the structures presented in this thesis.

From a fundamental point of view, in the region in frequency and momentum where the hybrid mode is located for the excited structure, no resonant features are found in the unexcited case. Therefore, the process of photo-excitation indeed *creates* a hybrid mode, which was absent previously.

These newly generated polaritons appear in the frequency-momentum region where also the experimentally observed mode is located: The points in the dispersion of the hybrid mode that show the highest 25% of all values of calculated oscillator strength are concentrated in an area with frequencies between 32.4 THz to 34 THz and in-plane wavevectors ranging from 1.5 µm^{-1} to 4.5 µm^{-1}. Comparing to the experiment, the strongest photo-induced change is observed at a frequency of 34 THz, with a slight redshift towards 33.8 THz for late delay times (see Fig. 3.9). On the other hand, the experimentally observed in-plane wavevector is 3.84 µm^{-1} (Figs. 3.4 and 3.6 and the later section 3.7) and is, hence, larger than what is theoretically expected at this frequency. Nevertheless, the value itself is within the range of the supported k_x-vectors (i.e. in the region with the 25% highest values of oscillator strength). A direct comparison between theory and an experimentally measured dispersion will be shown in section 3.6, where also the origin of the difference will be addressed.

Interestingly, the area of increased oscillator strength only emerges from the calculation when all aspects of the heterostructure are included, such that the surface phonon polariton modes in the two SiO_2 layers are coupled through the collective oscillation of the two surface polariton modes in the thin sheet of black phospho-

rus. This exact point of the intersection of all bare polaritons is confined strongly in frequency and momentum and obtains its oscillator strength from the plasmon oscillations. This is expected, since even for low plasma frequencies the oscillator strengths of the surface plasmons far exceed those of the surface phonons, as evidenced by the magnitude of $\mathrm{Im}(r_\mathrm{p})$ in Fig. 3.12a. The plasmonic response is also the essential constituent that makes the mode switchable due to the change in the surface plasmon polariton dispersion upon injection of free carriers by photo-excitation. However, the phononic character of the mode also lends the hybrid mode advantageous properties, since surface phonons typically have lower losses than surface plasmons and lead to the high quality factor of the hybrid interface mode. A closer investigation of the influence of the phononic and plasmonic character on the propagation distance of the hybrid mode can be found in section 3.7.

In summary, only a sophisticated interplay of the phononic and plasmonic parts produces the experimentally observed polaritons with well defined wavevector and frequency.

Dispersion calculations for different plasma frequencies to explain the time dynamics of the polariton

In the experiment we have seen that the energy and the momentum is fixed for all pump-probe delay times where the polariton is observed. To find the reason for this behavior, the temporal evolution of the mode's dispersion shall be investigated theoretically and compared to the measured data. To do so, the polariton dispersion diagram visualized by the imaginary part of r_p is calculated for a range of plasma frequencies. This corresponds to different carrier densities, which arise due to different pump fluences or measurements taken at different pump-probe delay times in the experiment. After photo-excitation with the pump pulses the plasma frequency increases due to the generation of free electrons and holes. Carrier cooling inside the conduction band leads to a further increase in the plasma frequency, as the average effective mass of the carriers decreases towards the band minimum (see also section 3.2 and especially the discussion of Fig. 3.3). Subsequent carrier recombination in the material leads to a reduction of the plasma frequency compared to

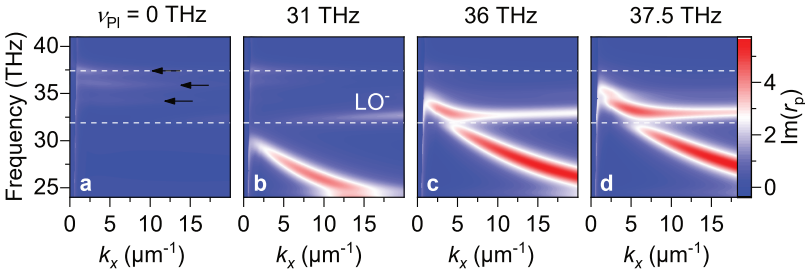

Figure 3.13. | Emergence of the hybrid polariton. The calculated dispersion of the polariton in the heterostructure is visualized via the imaginary part of the Fresnel reflection coefficient r_p in the relevant spectral range of the experiment for plasma frequencies ν_{Pl} of **a)** 0 THz, **b)** 31 THz, **c)** 36 THz and **d)** 37.5 THz. The borders of the upper SiO_2 Reststrahlen band are indicated by white dashed lines. The three substrate phonon modes are indicated by black arrows in **a** and the lowest split surface phonon mode LO^- is indicated in **b**. The black phosphorus layer is modeled with a height of 53 nm for all panels.

the maximum value. The results for four different plasma frequencies are plotted in Fig. 3.13. For the unexcited structure, i.e. a plasma frequency of 0 THz (Fig. 3.13a), the rich phonon spectrum observed in Fig. 3.12a is reproduced with more resolution, featuring three modes at small k_x vectors (marked by black arrows). The LO^- mode (marked in Fig. 3.13b) is faintly visible at higher in-plane wavevectors. This broad band of resonances originates from a complex interplay between the modes of the SiO_2 cover layer and substrate, wherein thin-film effects are a crucial aspect. These interactions are potentially the reason for the wide bandwidth of the spectrum we have observed in the heterostructure at equilibrium (Fig. 3.8c). Furthermore, since the lower split phonon branch LO^- strongly contributes to the scattered spectrum (especially for large k_x-vectors) and the upper branch is not visible in the calculation, the frequency of the lowest frequency phonon peak is consistently redshifted compared to the bare SiO_2 spectrum in theory and experiment.

Shifting the plasma frequency to higher energies, namely up to the lower edge of the Reststrahlen band (Fig. 3.13b), leads to an interesting effect on the phonon polariton modes. The increase of carriers inside the black phosphorus starts to screen the

contributions of the thick silicon dioxide substrate, leading to a pronounced suppression of the higher frequency surface phonon branches. Since the surface plasmon mode and the substrate phonon modes have no overlap in energy and wavevector yet, a constructive coupling is inhibited. Therefore, the spectral components of the phonon modes at the interface between substrate and black phosphorus at low in-plane momenta are suppressed in the reflection coefficient as the number of free carriers increases in black phosphorus, which turns the material character more metallic and less transparent. This phenomenon is seen in the ultrafast spectral response of the heterostructure shown in Fig. 3.9, where a strong suppression of the high frequency components was observed (blue shading). Here it should be stressed that after the peak of the pump-probe measurement ($t_{\mathrm{pp}} \approx 250\,\mathrm{fs}$, Fig. 3.3), the carrier density and hence plasma frequency decreases with time. Hence, later delay times correspond to a lower plasma frequency. The experiment shows that the reduction of the high frequency components is still visible at late delay times ($t_{\mathrm{pp}} = 4\,\mathrm{ps}$, Fig. 3.9) even though the hybrid polariton mode has already mostly vanished (see also the intensity profile in Fig. 3.6). Another result of the suppression of high-frequency components is the different contrast at $t_{\mathrm{pp}} = 10\,\mathrm{ps}$ compared to the unexcited case at $t_{\mathrm{pp}} = -5\,\mathrm{ps}$ in Fig. 3.6 where the flake is darker relative to the silicon dioxide substrate. The slight enhancement of the LO^- branch due to the surface plasmon seems not to be able to make up for the loss in intensity caused by the suppression of the high frequency phonons. Therefore, also in the pump-probe trace (Fig. 3.3), the scattered intensity drops below the baseline at the pump-probe signal onset $t_{\mathrm{pp}} \approx -0.7\,\mathrm{ps}$ and at late delay times ($5\,\mathrm{ps} < t_{\mathrm{pp}} < 20\,\mathrm{ps}$).

In contrast, the LO^- branch strengthens in the $\mathrm{Im}(r_{\mathrm{p}})$ calculations, when the plasma frequency enters the Reststrahlen band and forms the hybrid mode (Fig. 3.13c). Here, a strong increase in the oscillator strength at the fixed frequency and wavelength of the hybrid mode is observed, which leads to the enhancement of the low frequency spectral components and the emergence of the spectral peak upon photoactivation (red shaded areas in Fig. 3.9). It compensates for the loss of spectral components at high frequencies in terms of the absolute scattered intensity, which is the reason for the strong peak in the scattered intensity seen in the pump-probe measurement ($0\,\mathrm{ps} < t_{\mathrm{pp}} < 5\,\mathrm{ps}$, Fig. 3.3). Consistently, this feature disappears

earlier than the suppression of high frequency components, as the plasma frequency leaves the Reststrahlen band. This perfectly matches the theoretical dispersion in Fig. 3.13, where it was revealed that the suppression starts to take place while the surface plasmon branch is still outside the Reststrahlen band.

A further increase in carrier density does not alter the dispersion strongly (Fig. 3.13d). The location of the hybrid mode is locked by the interplay of its three constituents: the surface plasmon polariton, the LO^- surface phonon and the parts related to the phonon resonance in the silicon dioxide buffer layer. Together, these three form one collective hybrid mode. This coupling to the modes at low momenta in the bottom SiO_2 layer slightly increases for a higher plasma frequency, but the most prominent effect is that the k_x-vector distribution of the mode changes. There is an increase in the amount of supported wavevectors leading to a larger range in supported polariton wavelengths. Experimentally such a superposition of more wavelengths should cause a smearing of the fringe pattern. This is indeed observed in the real space image at the maximum of the pump-probe curve (Fig. 3.6, $t_{\mathrm{pp}} = 250\,\mathrm{fs}$) as a smeared-out feature in the fringe pattern. The theory thus reinforces the prediction of section 3.3, where this phenomenon was mentioned to originate from the change in k_x-vector spread and not carrier diffusion.

Pump-fluence measurements to corroborate the theoretical predictions

We have seen that the predictions of the theory match the experimental findings in the intensity and frequency resolved measurements. Additionally, a complementary approach can be used to investigate the smearing of the interference pattern for elevated carrier concentrations. That is, instead of varying the delay time, one can influence the plasma frequency directly by changing the pump fluence systematically. Here, the timing between pump and probe pulses is kept fixed at the maximum of the pump-probe curve and the pump fluence of the near-infrared pulses is varied using a continuously tunable neutral-density filter. The change of the scattered intensity at a fixed location for different pump fluences is shown in Fig. 3.14a. As expected from theory, the intensity at first decreases due to the suppression of the buffer layer phonon contributions when increasing the fluence (and therefore plasma frequency).

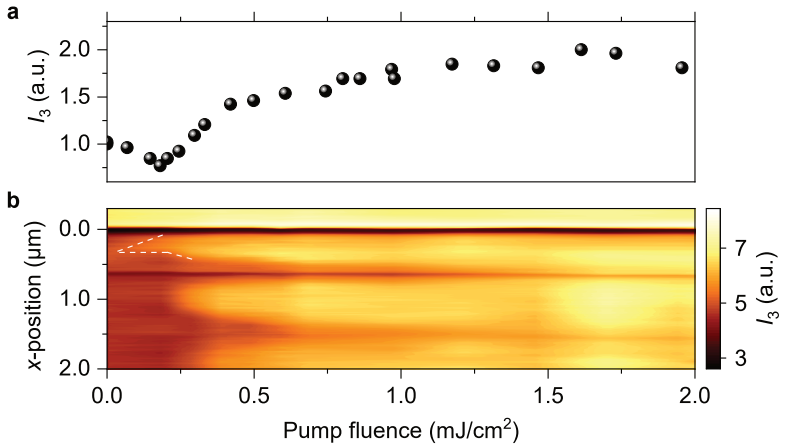

Figure 3.14. | Fluence dependence. Change of the scattered intensity I_3 as a function of pump fluence. **a)** Evolution for one particular tip position. **b)** Development of the fringe pattern for increasing pump fluence along one line perpendicular to the edge of the flake. There is an increase in scattered intensity close to the edge already for small pump fluences (white dashed lines). The data in **a** were taken at $x = 0.2\,\mu\text{m}$ in panel **b**. The flake in this experiment had a height of 53 nm.

The minimum of this trend is reached at $0.18\,\text{mJ/cm}^2$. For higher pump fluences, the creation of the hybrid mode leads to a rebound of the scattered intensity. At a fluence of $0.27\,\text{mJ/cm}^2$ the increase of the low frequency components associated with the LO^- branch and the hybrid mode have compensated for the loss of the high frequency parts. For increasing pump power the intensity keeps rising until a saturation sets in starting in the region around $1\,\text{mJ/cm}^2$. These findings are consistent with experimental observations that $1\,\text{mJ/cm}^2$ is sufficient to observe the hybrid mode without damaging the heterostructures.

Finally, the pump fluence and hence indirectly the plasma frequency can be experimentally linked to the averaged in-plane k-vector distribution of the mode by taking line scans across a single flake edge for various pump fluences. The result is shown below the intensity profile at a fixed spot on the same flake in Fig. 3.14b. Intriguingly, the fringe pattern on the structure only sets in at a fluence of $\approx 0.27\,\text{mJ/cm}^2$.

At this point the intensity increase of the hybrid mode compensates the previous drop. However, already for smaller fluences there is an increase in intensity close to the edge (white dashed lines). This can potentially be attributed to the increase of oscillator strength in the LO^- branch in conjunction with the surface plasmon branch, which starts reaching the Reststrahlen band. The wavevector distribution there is fairly large (see Fig. 3.13b), leading to a short wavelength in real space and only a limited propagation as the coherence length of the plasmon itself is lower than the one of the hybrid mode.

Starting from the appearance of the long wavelength interference pattern associated with the hybrid mode at a fluence of $\approx 0.27\,\mathrm{mJ/cm^2}$, an increase in pump fluence does not alter the wavelength of the pattern, as expected from previous measurements and theory. The smearing in x as a result of the broader k_x-vector distribution becomes obvious when increasing the fluence up to the saturation regime. From this point on the different fringes are only separated by a thin region of low intensity. I want to stress that the location where the previous intensity measurement was taken ($x = 0.2\,\mu\mathrm{m}$) was chosen such that it was right on the center of the first interference fringe. Therefore, a change in fringe width does not compromise the results of the previous discussion of Fig. 3.14a.

In summary, we have seen that the experimental findings can be explained theoretically by the creation of a hybrid phonon-plasmon polariton. In the experiment real space data can access the k_x vector distribution of the mode whereas spectral measurements are sensitive to the energy of the polariton. In the next section, both techniques will be combined to obtain a hyperspectral map, which allows us to extract the dispersion experimentally and compare it to the theoretical calculations.

3.6. Experimentally accessing the dispersion of the hybrid mode

To compare the theoretical calculations with the experiment, a method called hyperspectral imaging is used to measure the dispersion of the observed mode. The technique relies on the echolocation-like interference patterns that can be measured

in real-space using near-field microscopy and combines them with additional spectral information. In other words, instead of only resolving the scattered intensity across the interference fringe pattern, the spectral amplitude and phase at each frequency is recorded at each point in space. A sketch of how this measurement process can be implemented and how it allows one to access the polariton dispersion is depicted in Fig. 3.15.

The easiest way to understand the procedure is to look at hyperspectral measurements with a sample that shows surface polaritons in equilibrium. This might be the case, e.g., for a sample like graphene with a high carrier density due to electrostatic gating. In this case a fringe pattern can be resolved by moving the tip over a sharply defined edge, such that the tip moves from the substrate to the sample or vice versa (indicated in Fig. 3.15a by a flake with a color-coded fringe pattern on its topography). First, consider the case where hyperspectral measurements are performed sequentially using monochromatic lasers of slightly different frequency for each scan (colored sinusoidal lines in Fig. 3.15a). Every scan yields a delta-function spectral amplitude with spatially dependent intensity. As described in section 2.2, for each laser frequency a different interference pattern of the scattered near-field intensity is obtained, which shows a characteristic wavelength λ_{Pl} due to the dispersion of the polariton. Plotting these near-field wave patterns in a two-dimensional plot as a function of x-position and frequency leads to the complete hyperspectral map (Fig. 3.15b, with three example curves corresponding to particular frequencies highlighted in white). This graph contains all necessary information about the dispersion of the mode as it shows the polariton wavelength for each frequency. To relate these data to the actual dispersion, a factor of two has to be incorporated into the x-axis, as the actual wavelength of the polariton is twice as long as the measured wavelength due to the formation of the standing wave pattern (see equation 2.32). A Fourier transform along the x-axis can subsequently convert the image into a graph of in-plane wavevector k_x and frequency (Fig. 3.15c), which is the dispersion of the mode. In the literature, the Fourier transformed image is typically not calculated, but rather the dominant in-plane wavevector k_x for each measured frequency is extracted and shown as a point over theoretical calculations (as shown for the three example monochromatic lasers in Fig. 3.15. For literature references, see, e.g. [Woe15, Dai14, Dai15]). A severe drawback of using monochromatic lasers

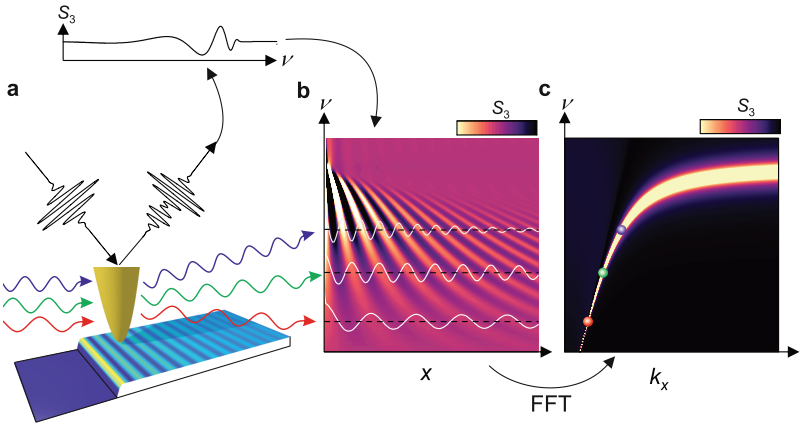

Figure 3.15. | Principle of hyperspectral imaging for dispersion measurements. a) One can either use multiple continuous wave lasers with different wavelengths (sketched red, green, blue) and resolve the standing wave patterns in the amplitude at each frequency separately to end up with a hyperspectral map, or one can use a pulsed source (black incoming and reflected waveform) with a broad spectrum and map the spectral change (plotted at the top of the figure for a single tip position) as a function of distance from the edge of the sample, giving the same map. **b)** Typical hyperspectral map for a surface plasmon. The scattered near-field amplitude is color-coded as a function of position x and frequency ν. The interference patterns for three exemplary wavelengths are highlighted in white. **c)** A Fourier transform of the map along the x-direction results in the dispersion of the polariton that forms the standing wave pattern. The mode dispersion is traced by the maximum of the amplitude as a function of k_x vector and frequency. The colored spheres indicate points on the dispersion extracted from the interference patterns measured with the three monochromatic lasers.

is, however, that they are not capable of resolving dynamical processes, such as the photo-excited black phosphorus heterostructure studied here. Therefore, a different approach must be used for the short lived process we are investigating. Namely, the monochromatic lasers are replaced by ultrashort laser pulses with a broad spectrum (black pulse hitting the tip in Fig. 3.15a). This changes the way the points in the hyperspectral map are obtained. For continuous sources, a measurement at one tip position fills in a single point on the x-ν plot (e.g. Fig. 3.15b). Conversely, since a

pulse is made up of a bandwidth of frequencies, a spectrally resolved measurement at one tip position contains all the information about the scattering near-field amplitude of the frequencies in the bandwidth (Fig. 3.15a, top panel) and fills in an entire vertical line in the x-ν plot. Measuring scattered amplitude spectra using the same input pulses as a function of tip position x yields the full hyperspectral map without the need to change lasers. From then on, the procedure to obtain the dispersion is the same as for the monochromatic approach. The difference is, however, that this method can also be combined with a pump pulse. By recording hyperspectral maps as a function of pump-probe delay time, one can thus map out the transient dispersion of photo-excited samples. The approach was previously used in the pioneering work on graphene [Ni16] where the change to the Drude weight by carrier heating was experimentally determined for two delay times.

For the experiments on the black phosphorus heterostructure, the real-space snapshots (Fig. 3.6) and the ultrafast spectral response (Fig. 3.9) indicate a strong confinement of the hybrid polariton mode in frequency and momentum. To experimentally access the full dispersion of the transient mode and compare it to theory, a hyperspectral map is recorded right at the pump-probe delay time of maximum change to the scattered intensity. The result of the measurement on a $\approx$ 78-nm-thick heterostructure is shown in Fig. 3.16a for a fixed a pump-probe delay time of $t_{\mathrm{pp}} = 250\,\mathrm{fs}$.

The scan was taken across a well-defined edge, with the substrate to heterostructure direction corresponding to increasing x. The change from the substrate onto the heterostructure (at $x = 1.6\,\mu\mathrm{m}$) is strongly visible in the hyperspectral image. The SiO_2 substrate shows the strong phonon resonance that has been seen previously in the equilibrium measurement (Fig. 3.8b). The spectral response here is the same across all points on the substrate. No polaritonic wave patterns can be observed. In contrast, the response of the heterostructure is highly structured for different x-positions owing to the hybrid polariton. An interference pattern similar to the real-space images (see Fig. 3.6) is clearly discernible. However, now the data also contain spectral information. As previously observed in Fig. 3.8 combined with Fig. 3.9, the center frequency of the maximum spectral amplitude on the sample is consistently lower than the resonance frequency of the substrate phonon. This

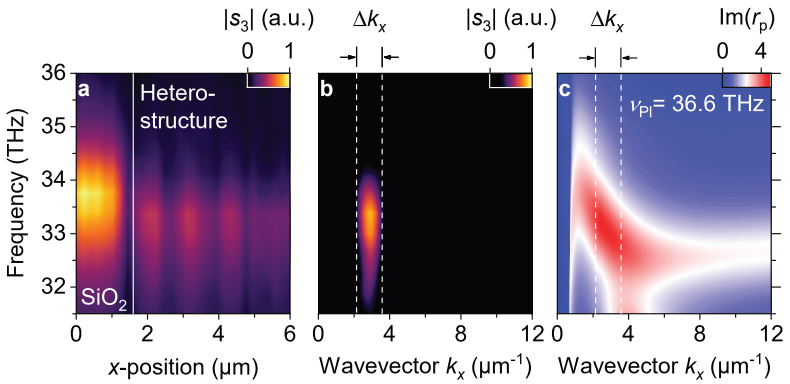

Figure 3.16. | Direct measurement of the hybrid polariton dispersion. **a)** Hyperspectral map across the edge of the substrate to the heterostructure at a pump-probe delay time of $t_{\mathrm{pp}} = 250\,\mathrm{fs}$. The scattered near-field amplitude s_3 is shown as a function of frequency and tip position. **b)** Polariton dispersion, visualized via the scattered amplitude, as a function of frequency and k-vector k_x, which was obtained by a Fourier transformation of the data on the heterostructure in **a** along the x-direction. **c)** Theoretically predicted dispersion of the hybrid mode for a flake with the corresponding height and a plasma frequency of 36.6 THz, visualized via the imaginary part of the Fresnel reflection coefficient r_{p} (similar to the dispersions shown in section 3.5.3).

shows, again, that the splitting of the surface phonon leads to a redshift of the main spectral feature.

Cutting away the substrate parts of Fig. 3.16a (left of white vertical line) gives a hyperspectral plot of only the spectral and spatial modulation of the scattering response of the sample at $t_{\mathrm{pp}} = 250\,\mathrm{fs}$. A Fourier transform including the previously mentioned factor of two results in an experimentally obtained dispersion. This is plotted in Fig. 3.16b. To minimize artifacts from the finite scan window in the Fourier transformation, the data are zero-padded and a running average is subtracted from the data analogous to the procedure described in Ref. [Ni16]. This process eliminates the slowly varying background change in the near-field data but leaves the short wavelength oscillations of the polariton unchanged. As a result one

can clearly see the strongly confined mode of the hybrid polariton. It is confined within a momentum range that is on the order of Δk_x, i.e. the resolution of the scan. This experimental boundary originates from the finite length of the hyperspectral map containing fringes. The finite length results in a finite k_x resolution when doing the Fourier transform.

Comparing the dispersion with a theoretical calculation for a flake of the same thickness and a plasma frequency of 36.6 THz, a good agreement is seen. The extension in frequency and k_x-vector of the mode fits to the experimental data and the k_x center position is well reproduced.

However, there are also differences. Most notably, the center frequency is a little lower in theory compared to the experiment and the dispersion features a tilt in theory but is almost vertical in the experiment. These deviations might stem from the fact that the theoretical calculations and the measurement probe slightly different quantities. The calculations show the bare eigenmodes of the system in an ideal structure, which extends infinitely in the in-plane directions. It can show the dominant effects but not the full picture of the experiment, as the measured data probe the eigenmodes but also include effects due to the finite lateral extent of the system and the measurement technique.

The experimental dispersion has been obtained from the raw scan data, which is a convolution of the input spectrum, the frequency- and momentum-dependent coupling efficiency, and the actual response of the tip-sample system. Therefore, the low frequency components are decreased due to the smaller spectral amplitude in this region. This may lead to the difference in the center frequency of the mode.

In addition to the input spectrum, the distribution of k_x-vectors that is present in the evanescent fields underneath the tip also plays a role in determining the measured dispersion. This distribution affects the launching efficiency of the polariton, depending on its in-plane momentum, and is challenging to quantify experimentally or theoretically. In the literature, it is approximated to be bell-shaped [Fei11] and so far has been assumed to be fairly independent of the frequency for simplicity. However, for a real tip, the incoupling efficiency for different k_x-vectors might vary slightly for different frequencies, which could potentially lead to a different tilt in the dispersion.

Finally, the dispersion in the experiment relies on the interference mechanism of propagating surface waves. Therefore, losses of the material also enter in the measurement. These losses are material-specific and are the main reason why the split surface plasmon polariton SPP^+ is challenging to observe below the Reststrahlen band (see later, section 3.9).

In spite of these considerations, which prohibit perfect agreement between theory and experiment, the observed congruence corroborates the interpretation of a hybrid mode formed by the interplay of phonon polaritons and the surface plasmon polariton.

As a further consistency check between the different experiments, the experimentally obtained dispersion can be correlated with the separately measured spectral (Fig. 3.9) and real-space (Fig. 3.6) data. From the hyperspectral measurement, the phase velocity v_p of the mode can be calculated from the central location of the mode in (k_x, frequency)-space via

$$v_\mathrm{p} = \frac{\omega_\mathrm{center}}{k_{x,\mathrm{center}}} \approx \frac{2\pi \cdot 33.1\,\mathrm{THz}}{2.86\,\mathrm{\mu m^{-1}}} = 72.7 \cdot 10^6\,\frac{\mathrm{m}}{\mathrm{s}} \approx 0.24\,c, \tag{3.1}$$

where c is the speed of light. The propagation distance of the phase front can thus be estimated using the spectral linewidth of the peak in the ultrafast spectral response as a measure of the damping γ_est. From the spectrum at $t_\mathrm{pp} = 0.25\,\mathrm{ps}$ in Fig. 3.9, we obtain a resonance width of $\Delta\omega_\mathrm{est} \approx 2\pi \cdot 1.8\,\mathrm{THz}$ (FWHM). For a Lorentzian resonance, $\Delta\omega_\mathrm{est}$ equals twice the actual linewidth γ_est (for a Gaussian distribution, the factor is $2\sqrt{2\ln 2} \approx 2.355$). Assuming a Lorentzian line shape, the polariton lifetime τ_est of the hybrid mode can be calculated via

$$\tau_\mathrm{est} = 1/\gamma_\mathrm{est} = 2/\Delta\omega_\mathrm{est} \approx 177\,\mathrm{fs}. \tag{3.2}$$

In the numerical simulations of the hybrid mode a plasmon scattering time of 74 fs is used, which is based on literature values (see also appendix C). The lifetime of the hybrid mode is hence significantly increased with respect to the bare plasmonic response due to the coupling to the high-quality phonon mode in the heterostructure.

Multiplying τ_{est} by the phase velocity yields a propagation length of $\approx 12.8\,\mu\mathrm{m}$. For the experimentally observed interference pattern, which originates from interfering polaritons that travel from the tip to the edge and back, a standing wave pattern should be visible for half of that distance, i.e. $\approx 6.4\,\mu\mathrm{m}$. From Fig. 3.6, however, we see that the fringe pattern can only be measured for ≈ 3 - $4\,\mu\mathrm{m}$. To investigate the origin of this discrepancy, we will study the propagation of the hybrid polariton in more detail in the next section and determine whether it is dominantly influenced by phononic or plasmonic contributions.

3.7. Polariton propagation length and phononic characteristics of the mode

Until now, the overall propagation length of the hybrid mode has only been mentioned to be exceptionally long compared to the typical propagation length of mid-infrared surface plasmon polaritons at room temperature [Che12, Fei12, Woe15]. In the previous section, the phase velocity and the damping lead to a propagation length of $\approx 12.8\,\mu\mathrm{m}$. In Fig. 3.4 interference maxima of the propagating mode are seen for distances up to $\approx 4\,\mu\mathrm{m}$ away from the edge – corresponding to a propagation length of $\approx 8\,\mu\mathrm{m}$. From the real-space images for different delay times (Fig. 3.6), we can quantitatively extract the fringe pattern with high signal-to-noise ratio by averaging line scans perpendicular to the flake edge. The results for averaged line profiles at $t_{\mathrm{pp}} = -5\,\mathrm{ps}$, $0\,\mathrm{ps}$, $2.25\,\mathrm{ps}$, and $10\,\mathrm{ps}$ are shown in Fig. 3.17a. The individual line scans were recorded in the region marked in Fig. 3.17b. This area does not contain any topographic irregularities. The left edge of the scan was chosen to match the topographic edge of the flake according to the methods used in [Woe15]. There, the first point of zero inclination following the sharp onset over the edge is defined as the zero for the x-location. At this point the tip has fully reached the top of the flake and hence the measured near-field response is not influenced by potential scattering effects of the flake edge. The right end of the scan range is determined by the beginning of the fold in the flake. The extension of the scan range parallel to the flake edge is chosen to maximize the scan area while minimizing overlap with topographic

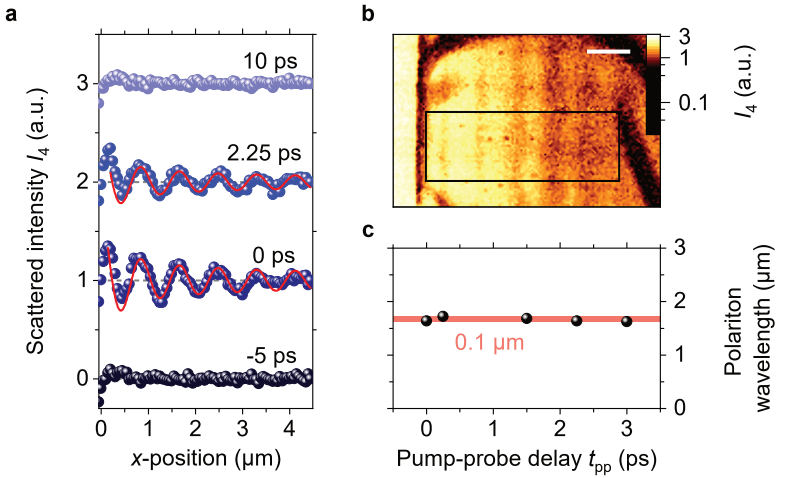

Figure 3.17. | Ultrafast evolution of the polariton wavelength. a) Processed line scans of the scattered intensity as a function of tip position for four different delay times. The lines are obtained by averaging over the area marked in **b** for selected images in Fig. 3.6 including a background correction. Red curves indicate fit functions according to equation 3.7. **b)** Example pattern of the scattered near-field intensity I_4 as a function of position (Fig. 3.6, $t_{pp} = 0.25\,\text{ps}$). Marked is the region which is used for spatial averaging in order to extract the line profiles in **a**. **c)** From the fits to the line profiles (two example fits are shown in **a**), the polariton wavelength can be extracted for each pump-probe delay time. Throughout the lifetime of the mode, all points lie close together, within a 0.1 µm window (highlighted in red).

features. The averages shown in Fig. 3.17a contain no signal modulation for either negative pump-probe delay times or positive delay times $t_{pp} \geq 10\,\text{ps}$ since the hybrid polariton is non-existent in these cases. Right at the time overlap ($t_{pp} = 0\,\text{ps}$) and at $t_{pp} = 2.25\,\text{ps}$, prominent oscillatory modulations are visible in the averaged curves. The raw data contain not only these oscillatory modulations, but also longer-range variations in the background. To isolate the modulations due to polariton interference, a running average is subtracted from the scattered intensity. This processed pattern shows only a single oscillation frequency and decreases in intensity further from the edge of the flake. The oscillatory behavior of the scattered intensity is

still discernible at $x \approx 4\,\mu m$. Since the fringes were resolved using an echolocation technique, this corresponds to a polariton propagation distance of $8\,\mu m$, i.e. from the tip to the edge and back. However, this relationship only holds for tip-launched polaritons. There are also other ways of launching polaritons (e.g. impurities or resonator structures like those in [Dai17]). However, these alternate launching schemes based on a point source would produce an interference pattern that is not aligned parallel to the edge of the sample, so they can be ignored. Apart from these launching mechanisms, the polariton could in principle also be launched directly from the edge of the flake [Dai17, Woe15]. In this scenario, the polariton would be detected by the tip and an interference pattern would be created that is similar to what is seen in the experiments here. Nevertheless, it is unlikely to only have edge launched plasmons when using a metallic probe tip. The strongly reflecting tip is typically more efficient in launching polaritons than the edge: In experiments on 100-nm- to 300-nm-thick hexagonal boron nitride flakes it has been found that the scattering cross section of an SNOM tip is approximately two orders of magnitude larger than the scattering length provided by the edge of the hexagonal boron nitride flakes [Dai17]. There is a differentiation between scattering cross section and length since the tip is a point like polariton launcher, whereas the edge is a line-like launcher. However, both quantities directly determine the coupling efficiency of the respective object. Therefore, in experiments where edge launched polaritons contributed to a large portion of the standing wave pattern, there have also been interference maxima discernible from the tip launched polaritons. They can be differentiated since the edge launched polaritons only have to travel from the edge to the tip and not twice the distance and, therefore, show a different periodicity compared to the tip launched polaritons [Dai17, Woe15]. Consequently, the standing wave pattern typically features two distinct frequencies if edge launched polaritons are present. This is not the case for the measurements on the black phosphorus heterostructures. Therefore, the interference pattern on the heterostructures are expected to be solely tip launched.

Such a tip launched polariton decays as a function of distance (even without any damping). The reason is that the geometrical expansion from a point to a circular wave with increasing radius must be compensated by an amplitude loss of the wave

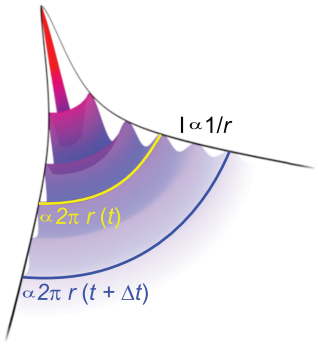

Figure 3.18. | Geometrical polariton decay. Sketched is a part of a circularly expanding polariton wave. For increasing propagation distance, the radius of the angle element of the wave increases from $r(t)$ to $r(t + \Delta t)$. As a result, the circumference increases linearly with r. To conserve the energy of the polariton wave, its amplitude in intensity I must decrease with $1/r$.

to conserve its energy (see Fig. 3.18). For a two-dimensional polariton, the power $P(r)$ as a function of the radius r is the integral of the intensity $I(r)$ along the circumference U of the polariton at a given radius and should be constant:

$$P(r) = \oint I(r)dU = 2\pi r \cdot I(r) \stackrel{!}{=} \text{const.} \tag{3.3}$$

Therefore, the intensity as a function of radius decays with $1/r$. Accordingly, the electric field scales with $1/\sqrt{r}$. However, in our near-field intensity measurements of the surface polaritons (e.g. Fig. 3.17a,b), we actually measure an interference pattern of the incoupled electric field and the edge-reflected electric field of the polariton at the tip position. Hence, the measured intensity as a function of distance from an edge x is given via

$$I_{\text{measured}}(x) = |E_{\text{in}} + E_{\text{reflected}}(x)|^2. \tag{3.4}$$

The reflected electric field is thereby given by

$$E_{\text{reflected}} = E_{\text{in}}|R|e^{i\Phi_R}\frac{e^{i2k_x x}}{\sqrt{x}}, \tag{3.5}$$

where we take the geometrical decay into account via $1/\sqrt{x}$. Additionally the equation includes a phase that the polariton acquired after a distance of $2x$ (from the tip to the edge and back), and a complex coefficient $|R|e^{i\Phi_R}$, which contains information about the non-perfect coupling efficiency of the tip to the polariton and potential

losses (and phase shifts) due to the reflection at the edge. Inserting this electric field into equation 3.4, leads to a measured intensity signal

$$I_{\text{measured}}(x) = |E_{\text{in}}|^2 \cdot \left(1 + \frac{|R|^2}{x} + 2\frac{|R|}{\sqrt{x}}\cos(2 \cdot k_x x + \Phi_{\text{R}})\right). \tag{3.6}$$

The measured intensity contains two background terms and one term that oscillates with $2 \cdot k_x x$. We have removed the background from the measured data in Fig. 3.17a by subtracting a running average. As a result, we can fit the processed data using

$$I_4(x) \propto I_4^0 \cdot \frac{\cos(2 \cdot k_x x + \Phi_{\text{R}})}{\sqrt{x}}, \tag{3.7}$$

where I_4^0 takes the role of the initial incoupled intensity and the amplitude loss due to the reflection at the edge. Fitting the data of Fig. 3.17a at delay times $t_{\text{pp}} = 0\,\text{ps}$ and at $t_{\text{pp}} = 2.25\,\text{ps}$ shows that both modulations share a common in-plane wavevector, $k_x = 3.84\,\mu\text{m}^{-1}$, and also the phase shift of the reflection, $\Phi_{\text{R}} = -0.22$. The modulation amplitude I_4^0 varies and for the best fit is 0.2 and 0.14 for $t_{\text{pp}} = 0\,\text{ps}$ and at $t_{\text{pp}} = 2.25\,\text{ps}$, respectively.

The fit-curves for these examples are overlaid on the actual data as red lines in Fig. 3.17a. The good agreement between the theoretical curves and the experimental results highlights the low losses in the propagation since no imaginary part of k_x is needed to explain the amplitude decay from the edge. This means that over the measured distance of $\approx 4\,\mu\text{m}$ ($8\,\mu\text{m}$ propagation distance) the hybrid polariton mode exhibits negligible loss and the standing wave pattern solely decays due to geometrical spreading. This is another indicator of the long polariton lifetime, which was inferred from the linewidth of the ultrafast spectral response (Fig. 3.9) and discussed at the end of section 3.6.

Using the fit routine for all recorded delay times for which a sinusoidal modulation is seen allows one to extract the instantaneous wavelength of the hybrid polariton. The results are shown in Fig. 3.17c, where the polariton wavelength is plotted as a function of pump-probe delay. The red shaded area indicates the range of the measured wavelengths. The deviation is only $0.1\,\mu\text{m}$ across the whole time window where standing wave patterns can be measured. This finding underlines the

strong confinement of the hybrid mode in the k_x vector component. Additionally, it highlights the remarkable feature of the hybrid mode: In contrast to a bare surface plasmon polariton the wavevector does not change significantly as a function of pump-probe delay time. The averaged value of the wavelength on this particular flake was 1.67 µm, which is actually also quite close to the center wavelength of the pump laser ($\lambda_{\mathrm{Pump}} = 1560\,\mathrm{nm}$). However, this is a coincidence for this heterostructure and varies slightly for different flakes (see Fig. 3.5). Nevertheless, to exclude interference effects originating from the pump laser another study is conducted, where the same standing wave pattern is obtained for different pump laser wavelengths (appendix D).

An interesting point is that the observed polariton wavelength is much longer than typical surface plasmon polariton wavelengths seen on graphene, which lie in the hundred nanometer range. Additionally, the measured propagation lengths of $\approx 8\,\mu\mathrm{m}$ are atypical for surface plasmon waves at room temperature. Even in high quality samples of graphene encapsulated in boron nitride [Woe15] the propagation was only visible for 800 nm from the edge. The intriguing long propagation length of the hybrid mode can, however, be explained by considering that the mode is a coupled system composed of not only a surface plasmon polariton, but also a spectrally sharp surface phonon polariton. For bare phonon polaritons, long propagation lengths on the order of tens of micrometers have been reported in silicon carbide [Hub08].

The propagation distance for the phonon polaritons in the heterostructure can also be modeled theoretically using the dielectric function of silicon dioxide which was used in the dispersion calculations (for the exact details of the dielectric function see appendix C). The real and imaginary parts of the dielectric function in the relevant frequency range are depicted in Fig. 3.19a. The multiple Lorentzian phonon resonances in the Reststrahlen band given by reference [Gun00] are visible. These lead to an intricate dispersion diagram in the unexcited structure (see also Fig. 3.12 and Fig. 3.13a). From the dielectric function the in-plane wavevector k_x of a bare phonon polariton can be calculated using the analytical expression in equation 2.10 in section 2.1. From this complex valued quantity the wavelength of the mode can be determined using $\lambda = 2\pi/\mathrm{Re}(k_x)$, where $\mathrm{Re}(k_x)$ signifies the real part of the wavevector. Furthermore, the propagation length of the mode δ_{P}, defined by the

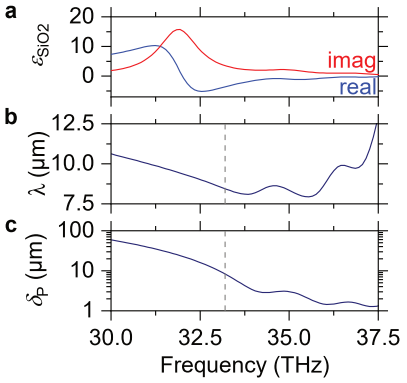

Figure 3.19. | Properties of surface phonon polariton propagation. a) The real (blue) and imaginary (red) part of the dielectric function determine the properties of a SiO_2 surface phonon polariton at an interface to air. **b)** The in-plane wavevector k_x determines the polariton wavelength λ, which is plotted as a function of frequency. **c)** From the imaginary part of k_x the intensity decay length δ_P is extracted. Gray dashed lines indicate a frequency of 33.2 THz in panels **b** and **c**.

$1/e$ decay of the intensity, is given by the imaginary part of k_x via $\delta_P = 1/[2 \cdot \mathrm{Im}(k_x)]$ [Nov06]. For the given dielectric function, the wavelength is plotted in Fig. 3.19b and the propagation length is plotted in Fig. 3.19c (as a function of frequency in each case). The wavelength ranges from 8 µm to 12.5 µm in the relevant spectral range of the experiment, with three local minima at 33.8 THz, 35.6 THz and 36.9 THz. The calculated phonon polariton wavelengths are consistent with experimental values in the literature, e.g. the 10.85 µm surface phonon polariton observed in silicon carbide in [Hub08].

The propagation length δ_P follows a similar trend, exhibiting three minima, but note that these are blueshifted compared to the minima in the wavelength curve in Fig. 3.19b. Instead, they roughly correspond to locations where the curvature in the wavelength after a minimum changes sign. At these points the propagation length is decreased to the few micrometer scale. For frequencies below 33.8 THz the propagation length increases monotonically with decreasing frequency up to propagation lengths of ≈ 60 µm at 30 THz. However, the oscillator strength of the polariton decreases significantly for frequencies away from the phonons.

From these calculations we learn that propagation lengths on the order of tens of micrometers are reasonable for surface phonon polaritons, in contrast to the shorter propagation lengths observed for mid-infrared surface plasmon polaritons. Yet, since the wavelengths of surface phonon polaritons are also calculated to be in the ten

micrometer range, the propagation length δ_P in units of wavelength is 5 - 6 λ. This is consistent with the experimental observations in this thesis that the wavelength of the hybrid mode in the heterostructure is $\approx 1.5\,\mu m$ and the observed propagation length is $\approx 8\,\mu m$.

There are differences between the observed heterostructure polaritons and the predictions for surface phonon polaritons too, though. Specifically, the precise values of the observed wavelength and propagation length differ from those calculated for a bare surface phonon polariton. At a frequency of 33.8 THz, where the strongest photo-induced change was measured in the time-resolved measurements of the hybrid mode (Fig. 3.9), the predicted wavelength is roughly 8 µm and the propagation distance is approximately 3.8 µm. The value of the propagation distance, however, rapidly increases with decreasing frequency and already at 33.2 THz a propagation length of 8 µm is seen (gray dashed lines in Fig. 3.19b and c). The reason is that the surface phonon starts to curve off the light line at 32 THz and reaches its maximum curvature at 33.8 THz. This can be seen easily by calculating the dispersion for the bare surface phonon polariton at an interface of air and the silicon dioxide. The results are shown in Fig. 3.20a, where the dispersion is visualized via the Fresnel reflection coefficient r_p as a function of frequency and k_x. At the upper frequency limit of the polariton the damping is also the highest (see imaginary part of k_x in Fig. 2.4c) leading to a strong suppression of the mode propagation. The hybrid mode in the case of the black phosphorus heterostructure therefore profits strongly from the fact that the intersection point of the surface plasmon and the split phonon polariton lies at slightly lower energies than the bare surface phonon polariton. What is particularly helpful in this case is the fact that the polariton is split in the thin silicon dioxide film of the capping layer, as this leads to a further decrease of the frequency of the intersection point. The dispersion of a thin slab of silicon dioxide surrounded by air is shown in Fig. 3.20b to demonstrate the shift for the thin capping layer compared to the bulk case. The redshift is also nicely visible in the experiment in Fig. 3.16a, where on the silicon dioxide the strong surface phonon is visible at 33.8 THz and on the heterostructure the hybrid mode lies at a slightly lower frequency of ≈ 33.2 THz (corresponding to a propagation length of 8 µm in Fig. 3.19).

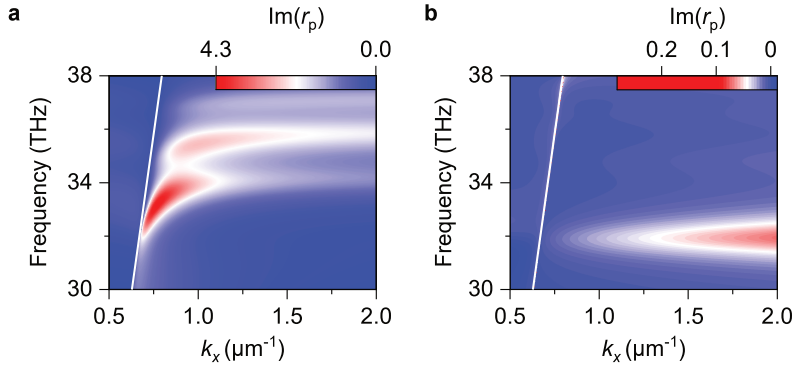

Figure 3.20. | Dispersion of surface phonon polaritons in silicon dioxide including thin-film effects. In contrast to calculations of the full heterostructure, this figure considers only bare silicon dioxide surface phonon polaritons. **a)** The imaginary part of r_p for an interface of air and silicon dioxide is plotted as a function of in-plane wavevector k_x and frequency. The silicon dioxide dielectric function is modeled according to the calculations in the previous sections. **b)** The dispersion of polaritonic modes of a thin film (5 nm) of silicon dioxide in air is modeled to show the effect of the thin-film splitting in the thin capping layer on the heterostructures.

In the measurements of the spectral response as a function of delay time in Fig. 3.9 the frequency with the highest pump-induced change is slightly higher than what is observed in the hyperspectral map (Fig. 3.16a). Here, the distinction between pump-induced change and absolute spectral amplitude has to be made: The strongest modification in time, which is seen in the pump-induced spectral change (Fig. 3.9), can likely appear at a frequency not coinciding perfectly with the hybrid mode but rather its high-frequency border. Such an observation is expected for the hybrid mode, since the spectral components of the hybrid mode surpass the contributions of the split phonon mode, which dominates the equilibrium response (Fig. 3.8c). The relative change is therefore strongest for components at the high-frequency end of the hybrid mode, as these show a comparably low scattering response in equilibrium (see Fig. 3.8c). Quantitatively, the drop in the spectral amplitude close to the silicon dioxide resonance in equilibrium appears between 33 THz and 34.5 THz (maximum

to minimum value), which is also the range where the strongest modulation in the pump-induced spectral change is seen (Fig. 3.9). Comparing these numbers to the resonances in silicon dioxide also shows that the hybrid mode enhances frequencies that are associated with the unsplit phonon resonance, as seen in Fig. 3.8b.

This is in agreement with the central conclusion of this section, which is that the long propagation lengths of the hybrid mode indicate that it has a strong phononic character. The pump pulses induce a coupling of the two different silicon dioxide layers via the transient plasmonic mode and thereby increase the phononic parts of the spectrum as the thin top surface is linked to the thick bottom SiO_2 surface (which by itself shows a spectrally narrow phonon resonance). A more detailed explanation can be found in the discussion of Fig. 3.12. This interplay makes the mode switchable and yet provides it with a long propagation. Additionally, the coupling to the surface plasmon mode leads to the strong confinement of k_x-vectors and frequency of the hybrid mode, which made the recording of snapshots in real space with a broadband source possible (see Fig. 3.6).

An alternative but complementary way to understand the long propagation of the hybrid polariton mode is in terms of the inverse of the damping, the so-called polariton lifetime. The experiments suggest a lifetime of approximately 177 fs (see equation 3.2). In the next section the implications of this increased polariton lifetime, compared to the plasmon polariton, are discussed in more detail. In the discussion, the polariton lifetime will also be distinguished from the carrier lifetime of the free electrons in the structure, which is a crucial point when dealing with ultrafast switching of polaritons.

3.8. Implications of carrier and polariton lifetimes

A subtle but very important point when dealing with ultrafast switching of surface polariton modes is the differentiation between the different timescales involved in the process. The most important ones are the polariton lifetime and the carrier lifetime. Steady-state near-field measurements, which are common practice in the field, only measure the polariton lifetime because the carrier density in equilibrium does not change.

Generally, the carrier lifetime in a semiconductor denotes the timespan over which free carriers populate the conduction band following an interband excitation, before they recombine. It is the timescale in which plasmon polariton propagation is allowed in the heterostructures. Just as the experiment has shown, a polariton can only be launched when free carriers exist in the structure. This is the key concept to high-contrast ultrafast switching. The polariton lifetime on the other hand is given by the quality (q-factor) of the polariton mode and determines the propagation length and decay characteristics of each individual polariton wave.

So far, there is only one preceding work on near-field studies of photo-excited polaritons [Ni16] where the carrier lifetime also plays a role. However, this new field of research has already produced interesting theoretical work. Spectacularly, it has been predicted that photo-activation of plasmons could even lead to plasmon amplification [Sun16]. Z. Sun, D. N. Basov and M. M. Fogler have shown theoretically that the evolution of a polariton's dispersion – governed e.g. by the carrier lifetime – leads to an additional timescale, and that this timescale can have an interesting interplay with the polariton lifetime. I will briefly rephrase the main points of this finding.

The oscillation of charges of the polariton can be described as a harmonic oscillator with a damping γ and an oscillation angular frequency ω given by its energy. Both of these quantities can be time dependent, leading to a differential equation for the charge density X as a function of time

$$\left[\partial_t^2 + \gamma(t)\partial_t + \omega^2(t)\right] X(t) = 0. \tag{3.8}$$

For a slowly decreasing oscillation angular frequency $\omega(t) \propto e^{-\kappa \cdot t}$, caused for example by carrier recombination and the accompanying decay of the plasma frequency with a decay rate $\kappa \ll \omega$, Z. Sun *et al.* show that the amplitude of the charge density oscillation for a constant damping rate γ is given by

$$A(t) = e^{(\kappa-\gamma)t/2}. \tag{3.9}$$

Depending on the relation between the decrease in frequency κ and the damping γ, the amplitude can decrease, or, surprisingly, increase, corresponding to amplifi-

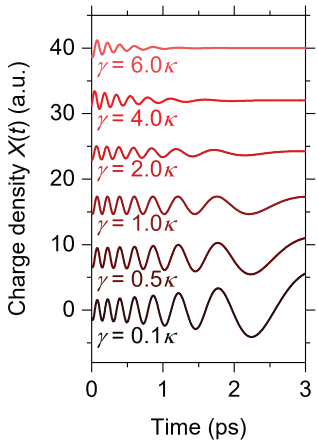

Figure 3.21. | Plasmon amplification. Shown is the oscillation of the charge density $X(t)$ of a plasmon over time modeled by a harmonic oscillator with a time dependent angular resonance frequency $\omega(t) = 50\,\mathrm{THz} \cdot e^{-\kappa \cdot t}$. For the simulations the frequency decay was chosen to be constant at $\kappa = 1\,\mathrm{ps}$ and γ was varied to show the effects of γ smaller than, equal to and larger than κ.

cation. In Fig. 3.21 the numerical solutions of the differential equation are shown for different ratios between κ and γ. The method to solve the differential equation numerically is described in appendix E.

The oscillation period increases for all curves over time due to the decay of the instantaneous resonance frequency. Depending on the ratio of γ to κ the amplitude also changes according to equation 3.9. For $\gamma = \kappa$ it stays constant, whereas for larger damping the amplitude decays exponentially. For smaller damping rate than decay rate, the oscillation magnitude actually increases, leading to an amplification of the polariton.

The results are quite astounding, as they show that the amplitude of a polariton can be increased by precisely tuning the relative strengths of the damping rate and mode evolution rate, providing the prospective for very long polariton propagation distances. The role this plays in the case of the hybrid polariton mode, i.e. whether amplification contributes to the very long observed propagation length, is therefore extremely interesting. To model the effect, we have to find reasonable assumptions for the time dependent frequency shift of the hybrid polariton and (for comparison) also the plasmon polariton together with realistic values of the damping γ of both

modes. To do so, we will have a closer look at the experimental results that we have discussed so far.

We have estimated the polariton lifetime of the hybrid mode to be approximately 177 fs (see equation 3.2) to explain the long propagation distances measured on the flakes. For the carrier recombination rate, the estimate is more difficult. The pump-probe experiment in Fig. 3.3 shows the decay of carriers but it includes the nonlinear response function of the near-field signals as discussed previously [Eis14, Sti10]. The time after which the pump induced change has decayed back to half its maximum value is at 2.4 ps and the $1/e$ value is reached at 3.4 ps. The intensity reaches the baseline after 5 ps (when the plasma frequency leaves the Reststrahlen band) but remains low until 20 ps after excitation.

A more direct way to access the carrier lifetime is to look at the evolution of the scattered amplitude spectrum, as was done previously for indium arsenide nanowires and bulk surfaces [Eis14, Wag14b]. In the present case the situation is more complex, though, since the sample response is not given by a simple Drude model. Nevertheless, the frequency at which there is zero change to the scattered amplitude spectrum (ν_{0C}, see section 3.4) can be used as a marker of the high-frequency edge of the upper surface plasmon polariton branch. Therefore, tracing the point ν_{0C} as a function of delay time can reveal the evolution of key aspects of the polariton dispersion, in analogy to direct measurements of the plasma resonance frequency in the simpler case of indium arsenide. The extracted ν_{0C} values for the ultrafast spectral evolution of the heterostructure (full spectra in Fig. 3.9) are shown in Fig. 3.22 as red spheres. The error bars are given by the frequency resolution of the measurement. One can clearly see the initial rise (blueshift) from 0 to 0.25 ps and the subsequent redshift for increasing delay times. The time-dependent redshift, which corresponds to a decreasing of the plasma frequency due to carrier recombination, can be fit by an exponential decay (red curve in Fig. 3.22). The curve is given by

$$\nu_{0C}(t_{pp}) = (3.0 \pm 0.6)\,\mathrm{THz} \cdot e^{-\frac{t_{pp}}{(2.7\pm1.2)\,\mathrm{ps}}} + (33.4 \pm 0.7)\,\mathrm{THz} \tag{3.10}$$

from which two things can be seen. Firstly, the exponential decay suggests a decay rate on the order of $1/(2.7\,\mathrm{ps})$. Secondly, the modulation is less than 10% of

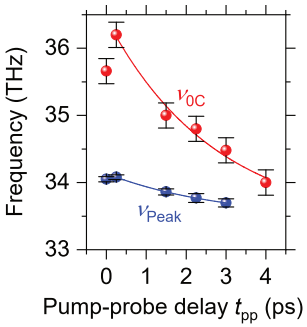

Figure 3.22. | Ultrafast evolution of frequency shifts in the hybrid mode. The location of zero change ν_{0C} (red) and the position of the maximum change ν_{Peak} (blue) of Fig. 3.9 are plotted as function of pump-probe delay time. Excluding the first value of the rise, exponential decay curves with an offset from zero are fitted to the data (lines).

the additional baseline of 33.4 THz, which has to be added. These observations are consistent with the theoretical prediction that the change in plasma frequency can result in a small change in the extension of the hybrid mode's confinement in frequency (Fig. 3.13). The offset is owed to the strong surface phonon polariton mode, which prevents ν_{0C} from passing below the frequency of the phonon resonance (33.8 THz on bare SiO_2 and $\approx$ 33 THz on the heterostructure due to thin-film splitting). Therefore, the decay time of 2.7 ps can also only be seen as an estimate of the plasmonic decay, which, however, is in good agreement with the values for the point of half-decay and the $1/e$ point in the pump-probe measurement (Fig. 3.3).

Dissecting the spectra into traceable points of interest also allows one to learn a little more about the evolution of the hybrid mode. By fitting the pump-induced changes to the spectra (Fig. 3.9) with Lorentzians in the region of 33 to 36 THz, the peak position can be determined more precisely as a function of pump-probe delay time than by only extracting the frequency with the maximum value in the amplitude. The evolution of the peak frequency ν_{Peak} as a function of pump-probe delay time is also plotted in Fig. 3.22 (blue spheres). The error bars correspond to the uncertainty in the Lorentzian fits. Analogous to the dynamics in ν_{0C}, an initial blueshift and subsequent redshift is seen. The redshift can be fitted with an exponential decay (blue line), which is given by

$$\nu_{Peak}(t_{pp}) = (0.68 \pm 0.01)\,\text{THz} \cdot e^{-\frac{t_{pp}}{(2.89\pm0.08)\,\text{ps}}} + (33.45 \pm 0.01)\,\text{THz}. \tag{3.11}$$

The fit corroborates the claim of a hybrid mode that stays almost constant in frequency, with only very small shifts ($< 3\%$ of the center frequency). Comparing it to the fit of ν_{0C}, the time constant is comparable for ν_{Peak} and the amplitude of the decay is 23% of the one for ν_{0C}. Nevertheless, this extraction highlights an interesting point in ultrafast polariton control, as it shows that the mode does evolve in time while it is in existence.

To estimate how the amplitude and wavelength of the hybrid mode evolve during propagation according to the model of Sun *et al.*, we can now use these extracted changes in the instantaneous frequency from Fig. 3.22. The change to the peak position $\nu_{Peak}(t_{pp})$ serves as a good estimate for the instantaneous frequency of the hybrid mode, whereas $\nu_{0C}(t_{pp})$ can be used as a rough guide to follow the evolution of the pure plasmonic response. In fact $\nu_{0C}(t_{pp})$ does not correspond to the raw black phosphorus plasma frequency because of the strong SiO_2 phonon contribution (see discussion of equation 3.10) but it still allows for the time-dependent mode wavelength to be determined when an appropriate scattering rate γ is assumed. In the simulations of the dispersion of the hybrid mode, the scattering rate of the plasmon has been set to 13.5 THz. This has resulted in a well defined hybrid mode and has led to good agreement between the theory and the measured data. The value is obtained from literature values for averaged in-plane effective masses and mobilities (see appendix C). For the hybrid mode, the scattering rate can be approximated from the FWHM linewidth of the spectral response of the hybrid mode and resulted in a scattering rate $\gamma_{est} \approx 1/(177\,\text{fs})$ (see end of section 3.6 and Fig. 3.9). This value corresponds to the lower boundary for the scattering rate, since the mode potentially extends further in frequency than the peak in the pump-induced spectral response (see discussion in section 3.7 following the description of Fig. 3.20).

The results of the numerical simulations are depicted in Fig. 3.23, where the hybrid mode's charge oscillations in time are plotted in blue and the oscillations of the pure plasmonic mode are shown as a red line. To simplify a direct comparison, the curve of the hybrid mode is shifted by 5.9 fs in time, such that the first zero-crossing happens at the same time for both curves. The amplitudes are normalized to the first maximum of each curve.

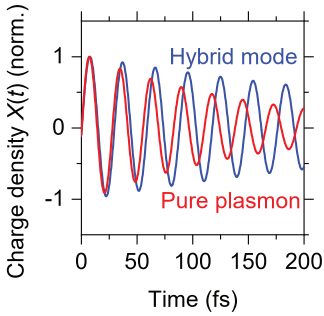

Figure 3.23. | Propagation of the hybrid mode and the pure plasmon polariton in time. Plotted are the numerical solutions to differential equation 3.8 for the propagation of the hybrid mode and a pure plasmon polariton. The values for the instantaneous frequency and the damping rate are discussed in the text. The decays are governed by the damping and no amplification of the modes is seen.

There is a discernible decay of the oscillation amplitude for both polaritons, i.e. no polariton amplification. However, over the period of the hybrid polariton lifetime, which was estimated to be 177 fs, the loss in amplitude is not as strong as has been seen for the line scans in Fig. 3.17a. The simulations do not include the $1/\sqrt{x}$ decay due to the geometrical spreading of the wave, such that the polariton decays only due to the intrinsic damping of the mode (corresponding to the chosen scattering rate). These results agree with our previous findings that the hybrid polariton shows low damping over the distance where it can be measured and is mostly dominated by the geometrical decay. The plasmon shows a stronger damping, which is in agreement with a lifetime of ≈ 74 fs (see also appendix C).

Additionally, for the hybrid mode one can nicely see that the modulation wavelength does not significantly change over time. This is in agreement with the measured data where also no prominent change to the spacing of the maxima has been seen for increasing distance from the edge (compare e.g. Fig. 3.6 and Fig. 3.17a). The reason for this behavior is that the influence of the frequency pinning by the phonon polariton interaction outweighs the influence of the slight shift produced by the change in the plasma frequency.

In contrast, the bare plasmon polariton mode shows a prominent change in the instantaneous wavelength over time. This effect, together with the stronger damping, complicate the detection of the bare plasmon polariton when measuring the spectral response at a single position on the heterostructures. Nevertheless, it is possible to

measure the pure plasmon polariton at frequencies below the Reststrahlen band of silicon dioxide, where it is not hybridized with the phonon polaritons. The evolution of this bare SPP^+ mode is investigated in the next section.

3.9. Tracing the pure surface plasmon branch at low frequencies

Based on the theoretical model detailed in this thesis, the hybrid polariton mode is composed of the phonon contributions in the Reststrahlen band of SiO_2 and the upper branch of a thin-film-split surface plasmon polariton in black phosphorus. The calculated dispersion diagrams (Fig. 3.12b and Fig. 3.13) show that the split surface plasmon polariton also exists at lower energies than the hybrid mode. For these frequencies it is not coupled to the surface phonon polaritons and exists as a bare surface plasmon polariton with strong dispersion.

It should be possible to trace this part of the mode experimentally by investigating the heterostructure using probe pulses with a lower center frequency. In the experimental setup, the probe pulses are generated via difference frequency generation in a gallium selenide crystal. The rotation angle of the crystal relative to the incident beams allows one to tune the phase matching condition, resulting in a shift of the center frequency of the probe pulses. To find the fingerprint of the bare surface plasmon mode, the probe spectral bandwidth is shifted to the range of 28 THz to 34 THz and another time dependent spectral analysis is performed (analogous to the data in Fig. 3.9 but at lower frequencies).

The amplitude spectra of the experiment for different delay times are shown in Fig. 3.24. Again, the data are normalized to a spectrum at negative delay times to visualize solely the pump-induced change. For comparison with the previous, higher frequency measurements, a selection of complementary amplitude spectra from Fig. 3.9 are plotted in the right panel of Fig. 3.24. For consistency, the low frequency measurements are performed on a heterostructure with roughly the same height ($\approx$ 110 nm) as the flake of the first dataset. It is visible that the spectral

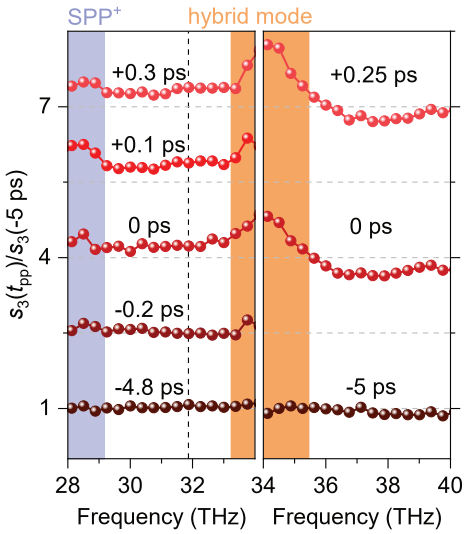

Figure 3.24. | Ultrafast spectral response of the unhybridized plasmon polariton. Plotted is the combined spectral evolution of the hybrid mode (orange shading) and at lower frequencies the (upper) bare surface plasmon mode SPP^+ (light blue shading) for different pump-probe delay times. The data in the right panel are selected curves taken from Fig. 3.9. The dashed black line shows the low frequency end of the SiO_2 Reststrahlen band. The data are vertically offset for clarity.

features of the two different measurements show striking agreement in the region around 34 THz for comparable delay times. Already at a delay time of $t_{pp} = -0.2$ ps the spectral amplitude increases in this area (indicated by an orange shading). The amplitude subsequently rises for increasing delay times. The good agreement between the data shows the reproducibility of the experiment for heterostructures of comparable height. It has been seen that the exact frequency of the hybrid mode depends weakly on the thickness. This dependency can be attributed to different thin-film splitting of the surface plasmon, which modifies the crossing point of the hybrid mode as well as a change in the photo-induced carrier density.

The most interesting part of the graph for our current discussion is the low frequency region. At the same time as the hybrid mode emerges a shoulder appears in the spectrum for frequencies $\nu \lesssim 29$ THz (blue shaded area). This peak can be attributed to the upper branch of the split surface plasmon polariton (SPP^+), which enters the spectrum from the low frequency side for increasing carrier density. At $t_{pp} = -0.2$ ps the two maxima in the amplitude (SPP^+ and the enhancement around 34 THz) are separated by a spectral region without any pump-induced change. Referring back to

the theory calculations in Fig. 3.13, this behavior is consistent with the prediction that initially, with increasing plasma frequency upon photo-excitation, the plasmon polariton screens the high frequency phonons and enhances the oscillator strength of the low frequency phonon polariton branch LO^- (see Fig. 3.13b). At this time the spectral feature around 34 THz is not yet the hybrid mode, but instead only the enhanced surface phonon polariton LO^-. The two modes are still separated in the dispersion diagram. Nevertheless, the SPP^+ influences the split phonon polariton by changing the dielectric environment at the interface to the adjacent SiO_2. This observation agrees with Fig. 3.7a, where the fringes associated with the hybrid mode are only visible closer to (i.e. within 50 fs of) pump-probe time overlap. Additionally, this finding is also consistent with Fig. 3.14, which shows the complementary measurements of fringe spacing versus pump fluence (rather than time delay). At low fluences, before the hybrid mode is observed as a standing wave pattern, another short-wavelength feature is discernible (white dashed lines in Fig. 3.14b). This could be an indication of the strengthening of the LO^- surface phonon branch by the surface plasmon polariton SPP^+, before it enters the Reststrahlen band. At later times, e.g. $0\,\mathrm{ps} \leq t_{\mathrm{pp}} \leq 0.1\,\mathrm{ps}$, the scattered amplitude in the center of the spectrum in Fig. 3.24 increases above the baseline to a positive value, while the maxima at the edges of the spectrum both also increase. Having passed the point of maximum pump-probe signal, the amplitude of the surface plasmon polariton branch decays at $t_{\mathrm{pp}} = 0.3\,\mathrm{ps}$.

The magnitude of the pump-induced change to the scattered amplitude between 29.2 and 33.2 THz, i.e. in the region between the bare surface plasmon mode and the hybrid mode, always remains lower than either of the individual photo-induced resonances. This behavior is consistent with theory. The calculations show a suppression of the SPP^+ branch at the lower boundary of the Reststrahlen band, which leads to a clear separation of the hybrid mode and the bare SPP^+. This effect leads to the well defined confinement of the hybrid mode in energy and momentum. In the experiment the avoided area is roughly 5 THz wide from peak to peak of the modes. This value is larger than expected from the theory plots. However, one has to consider that the extension of the hybrid mode in frequency is potentially larger than the bare peak in the pump induced change due to the shape of spectrum

in equilibrium (see also the discussion in section 3.7 following the description of Fig. 3.20). The hyperspectral map (Fig. 3.16) showed that the mode extends down to almost 32 THz in good agreement with the theoretical calculations. Therefore, the avoided crossing region is more likely only $\approx$ 3 THz wide in the experiment, which is in reasonable agreement with the theoretical predictions.

Another difference between theory and experiment is that the strength of the scattered amplitude of the hybrid mode surpasses that of the bare SPP^+ surface plasmon polariton. However, this effect can be explained by considering the damping mechanisms in the structure. It has been discussed in the previous section that the quality factor of the hybrid mode is higher than the one of the surface plasmon polariton due to the coupling to the sharp phonon resonance. This leads, together with the high phase velocity, to long propagation. Bare surface plasmon polaritons, on the other hand, typically propagate shorter distances at room temperature [Che12, Fei12, Woe15].

To measure the spectra in Fig. 3.24, the tip was located on the first bright fringe next to the edge of a photo-excited heterostructure. For all spectra this position was not changed. These are optimal conditions to probe the hybrid mode for which the interference pattern does not change significantly as a function of pump-probe delay time (see Fig. 3.17). The surface plasmon polariton on the other hand should change its wavelength significantly (compare Fig. 3.13) making the detection scheme less appropriate. For this reason a lower scattered near-field amplitude can be understood as being due to the fact that the tip position might not be well suited for measuring the surface plasmon polariton SPP^+ at each time. In other words, the interference is not always fully constructive for the SPP^+ branch.

Nevertheless, we have seen that the low frequency plasmon branch (SPP^+) predicted by theory can be traced in the experiment. It showed a strong dispersion, which made it difficult to trace in the spectral analysis because of the changing wavelength and stronger decay compared to the hybrid mode. In contrast, the constant wavevector and fixed energy of the hybrid mode are very favorable traits for the implementation in polaritonic devices. Therefore, the next chapter addresses these advantages for device integration and also expands on other materials, which could complement this novel polariton-based logic.

Chapter 4

Device integration and prospective future directions

In the previous chapter, we have seen that heterostructures of black phosphorus and silicon dioxide can serve as a technological platform for ultrafast switchable polariton devices. The benefits of such devices include faster computational speed and potentially less heat dissipation. In combination with other two-dimensional materials a polaritonic circuit can be envisioned. The advantages of the hybrid mode composed of surface plasmon and surface phonon polaritons are its strong confinement in energy and momentum. Due to these well defined properties, custom-tailored heterostructures can in the future be utilized with a monochromatic laser to launch surface polaritons with a single grating, since the region of confinement does not strongly vary as a function of pump-probe delay time for the photo-activated structure. The grating thereby replaces the tip to provide the single necessary wavevector to couple to the mode. This constitutes a great advantage for fabrication, as it is easier to implement than coupling mechanisms with multiple lasers or different gratings (for which it would be necessary to match the wavevector of a transient mode with momentum changing on the picosecond timescale). The exact position of the hybrid mode in momentum and frequency can also be custom tailored by varying the thickness of the different silicon dioxide layers and the black phosphorus flakes, which determines the splitting of the thin-film polaritons.

Coupling these switchable nanophotonic devices to other thin-film polariton structures can lead to new interesting physics, which may allow for further consolidation of polaritons for future electron-light-coupled logical devices. Already at the lateral interface of bilayer and single layer graphene, intrinsic effects like a plasmonic analogue of Snell's law have been found [AG14]. In that work focusing of surface plasmon polaritons has also been shown. Similar observations have been reported for surface phonon polaritons [Hub08]. Additionally, defects and topological boundaries can be used as local reflection channels for guiding surface polaritons [Jia17].

Furthermore, the focus of the polariton community is shifting from a very plasmonics-based approach towards phonon polaritons, as they offer high quality factors and hence long propagation distances. In this respect, hexagonal boron nitride has been of great interest, as it features a strong anisotropy of the in- and out-of-plane dielectric function and exhibits hyperbolic phonon polaritons [Dai15, Yox15]. Even the very common substrate silicon dioxide, which was used in this thesis, is under intense investigation for future polariton devices.

An especially intriguing experiment has been reported recently where SiO_2 was combined with an ultra-thin film of the phase-change material $Ge_3Sb_2Te_6$ [Li16]. In this configuration, it has been possible to perform non-volatile optical switching of the phase-change material, which led to a local dielectric contrast where the material properties were altered. At the edges of the written structure the authors could measure ultra-confined surface phonon polaritons with near-field microscopy. This is an important step towards future storage devices. The persistent storage of information in a polariton structure is the second prerequisite for future data manipulation, following ultrafast plasmon logic (which could be based on switchable interface polaritons in black phosphorus heterostructures).

One of the prototypical phase-change materials is vanadium dioxide (VO_2), which features a transition from insulating states to a metallic state at a temperature of 341 K, i.e. close to room temperature [Mor59]. Of special interest in this material has been its ultrafast photo-activation and the non-trivial correlation of the phase transition with strain. Therefore, vanadium dioxide nanobeams are studied in the following section using ultrafast near-field nanoscopy. Hereby, particular focus is

set onto the possibility to strain-tailor the transition-temperature and the ultrafast response at room temperature for future devices.

As a final outlook towards new materials for ultrafast switching of polaritons with low damping, the subsequent section addresses the promising role of topological insulators in the field of polaritonics. Here, first results on the dielectric heterogeneity of $(Bi_{5\%}Sb_{95\%})_2Te_3$, a typical three-dimensional topological insulator, are revealed on the nanoscale.

4.1. Persistent switching for data storage in phase change materials

Vanadium dioxide changes from an insulator at room temperature to a metal for temperatures above 341 K. This close-to-room temperature transition made VO_2 the prototypical material for studying phase transitions and strongly correlated electron systems. The material features two insulating monoclinic phases, an insulating triclinic phase and a rutile metallic phase, which together give rise to an intricate strain diagram [Atk12b, Par13]. Recent reports even discuss an additional monoclinic metallic phase, which can be accessed by photo-excitation [Coc12, Nag12, Mor14]. The phenomenon that the phase transition can also be switched on ultrafast timescales with laser excitation has been reported earlier [Cav04, Küb07, Hil07] and is one of the reasons for the attractiveness of the material, as it can be switched rapidly, but also contains a persistent structural change for data storage. There are long-standing discussions about the origin of the transition, namely whether it is a Mott insulator [Zyl75], a Peierls insulator [Goo71], or some combination of the two. To accurately predict the bandgap in calculations, both effects have to be taken into account [Bie05]. Furthermore, the change in the ultrafast transition is accompanied by coherent oscillations [Cav04, Kim06, Küb07] in the polarizibility originating from structural oscillations of the vanadium-vanadium dimers. Spectrally disentangling these low frequency contributions (at $\approx 6\,\mathrm{THz}$) from the higher frequency response showed that the low frequency parts ($< 20.6\,\mathrm{THz}$) are dominated by excited phonons whereas the region of our probe spectrum would probe the free electron response of the system [Küb07].

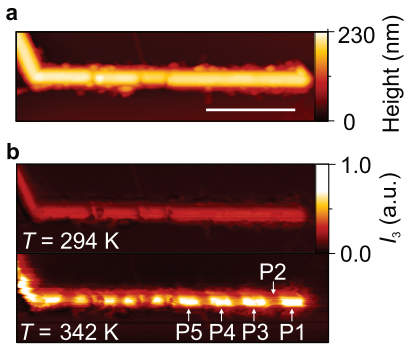

Figure 4.1. | Overview of the studied VO_2 nanobeam.
a) Height profile of an individual VO_2 nanobeam. The scale bar is 2 µm long. **b)** Recorded scattered near-field intensity as a function of position below (294 K, top image) and above (342±1 K, bottom image) the transition temperature. Points P1, P3 - P5 mark the centers of metallic domains and P2 one domain which did not switch. A continuous wave quantum cascade laser at a wavelength of 8.4 µm is used as the probe beam.

Since the phase transition is of first order, it features a nucleation and growth process of metallic domains upon switching. To observe the growth of the metallic puddles, near-field microscopy has proven to be ideally suited [Qaz07, Liu13, Liu15] as it features the necessary spatial resolution to probe the local change in the conductivity of the material on the nanoscale. Using near-field microscopy, it has been observed that strain leads to a stripe pattern of metallic and non-metallic domains in the material [Jon10, Liu14]. More specifically, the stripe pattern appears in single crystals under tensile strain. However, it has not yet been clear whether this is a predetermined pattern that is built into the investigated structure or a dynamic effect that appears upon heating. So far, the latter effect has been seen as highly likely because a dynamical change from one phase into the other allows the structure to minimize the strain in the material due to the different crystal lattice constants of the insulating and metallic phases. In the following, we probe the ultrafast response of a strained vanadium dioxide nanobeam on a sapphire substrate on the length scale of its phase heterogeneity to show that there is in fact a built-in substructure in the nanobeam already at room-temperature. The results obtained at room temperature are subsequently correlated with the periodic domain structure of alternating insulating and metallic sections that emerges above the phase transition temperature.

The topography of a single wire is shown in Fig. 4.1a. The nanobeams orient themselves along the high symmetry axes of the sapphire substrate and therefore sometimes show kinks as seen on the left edge of the nanowire. The nanowire growth happens at high temperatures (where it grows along the crystallographic *c*-axis) and due to a mismatch in the thermal expansion coefficients of sapphire and VO_2 the wire is under tensile strain at room temperature. Furthermore, there are multiple small sized particles and grain boundaries along the main wire. However, on the right side, there is a 3-µm-long single crystalline part, which shows a clean surface. This region is the center of attention in the following study of its response upon photoexcitation. In the first step, the scattered near-field intensity is recorded below and above the phase transition temperature of VO_2. At room temperature no distinct features are visible in the scattered near-field intensity off the structure apart from the grain boundaries, which exhibit a lower scattering intensity than the rest of the nanobeam (Fig. 4.1b, top). In contrast, above the transition temperature (Fig. 4.1b, bottom) the single crystalline part of the nanowire shows a dominant fringe pattern, which corresponds to metallic (bright) and insulating (dark) domains. The locations of these domains do not vary even after multiple cycles of the structure from low to high temperatures and are independent of whether the thermal load on the wire is provided by a heater stage or by the average power of ultrafast near-infrared pulses supplied at a high repetition rate. It has to be noted that the structure has never been heated to such high temperatures that the full beam would have switched to the metallic phase.

Thus, having a sample with the intriguing pattern of insulating and metallic domains in the case of elevated temperatures, the possibility to disturb the local conductivity at room temperature is investigated. Pump-probe measurements with the frequency doubled pump laser (center wavelength 780 nm, pump fluence 2.1 mJ/cm^2) are performed on the different domains, which cannot be distinguished in the scattered near-field signal at room temperature (Fig. 4.1b, top). A characteristic pump-probe trace is shown in Fig. 4.2a. On all investigated positions, a very sharp rise and a decay back to the baseline within 1 ps is seen. Interestingly, the peak height varies between locations that turned metallic and regions that stayed insulating at elevated temperatures. To fully trace this behavior, the time delay is set to the peak of the

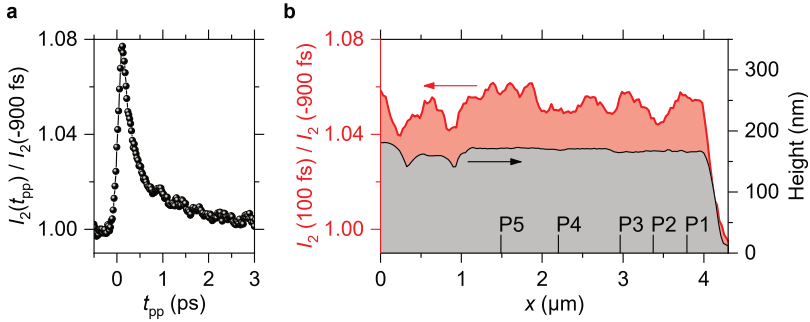

Figure 4.2. | Pump-induced change. a) Near-field pump-probe intensity scan at room-temperature taken at position P1 of Fig. 4.1b. The sample was photo-excited with the frequency doubled pump laser with a center wavelength of 780 nm and a pump fluence of 2.1 mJ/cm^2. **b)** A line scan across the center of the wire is performed while the sample is photo-excited. The height profile of the scan is plotted (black line) and is approximately flat over the whole single crystalline part of the wire. The simultaneously recorded scattered near-field radiation of the probe pulses (center frequency: 31.5 THz with a bandwidth of 10 THz FWHM and a duration of 60 fs FWHM) shows a strong modulation along the wire (red line). The delay between pump and probe was set to 100 fs, which is the peak in a pump-probe scan. The central positions of the bright domains in Fig. 4.1b are marked with P1, P3, P4 and P5. P2 is the central point between the first two metallic regions, which did not switch.

pump-probe trace and the SNOM tip is scanned across the single crystalline region of the wire. The recorded scattered intensity as well as the simultaneously recorded topography are shown in Fig. 4.2b. The height scan clearly shows the edges of the single crystalline region: To the right side it is the end of the wire and on the left side the grain boundary at $x \approx 0.9\,\mu$m, which is seen as a sharp trench in the topography. Between these borders, the height profile is very homogeneous and shows no topographic irregularities that could influence the pump-probe scan. The scattered intensity normalized to the near-field signal at negative time delay, however, shows a striking modulation across the one-dimensional scan range. Most notably, near the end of the wire the intensity shows an oscillatory modulation, which is high on the locations where the wire turned metallic at elevated temperatures (marked

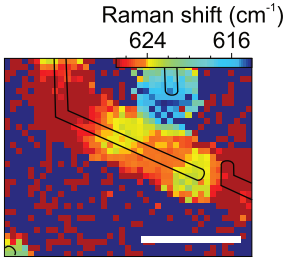

Figure 4.3. | Raman measurement to probe strain effects. Color-coded is the peak position of the triclinic ω_O phonon mode in a spatially resolved Raman measurement with a spatial resolution of $\approx$ 1 µm. The measurement was performed at room temperature with a probe fluence of $\approx$ 1 mW. The scale bar is 4 µm long and the black lines outline the nanowire position.

with P1 and P3) and low on the persistently insulating domain in-between (P2). Apart from these two maxima there are two more maxima which agree with the existence of two more metallic domains. At the left side, there is a region of high pump-induced change featuring three maxima, which are located around the position of the metallic domain P5. The metallic domain P4 does not perfectly match a peak in the scattered intensity. Nevertheless, these results show that there is an approximate correlation between the insulator-to-metal switching susceptibility and the room-temperature peak height of the pump-probe curves for the nanobeam for below-threshold photo-excitation.

Presumably, the microscopic origin of the interplay between the local change to the conductivity and the switching susceptibility is mediated by strain inside the structure. This assumption can be corroborated by a micro-Raman spectroscopy map of the nanowire, which is shown in Fig. 4.3. In the false-color plot, the peak shift of a strong Raman active mode is shown, which shifts depending on the strain in the material [Jon10]. Representative Raman spectra of the nanobeam together with details on the Raman setup are given in appendix F. The spatial resolution of this far-field technique is limited to approximately 1 µm, but one can already see local changes to the mode at the edges of the single crystalline domain. Also, the influence of strain is consistent with literature observations, which state that tensile strain increases the transition temperature [Atk12b, Par13] and blueshifts the bandgap [Abr12]. Therefore, domains with increased tensile strain are less likely to turn metallic and show a larger bandgap, which results in a lower population of the semiconducting conduction band upon photo-excitation with fluence below the transition threshold. Having fewer free carriers corresponds to a lower scattering intensity, which is mea-

sured in the pump-probe scans. These findings make strain tailoring of vanadium dioxide quite promising for local control of the ultrafast optical response and also the switching susceptibility. Furthermore, pump-probe nanoscopy can be used as a tool to determine strain in vanadium dioxide structures with nanoscale spatial resolution. In the investigated sample system the strain pattern is already frozen into the structure and most likely originates from the cooling process after the growth of the nanobeams. The beams are grown at 810° C and therefore fully metallic. In the process of cooling, the different thermal expansion coefficients of vanadium dioxide and sapphire lead to tensile strain on the nanobeams along the long axis (the *c*-axis). To reduce the overall tensile strain in the wire, parts of the beam switch into the insulating state, as it has a larger lattice constant, which is favorable in this configuration. These initially switched domains at high temperatures most likely occur at nucleation sites and also experience further strain when the wire continues cooling to room temperature. Below the phase transition temperature, the rest of the wire also turns into the insulating state, leading to a fully insulating wire that is composed of different parts: Some have experienced strain as they switched earlier and parts have incorporated less strain as they only became insulating due to the later change to lower temperature. Therefore, the pump-probe response and the switching susceptibility are encoded into the wire in its room temperature state. Heating the wire far above the transition temperature to another fully metallic state and cooling may reverse the process and potentially could lead to a different domain distribution.

4.2. Towards ultrafast switching of topologically protected Dirac particles

Throughout this thesis, we have seen that the addition of a high-quality surface phonon polariton to a surface plasmon polariton led to a reduced scattering rate of the combined hybrid polariton compared to the bare surface plasmon polariton. To achieve even lower scattering rates and, hence, longer polariton propagation, one can think about novel materials. A new class of materials, which is currently in the

center of much scientific attention, is that of topological insulators. The interest only grew with the 2016 award of the Nobel prize in physics to D. J. Thouless, F. D. M. Haldane and J. M. Kosterlitz "for theoretical discoveries of topological phase transitions and topological phases of matter"[1].

These new materials show intriguing properties with great promise for surface polaritons [Di 13]. Most notably, they host topologically protected surface states with Dirac-like dispersion and inhibited backscattering [And13]. These advantages could lead to long propagation lengths of surface polaritons in the topological surface state. To quickly recapitulate the most important features, the focus is set on three-dimensional topological insulators. Due to chemical bonding, crystal field splitting and spin-orbit coupling, the band structure in these materials is inverted in the bulk [Zha09a], meaning that the order of the conduction and the valence bands is reversed compared to conventional insulators for certain reciprocal lattice vectors. On the outside of the material, there is no reason for an inverted band structure so the band order is in the conventional state. This order is protected by the topology of the bands and consequently the order of the bands has to reverse at the material's surface. As a result, gapless, metallic surface states appear at the boundaries of the material, and these have been calculated to have Dirac-like dispersion and to connect the bulk valence and conduction band [And13]. This leads to the interesting virtue that the material shows hybrid character without heterostructuring: There is an insulating bulk material with a bandgap in the infrared [Zha11] and a protected surface state that supports Dirac-plasmons similar to those observed in graphene [Di 13, Lai14, Spe15]. Furthermore, the spin-orbit coupling leads to a spin-momentum locking, which means that the spin of the surface particles is coupled to their momentum and, hence, propagation direction. As a consequence, a strong suppression of back-scattering is seen, which should allow for long propagation lengths of surface plasmon polaritons [Zha09b]. Additionally, the electronic surface states, which host the propagating surface polariton modes, should also couple to the bulk electronic states, allowing for a tunable carrier concentration via photo-excitation of the semiconducting bulk material. Such optical control of the surface polaritons in topological insulators has a particularly interesting implication: In the unexcited

[1] "The Nobel Prize in Physics 2016". Nobelprize.org. Nobel Media AB 2014. Web. 20 Dec 2017. http://www.nobelprize.org/nobel_prizes/physics/laureates/2016/

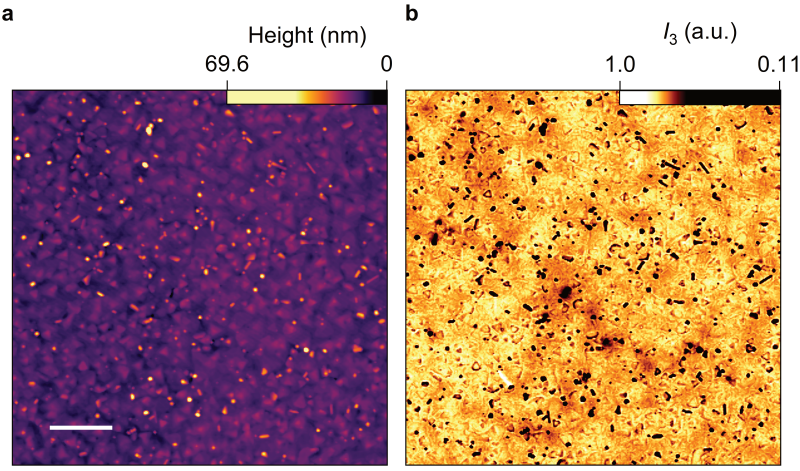

Figure 4.4. | Conductivity inhomogeneities in topological insulators. **a)** Height profile on a $(Bi_{5\%}Sb_{95\%})_2Te_3$ sample. The scale bar is 1 µm long. **b)** Scattered near-field intensity I_3 recorded with a quantum cascade laser operating at a frequency of 28.6 THz.

case, the surface plasmon polaritons are confined to the two-dimensional metallic surface state. Upon photo-excitation, however, it is possible to achieve a negative dielectric function also in the bulk semiconductor (comparable to the effects in the photo-excited black phosphorus layer in the previous chapter). Analogous to the discussion in the intuitive picture (section 3.5.1), the bulk could then support surface plasmon polaritons at its surface. This means, that there could be a change from a purely two-dimensional surface plasmon polariton to a surface plasmon polariton at a semi-infinite interface originating from the bulk plasma response. Alternatively, there could be an interaction of the two possible modes. Investigating the transition or the interference of the different polaritons could lead to new insights into the extension of the surface state into the material and the dielectric coupling of bulk and surface.

Here, the feasibility of the detection and control of Dirac-surface plasmon polaritons in topological insulators is studied on one example sample of the three dimensional

topological insulator $(Bi_{5\%}Sb_{95\%})_2Te_3$. In such compounds, the Fermi level and the location of the Dirac cone relative to the valence and conduction bands can be tuned with the antimony (Sb) concentration [Zha11]. A large scan across a sample grown by molecular beam epitaxy is shown in Fig. 4.4. The height profile (Fig. 4.4a) shows a crystal with many small triangular-shaped protrusions, which seem uniform in their orientation and density. The scattered near-field signal (Fig. 4.4b) reveals a different picture. The triangular shapes of the protrusions are also visible in the scan, however, there is also a large-scale inhomogeneity visible in the measurement where the intensity varies over large distances. This heterogeneity can be attributed to local changes in the conductivity of the sample. Transport and far-field measurements average over these differences. Hence, near-field microscopy is necessary to obtain a clear picture of the intrinsic properties of the material without spatial averaging. The detailed knowledge of the nanoscale sample properties can be used to improve the quality of the samples and to ultimately achieve Dirac surface plasmons. By now, flat regions with a uniformity down to the individual quintuple layer scale can be fabricated with lateral extensions exceeding 0.5 µm in Regensburg. This is a perfect starting point for future polaritonic studies.

Chapter 5

Conclusion

In this work, the ultrafast photo-activation of a hybrid interface polariton has been traced in real space for the first time. Complementary to approaches on graphene, the use of the direct bandgap semiconductor black phosphorus allows for high-contrast switching by interband excitation, in contrast to the previously demonstrated pure electron heating.

The polaritons are created in a custom-tailored heterostructure based on the semiconductor black phosphorus surrounded by silicon dioxide layers on a silicon substrate. The charge carriers in the photo-excited black phosphorus layer form a plasma response, which couples to probe pulses in the mid-infrared to form surface plasmon polaritons. These polaritons hybridize with strong mid-infrared surface phonon polariton modes in the surrounding silicon dioxide layers. This hybridization leads to the emergence of a completely new quasiparticle in the heterostructure – a coupled phonon-plasmon polariton that combines the virtues of both phonons and plasmons. The longitudinal optical phonon leads to a strong confinement in frequency close to the bare surface phonon resonance. Additionally, the mode inherits the sharp linewidth of the strong silicon dioxide phonon resonance, which allows for a long propagation length – significantly exceeding even state-of-the-art surface plasmon polaritons in encapsulated graphene at room temperature. In fact, the observed decay of the hybrid polariton is well described by pure geometrical decay, indicating negligible intrinsic damping across a propagation distance of 8 µm.

Meanwhile, from the surface plasmon polariton, the hybrid mode obtains its switchable character, as it is only present when the plasmon and phonon polaritons intersect at a particular frequency and wavelength in the complex dispersion relation of the Si/SiO_2/black phosphorus/SiO_2 heterostructure. The scattered near-field intensity changes by a factor of 350% upon photo-excitation, which demonstrates the striking influence of the plasmon on the mode: It exists only in the presence of the photo-activated surface plasmon. As a result, the mode can be switched on within $\approx 50\,\mathrm{fs}$, which is consistent with models for the build-up of screening.

Using nanoscopy, nano-spectroscopy and hyperspectral mapping, the full dispersion of the hybrid mode has been measured in the range of 31 THz to 36 THz. It shows a strong confinement not only in frequency, but also in in-plane wavevector k_x, which is a very favorable property for future nano-plasmonic devices where coupling with a single grating and a single frequency is desirable. This property has also allowed us to record the first ultrafast real-space snapshots of mid-infrared surface polariton photo-activation and the subsequent decay of the surface polariton.

Theoretically, the dispersion of the mode can be reproduced by calculating the imaginary part of the Fresnel reflection coefficient r_p of the multi-layered structure using a transfer matrix formalism. To understand the interplay between the different polaritonic modes in the heterostructure, a simple intuitive picture has also been provided based on the interaction between polariton modes at different interfaces. Furthermore, the interference of polaritonic modes at different surfaces of thin films has been discussed. The almost constant frequency and wavelength of the mode that is found throughout the experiments can be fully explained by the complete transfer matrix approach, while the intuitive picture provides a complementary, though less comprehensive description.

Furthermore, predictions on the behavior of the mode for different pump fluences have been experimentally verified, including a predicted broadening of the k_x-vector distribution of the hybrid mode. The exceptionally long propagation lengths of the hybrid mode have been explained by comparing them to theoretical propagation lengths for bare surface phonon polaritons in SiO_2. It has been found that the crossing of the plasmonic branch with the thin-film-split phonon branch allows for

a propagation of the coupled mode further than would be possible for the bare plasmonic mode.

The polariton lifetime has been estimated ($\approx 177\,\mathrm{fs}$) and compared to the carrier lifetime ($\approx 2.7\,\mathrm{ps}$) in the photo-excited structure. A small variation of the hybrid mode's center frequency with delay time is observed. Numerical simulations of an oscillator model with time dependent oscillation frequency have shown that the mode does not exhibit plasmon amplification.

Furthermore, shifting the center frequency of the probe radiation has revealed the existence of the uncoupled bare plasmonic response at low frequencies and corroborates the concept of a hybrid mode. A change in the pump wavelength also verifies the generality of the concept and shows that the hybrid mode can be created with at least two different pump configurations (appendix D). These results also rebut other explanations like the heterostructure acting as a waveguide for the pump pulses, which comes to mind since the polariton wavelength lies in a similar range to the initial pump wavelength.

Finally, the potential use of the structure in a polariton device is laid out and two other promising materials for ultrafast switchable devices are discussed. The metal-to-insulator phase transition in vanadium dioxide could be used for future storage devices and also be switched on ultrafast timescales.

In this thesis, it has been demonstrated that on a single crystalline nanobeam of vanadium dioxide, a built-in strain pattern has an essential influence on the ultrafast perturbative response of the material at room temperature and the switching susceptibility. Due to this interplay, near-field microscopy can be used at room temperature to pre-determine areas that are more or less likely to switch to the metallic state upon heating.

Furthermore, the potential of topological insulators as a new class of materials for switchable polaritons has been outlined. The description was extended by first measurements on three dimensional topological insulator samples grown at the University of Regensburg. The results show that near-field measurements are crucial to access the local conductivity of the material without averaging over different substructures.

In conclusion, ultrafast photo-activation of surface plasmon polaritons coupled with high quality surface phonon polariton modes is a viable route towards ultrafast polaritonic devices with low damping. Together with strain-tailoring of phase-change materials to modify their ultrafast optical response and switching susceptibility, devices with fully plasmonic logic and storage may be envisioned.

The exciting complementary opportunities provided by topological insulators might also open a new field in surface polaritonics where a single material can act as an ultrafast charge donor in the bulk to influence Dirac surface plasmon polaritons on its surface without the need for heterostructuring.

Appendix A

Ultrafast near-field microscopy setup

A.1. Schematic setup

The experiments in this work have been performed using the near-field microscope at the chair of Prof. Dr. Rupert Huber at the University of Regensburg. The setup is one-of-a-kind in that it features the shortest pump and probe pulses in the mid-infrared near-field community and is currently the only one that can perform electro-optic sampling of near-field waveforms in the mid-infrared spectral range [Eis14, Eis15].

It is based on a scattering-type scanning near-field optical microscope combined with an intricate laser setup to generate the pump and probe radiation. A simplified sketch of the setup is shown in Fig. A.1. The radiation is focused onto a sharp metalized tip (silicon tips with platinum/iridium coating, tip radius: 10 nm), which is used to sample the topography like in conventional atomic force microscopy. This approach also leads to a focusing of the near-fields below the tip to a volume smaller than achievable with conventional diffraction-limited optics. The sample is mounted onto a three-axis stage and is raster-scanned below the tip. The atomic force microscope is operated in tapping mode, which is a crucial prerequisite to disentangle the near-field contributions from the far-field parts in the scattered radiation (see below, section A.2). The pump and probe beams are focused onto the

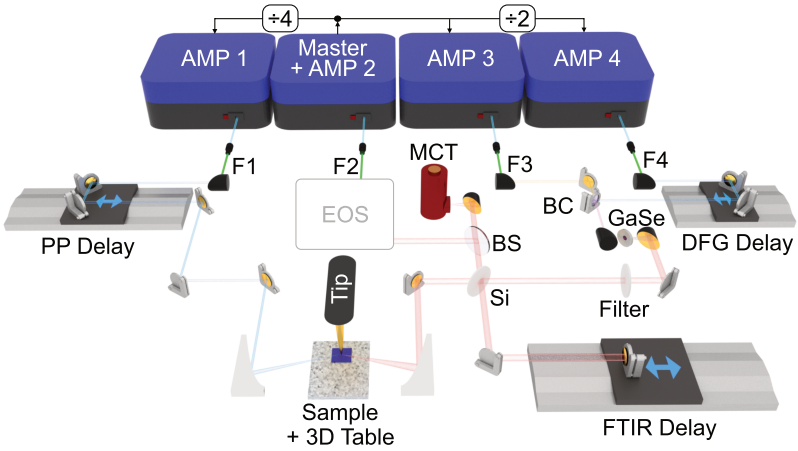

Figure A.1. | Ultrafast near-field microscopy setup in Regensburg. Schematic of the ultrafast near-infrared pump/mid-infrared probe near-field microscopy setup at the University of Regensburg. One master oscillator feeds four amplifiers (AMPs 1-4), of which some have a reduced repetition rate (÷2, ÷4). All laser outputs are coupled into nonlinear fibers (F1-F4) to spectrally and temporally shape the pulses. The output of AMP 3 and AMP 4 are combined with a beam combiner (BC) and focused into a gallium selenide (GaSe) crystal to produce mid-infrared radiation. A filter is used to eliminate the fundamental laser parts. A silicon (Si) wafer is used as a beam-divider for the Fourier transform infrared spectroscopy setup (FTIR) and a mercury cadmium telluride detector (MCT) for the intensity-resolved measurements. Furthermore, a beam splitter (BS) can send the radiation into an electro-optic sampling (EOS) setup. AMP 1 provides the pump pulses which are focused onto the AFM tip just like the mid-infrared radiation. Three delay stages control the timing for pump-probe delay (PP), FTIR time overlap and difference frequency generation overlap (DFG).

tip by fully non-dispersive optics to prevent a temporal stretching of the ultrashort pulses. The radiation for pump, probe and also the gate beam, which is necessary for electro-optic sampling are fully coherent. This is achieved by having a single master oscillator (repetition rate: 40 MHz) which feeds four amplifiers. To obtain the indispensable stability of the laser sources, an erbium-doped fiber laser is used

which can be operated for weeks without switching it on and off or readjusting the cavity. Also the amplifiers are based on erbium-doped fibers and provide four arms of ultrashort pulses (100 fs FWHM) at a center wavelength of 1560 nm. These pulses are subsequently spectrally and temporally tailored depending on their use in the setup. The output of amplifier 1 is used as pump radiation to photo-excite the sample. The pulses are compressed in a nonlinear fiber to obtain 40-fs-long pulses (FWHM) which are delayed with respect to the probe radiation via a delay stage and focused onto the tip via a parabolic mirror. The pulses of amplifier 2 are used as gating pulses for electro-optic sampling. As this technique was not extensively used for this work, it is reduced to a box in the schematic. In principle, it contains tailoring the pulses using nonlinear- and highly-nonlinear fibers and temporal compression using a prism compressor to obtain 10-fs-long pulses to sample the electric field of the probe radiation (for details see [Eis14, Eis15]). Amplifiers 3 and 4 are used to produce the mid-infrared probe radiation via difference frequency generation. To obtain short pulses in the desired spectral range, the pulses are compressed in a nonlinear fiber and the output of amplifier 4 is shifted in frequency using solitonic pulse propagation in a highly-nonlinear fiber. One obtains pulses centered at 1960 nm from the fiber, which are subsequently superimposed with the 1560 nm pulses of amplifier 3 in a nonlinear gallium selenide crystal where the temporal overlap is controlled by a delay stage (DFG Delay). Inside the crystal, the conversion of the incident frequencies of the two pulses to new frequencies is possible. By tuning the angle of incidence correctly the so-called critical phase matching is achieved. Using this approach one can favor the difference frequency mixing process over all other nonlinear processes and obtains radiation centered around the difference of the fundamental laser pulse wavelengths. Depending on the exact angle of the crystal, the process can be tailored to be more efficient in mixing the low or high frequency parts of the spectra leading to a tunability of the mid-infrared spectrum with accessible spectral components ranging from 15 THz to 60 THz. The remaining fundamental radiation exiting the crystal is filtered such that only the mid-infrared pulses are focused onto the microscopy tip with a parabolic mirror. There, the electric field of the probe pulses interacts with the sample via the near-field interaction below the tip and the modified response is scattered into the far field. The scattered radiation is collected by the same parabolic mirror which is used for the in-coupling process.

What is reflected back passes a silicon beam splitter and can be detected either field resolved via electro-optic sampling or intensity based in a mercury cadmium telluride (MCT) detector. The silicon beam splitter is also used to divide the probe radiation before it hits the metallic tip. One part is used as a reference which leads to a setup comparable to a Michelson interferometer. Using a temporal delay between the backscattered radiation and the reference arm allows to perform Fourier transform infrared spectroscopy (FTIR) of the scattered near-field radiation by means of the MCT detector. The recorded data are fed into a lock-in amplifier to extract the scattered near-field signal via demodulation techniques (see next section).

A.2. Demodulation technique

The radiation, which is scattered in the far field and detected using the MCT photodetector or electro-optic sampling, contains not only the near-field interaction below the tip, but also other contributions, for example light scattered off the sample or the cantilever. To differentiate these contributions from the pure near-field signal, which has the desired nanoscale spatial resolution, a lock-in demodulation technique is used. The near-field interaction of tip and sample is nonlinearly dependent on the distance of the tip from the sample. A commonly used approximation to see the nonlinear dependence describes the tip apex as metallic sphere with radius R_{tip} and polarizibility α_0 [Kei04]. The incoming electric field E_{in} induces a dipole moment in the tip, which is seen as a point dipole in the center of the sphere. Depending on the dielectric function of the sample $\varepsilon_{\mathrm{sample}}$, the electric field of the coupled system can be described via the interaction of the dipole and an image dipole below the sample surface leading to an effective polarizability α_{eff} of the system. The scattered electric field E_{scat}, which radiates into the far field, is then given by (see e.g. [Kei04])

$$E_{\mathrm{scat}} \propto (1 + r_{\mathrm{p}})^2 \alpha_{\mathrm{eff}} \cdot E_{\mathrm{in}} \tag{A.1}$$

$$= (1 + r_{\mathrm{p}})^2 \cdot \frac{\alpha_0}{1 - \frac{\alpha_0 \cdot \beta}{16\pi\varepsilon_0 \cdot (H_{\mathrm{tip}} + R_{\mathrm{tip}})^3}} \cdot E_{\mathrm{in}}, \tag{A.2}$$

where r_p is the Fresnel reflection coefficient for p-polarized light, $\beta = \frac{\varepsilon_\mathrm{sample}-1}{\varepsilon_\mathrm{sample}+1}$ defines the dielectric surface response and H_tip denotes the distance between tip and sample. The quantities E_scat, E_in, r_p, α_0, α_eff and β are all frequency dependent. However, for the sake of readability, the frequency dependence is dropped in the notation for all equations of this chapter. This is equivalent to an experimental setup with a monochromatic laser source. For pulsed laser operation, one would have to calculate the scattered field for each frequency contained in the pulse (an extensive derivation can be found in [Hub14] and the supplementary information of [Eis14]). It is clearly visible from the equation that the scattered near-field radiation scales nonlinearly with the tip height. This dependence can be utilized to extract the near-field contributions by modulating the height of the tip above the sample. This is already the case for the normal atomic force microscopy operation in tapping mode, where the tip is sinusoidally oscillating above the sample. As a result, the near field hits the detectors in bursts when the tip comes close to the sample [Wan15a]. Therefore, by filtering only the frequency components in the detected signal which are modulated with the tip frequency or higher harmonics of this frequency, one can suppress unwanted background radiation. Mathematically, the procedure can be described by decomposing the effective polarizability α_eff in a Fourier series of the tapping frequency Ω

$$\begin{aligned} E_\mathrm{scat} &\propto (1+r_\mathrm{p})^2 \alpha_\mathrm{eff} \cdot E_\mathrm{in} \\ &= (1+r_\mathrm{p})^2 \left(\sum_{\mathrm{n}=0}^{\infty} s_\mathrm{n} e^{i\phi_\mathrm{n}} \cdot e^{i\cdot \mathrm{n}\Omega\cdot t} \right) \cdot E_\mathrm{in}, \end{aligned} \tag{A.3}$$

where s_n and ϕ_n are the according scattering amplitudes and phases for each demodulation order n, respectively. In this thesis, the order of the harmonic is indicated by a subscript (e.g. I_4 means intensity measured at the fourth harmonic of the tip tapping frequency). Generally, the first order is still polluted by e.g. direct reflections off the cantilever, but for higher orders the signal becomes dominated by the near-field signal. Quantitatively, one can check if a signal originates from the near-field interaction by taking retraction scans. Hereby, the tip is retracted from the sample while maintaining the oscillatory motion. This leads to retraction curves of the detected signal which – for pure near-field interaction – decay rapidly when moving away from

the surface. Harmonics with pollution show modulations and non-vanishing signals at large distances from the tip (several hundreds of nanometers) due to far-field interference effects.

For the measurements in this thesis, high orders were shown (third and fourth harmonic), which in previous experiments on the setup have been found to be purely near-field sensitive [Eis14]. Additionally, retraction scans on gold were taken for each new tip to verify this assumption and to ascertain that the signal stems purely from the local near field.

Another interesting side effect, which has been shown in near-field microscopy, is that by changing the tapping amplitude, one can change the effective probing depth inside the material. From an intuitive point of view, this seems reasonable since a change in the dipole oscillation above the sample would also influence the depth of the image dipole inside the material (for dielectric media). The dependence has also been measured in experiments on buried structures [Kru12]. Furthermore, it has been found that the signal stemming from the different harmonic orders also show different decay characteristics below the tip apex [Gov14]. Therefore, also the different orders probe different volumes inside the sample. Higher orders hereby are more surface sensitive. These insights can reveal further interesting effects inside a material and can, for example, be used to trace the ultrafast build-up of a surface depletion layer in indium arsenide nanowires [Eis14]. In this work, the high orders used in the experiment lead to a shallow probing of the surface polaritons. Nevertheless, since the mode is a hybrid mode composed of polar oscillations in all layers of the structure, using the different orders as a depth-sensitive measurement could be misleading as it is one collective response, which contributes to the measured signal even though only the effects localized close to the surface are probed. Looking at the different orders is, however, crucial for pure intensity-based detection methods to verify that no artifacts appear (see section A.4).

A.3. Pulse characterization

The characteristics of the near-field setup are crucially dependent on the utilized laser radiation. The system can be used for time-resolved or steady-state measurements. For the equilibrium measurements on topological insulators and vanadium dioxide nanobeams, continuous-wave quantum cascade lasers with a center frequency of 28.6 THz and 36 THz were used to probe the sample. For the steady state experiments on black phosphorus and all time-resolved experiments, the pulsed laser sources shown in Fig. A.1 are utilized. The wavelength of the pump pulse determines if and where carriers are injected in the band structure of a semiconducting sample. The probe spectrum determines the range in which the polariton can be observed. Furthermore, when performing ultrafast near-field microscopy, the temporal resolution, which determines the shortest independent measurable step in time, is given by the duration of the pulses. It is hence essential to know the properties of the laser pulses impinging onto the near-field tip.

Ultrafast multi-terahertz probe pulses

The ultrafast probe pulses in the experiment are produced via difference frequency generation in a 1-mm-thick gallium selenide crystal and can be tuned to access spectral components from 15 THz to 60 THz. In the measurements on the black phosphorus heterostructures, the configuration with the highest mid-infrared power was used, which results in a Gaussian shaped spectrum centered at roughly 36 THz (pulse energy 30 pJ). The spectrum is typically modified by resonances in the tip. For this reason, the spectrum reflected off a gold reference substrate is used to determine the probe bandwidth of the pulse. The data are shown in Fig. 3.8a and show a small local maximum around 37.5 THz which only slightly modifies the Gaussian line shape of the pulse with a center frequency of 36.3 THz and a full width at half maximum (FWHM) of 6.8 THz. In Fig. A.2a a typical transient of the laser source is shown for a center frequency of 36 THz. The electro-optical waveform shows an intensity pulse duration (gray) with a FWHM of 67 fs which corresponds to 2.4 optical cycles at this frequency (red curve). The spectral amplitude and phase is plotted in Fig. A.2b and shows that the phase (red curve) of the pulse is almost flat over the spectral bandwidth.

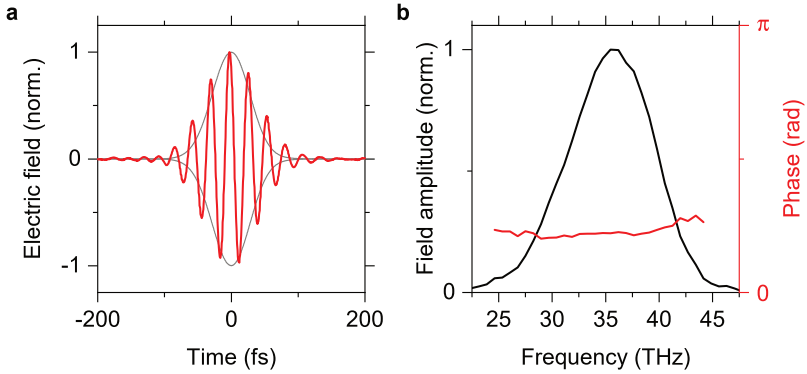

Figure A.2. | Probe pulse characterization. a) Electro-optically sampled waveform (red) and intensity envelope (gray) of a typical probe pulse of the laser source. **b)** Spectral amplitude and phase of the pulse.

Ultrafast near-infrared pump pulses

The laser pulses from amplifier 1, which are used for photo-excitation of the sample, can be characterized by frequency-resolved optical gating (FROG) [Tre97]. Here, the pulse is split into two parts which are correlated with one another using a delay line. However, instead of recording the intensity-correlation of the pulses, they are focused non-collinearly into a nonlinear crystal to generate the second harmonic of the superposition of both pulses. Detecting the spectrum of the second harmonic radiation for each delay time between the two pulses leads to characteristic FROG traces which can be reconstructed numerically. From the reconstruction, the spectral and temporal shape of the pulse can be obtained. The result for the pump beam centered at a wavelength of 1560 nm is shown in Fig. A.3. The obtained FROG trace and its reconstruction are shown in Fig. A.3a. An intense pulse is seen, centered at the time zero of the measurement which spans in frequency (FWHM) from 375 THz (799 nm) to 406 THz (738 nm) and has some faint contributions at larger time delays. The reconstruction shows good agreement to the experimental data and yields a pulse which is characterized in Fig. A.3b. It has a highly structured spectral amplitude, which is typical for this type of erbium-doped fiber laser, and

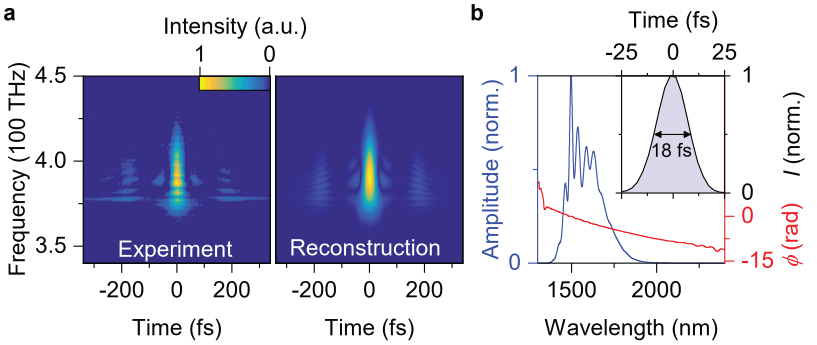

Figure A.3. | Pump pulse characterization. a) Experimentally measured (left) and reconstructed (right) FROG traces of the pump pulse. **b)** Pulse characteristics retrieved from the reconstruction. The spectral amplitude and phase are shown as a function of frequency. Inset: Temporal intensity profile of the pulse.

a fairly linear phase. The highest amplitude in the spectrum is seen at 1497 nm, but the center of the pulse is roughly at 1560 nm, which corresponds to the central local minimum in the spectral amplitude. The pulse has a FWHM duration of 18 fs, however the faint wings in the FROG trace indicate that there is a small pedestal below the pulse. It is not possible to measure the pulse at the position of the tip. Therefore, the shown characteristics of the pulse are valid for the pulse after spectral shaping in a nonlinear fiber where solitonic pulse compression is used to shorten the pulse to 18 fs. Subsequently, there are some dispersive optical elements (i.e. an indium tin oxide window, a half-wave plate and a linear polarizer), which temporally stretch the pulse. Accounting for the dispersion in these downstream components, the pulse, which impinges on the tip, has a calculated pulse duration of 40 fs (FWHM).

In appendix D, a black phosphorus heterostructure is investigated with pump pulses at different wavelengths. This is achieved by frequency doubling of the pulses described above in a periodically-poled lithium niobade crystal. Also in section 4.1, the vanadium dioxide sample was photo-exited with the frequency-doubled laser pulses of amplifier 1. The pulses in these cases were not shaped by optical fibers to increase

the maximum achievable pulse power. For the vanadium dioxide measurements, the repetition rate of the laser was set to 20 MHz and an intensity autocorrelation revealed a pulse duration of 150 fs FWHM. The repetition rate was set to 10 MHz for the black phosphorus heterostructures to reduce the thermal load on the sample and prevent degradation.

A.4. Measurement techniques

Based on the demodulation technique detailed above, different measurement techniques can be applied to perform experimental studies on the sample under investigation.

Topography and steady-state imaging

Since the setup is based on an atomic force microscope with a metallic tip, its conventional application is the mapping of the sample topography by raster-scanning the sample below the tip. The tip is tapped above the sample with a tapping frequency on the order of 285 kHz. Depending on the force interaction of the tip with the sample, the resonance frequency of the tip shifts slightly when the sample is moved closer or further away from the tip. As a consequence, the measured tapping amplitude at a fixed frequency changes. Using this signal as a feedback to keep the tapping amplitude constant by moving the sample closer to or farther away from the tip, the height at the exact position of the tip with respect to the previous location on the sample can be determined. This leads to a map of relative topography of the structures on the sample.

Simultaneously, the scattered near-field intensity can be extracted at each point using the demodulation technique explained in section A.2 to obtain the local scattering intensity of the sample. Typically, continuous-wave illumination is used and the intensity detected by a MCT photodiode. From the contrast between different spots on the sample, changes in the dielectric function of the material can be extracted. This allows to overcome the diffraction limit and reach a spatial resolution on the order of the radius of curvature of the utilized probe tip (≈ 10 nm).

Pump-probe measurements

To extend the detection scheme and enable the resolution of ultrafast dynamics, pulsed sources are used, which allow for pump-probe detection. Here, a pump pulse excites the material under investigation and a temporally delayed probe pulse samples the response of the material at different times after photo-excitation. Typically, different frequency regimes for pump and probe pulses are used to easily differentiate the induced sample response (e.g. the change in the local conductivity) from the excitation at a different frequency. Using the characteristic demodulation technique and detecting signals at higher orders of the tip tapping frequency, it has been shown that pump-probe measurements also work in the near field [Eis14, Wag14a, Wag14b, Eis15, Hub16]. Thereby, the spatial resolution can be enhanced to the low two-digit nanometer domain. The temporal resolution depends critically on the detection technique and the pulse durations of the pump and probe pulse. When only the intensity is mapped at each point in space and delay time, the best temporal resolution is given by a convolution of the pump pulse with the scattered probe pulse. As we have seen in section A.3, the probe pulse in this setup are ≈ 60 fs long and the pump pulses 40 fs. Therefore the best temporal resolution is on the order of 60 fs. However, if the pulse samples a strong resonance, it will obtain distinct ringing features from the free induction decay of the resonance. This leads to a deterioration of the temporal resolution in intensity-resolved measurements. Electro-optic sampling is a way to overcome this limitation (see below).

Together with the emergence of near-field pump-probe measurements, also the awareness of potential problems with the intensity-resolved (pump-probe) studies has increased. Our group has laid out this problem already in the supplementary information of the first publication [Eis14] in a rigorous calculation of the near-field signals based on the point-dipole model. The scattered intensity is given by the absolute square of the scattered electric field

$$I_{\mathrm{scat}} = |E_{\mathrm{scat}}|^2. \tag{A.4}$$

Entering equation A.3 and extracting only the contribution of the scattered intensity at one particular demodulation order n, one obtains (calculation see [Eis14, Hub14,

Eis15])

$$I_{\mathrm{n}} \propto (1 + r_{\mathrm{p}})^2 \cdot (1 + r_{\mathrm{p}}^*)^2 \cdot \sum_{\mathrm{k}=0}^{\infty} s_{\mathrm{n+k}} s_{\mathrm{k}} \cdot e^{i \cdot (\phi_{\mathrm{n+k}} - \phi_{\mathrm{k}})} \cdot |E_{\mathrm{in}}|^2. \tag{A.5}$$

It can easily be seen that the near-field intensity measured at, for example, the third harmonic of the tapping frequency is not purely the third-harmonic frequency decomposition of the near-field signal, but it is an infinite sum of two different components which can produce radiation at the third harmonic of the tip tapping frequency. The leading term is the multiplication of the zeroth order with the third harmonic but also the first and the fourth, the second and the fifth, ... orders contribute to the signal. The higher order terms are not necessarily a considerable problem, as typically the scattering process decreases the amplitude of the different orders strongly from one order to the next. However, already the leading term shows a distinct problem in the interpretation: The largest term is not purely originating from near-field interaction as it contains the zeroth order, which is the far-field reflection of the full sample. For steady-state imaging this fact has been long used as an advantage to increase the contrast of the measurement by utilizing a strongly reflecting substrate [Aiz08]. Although this is a reasonable approach for homogeneous substrates in steady-state imaging, this has to be taken carefully for pump-probe measurements. In every case where the far-field reflection could be dependent on the pump pulses, the detected signal at the third harmonic cannot be taken as the signal change solely at the tip position. Instead, it also originates from the surrounding area, which is illuminated by the pump spot. This area can be orders of magnitude larger than the near-field region below the tip. Especially pump-probe studies on large films are problematic in this respect as the global change will be modulated onto the local response. Therefore, we have always checked whether there is a change in the zeroth order to verify that no artifacts appear. Additionally, we found that for our samples, which are small (nanowires [Eis14], nanobeams [Hub16] or micron-scale flakes [Hub16]) compared to the area of bare substrate around it – which does not exhibit a pump-probe response – the changes genuinely stem from the near-field response below the tip. For the black phosphorus heterostructures an exemplary pump-probe measurement including all demodulation orders from the zeroth to the fifth order is shown in Fig. A.4. Here, the scattered intensity detected at the x-th

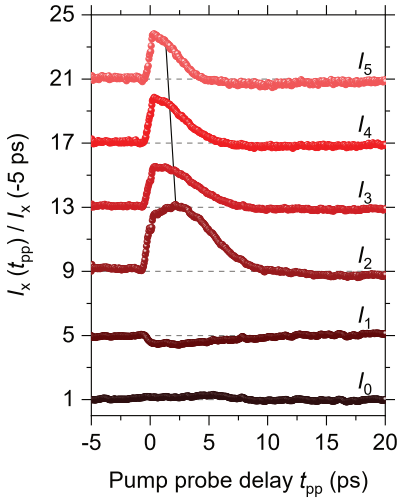

Figure A.4. | Pump-induced change for different demodulation orders. The scattered near-field intensity recorded on a black phosphorus heterostructure normalized to the first value is shown in a waterfall plot as a function of pump-probe delay time t_{pp}.

harmonic of the tapping frequency is plotted as a function of pump-probe delay time. Additionally, the data have been normalized to the first recorded value, 5 ps before the pump pulse arrives. It is clearly visible that the zeroth order does not contain any pump-probe response. There is only a slight fluctuation around the equilibrium position due to drift in the mid-infrared pulse power. The first order pump-probe scan shows only a slight dip below the baseline and should not be over-interpreted as it is typically polluted by artifacts of light scattered off the cantilever or regions at the base of the tip. The second order is more trustworthy to show a local sample response, however, should also not be used for extensive explanations. Starting from the third order, the pump-probe trace looks comparable for all recorded orders, which is a good indication that it is the genuine near-field response. We see the characteristic increase upon photo-excitation followed by a decay to the baseline within roughly 5 ps and a subsequent slight dip below the baseline for a delay time of up to $t_{pp} = 20$ ps. A tiny detail, which should be mentioned, is, that there is a faint shoulder in the pump-probe response at roughly $t_{pp} = 1.7$ ps which can be seen in orders two to five and is not corresponding to an intensity increase in the mid-infrared radiation as it should be seen in the zeroth order. Most notably, the

elevation is shifting for the different orders (marked by a black line). This might stem from the nonlinear response function of the scattered intensity as a function of the carrier density inside the material, or might be a feature which appears at different times for different probing depths inside the sample. As the peak shifts to later delay times for lower orders, the interpretation suggests a feature that appears at later times for deeper probing in the material. It is not fully understood what the origin of the feature is. The lines start and end points are at 1.3 ps and 2.2 ps, respectively, leading to a shift of 0.9 ps. If it is related to a feature which propagates along the vertical direction of the structure from the surface to the bottom, it cannot spread with the same speed as in lateral direction as it would have reached $\approx 65\,\mu m$ after this time – almost three orders of magnitude more than the thickness of the actual heterostructure.

As a further note, the images which were taken at different delay times also fall into the category of an intensity pump-probe measurement as only the scattered intensity was measured and not an interference pattern with an external reference arm (which is possible and currently done in other labs to reduce the far-field pollution in the scans of photo-excited large films). However, since no change to the scattered radiation was seen in the zeroth order images they can be seen as practically background free. The constraint "practically" is used here as there can still be contributions of the first order mixed with the fifth order and higher mixings, but the intensity of the scattered near-field intensity drops strongly for each increasing demodulation order, such that the mixing of zeroth with fourth order, which we observed, is the dominant one and the others only induce a negligible effect. Furthermore, the fringe pattern is clearly visible in the hyperspectral mapping, which is a spectrally-resolved measurement and does not suffer from far-field pollution effects (see next subsection).

Fourier transform infrared spectroscopy

To disentangle the spectral composition of the near-field radiation scattered from the sample and not only record the pump-induced change in intensity, Fourier transform infrared spectroscopy can be used to extract the amplitude spectrum of the near field as well as the relative phase to the incident mid-infrared radiation. This technique does not suffer from the previously mentioned limitations by pollution of the zeroth order intensity. The reason is that a reference pulse is overlapped with the pulse scattered from the tip-sample system. The measured intensity for a certain delay τ between the scattered and the reference electric fields is hence given by

$$I(\tau) = |E_{\mathrm{in}} \cdot e^{i\omega\tau} + E_{\mathrm{scat}}|^2, \tag{A.6}$$

where ω denotes the angular frequency of the oscillating electric field (for pulsed sources see reference [Hub14] and supplementary information of reference [Eis14]). Only the factors which contain a convolution of the reference field and the scattered field contribute delay-dependent information to the measured interferogram. Hence, there is no more mixing of two near-field responses which eliminates the multiple cross-terms in the intensity-resolved section above (see equation A.5). As a result, the measured intensity at the n-th demodulation order after some algebraic transformations (see referenec [Hub14]) is given by

$$I_{\mathrm{n}} \propto (1 + r_{\mathrm{p}})^2 \cdot s_{\mathrm{n}} e^{i\phi_{\mathrm{n}}} \cdot |E_{\mathrm{in}}|^2. \tag{A.7}$$

We see that the signal does only depend on the Fourier component of the effective polarizability α_{eff} of the order n (see equation A.3) and is not polluted by contributions of any other order. It can thus probe the spectral change in the sample below the tip upon photo-excitation with nanoscale precision when measuring at higher demodulation orders (e.g. third or fourth order). The same is true for the hyperspectral mapping described in section 3.6. The only drawback for this detection method is that it is intrinsically limited to the duration of the longer one of the pump or probe pulses. The probe pulse duration must also be taken after interaction with the sample, which might lead to a further decrease in temporal resolution.

Electro-optic sampling

To achieve a better temporal resolution than possible with FTIR measurements, electro-optic sampling can be used as it allows for sub-cycle temporal resolution. Here, an ultrashort gate pulse is used to sample the electric field of the scattered waveform after interaction with the sample. At the University of Regensburg, we currently have the only near-field setup which is able to resolve the scattered electric field from the mid-infrared near field of a tip [Eis14]. The technique can be used to sample pump-probe responses with a temporal resolution down to 10 fs and additionally yields the spectral evolution including the absolute phase of the pulses. With this technique the plasmon propagation could be investigated in real time as a next step. For the responses on the black phosphorus heterostructures, where a spectral sampling with larger time steps was sufficient to disentangle the intricate physics of the system, FTIR spectroscopy has been the first means of choice. The reason is that the direct resolution of only 50 photons in the coherent field, which has been demonstrated in the InAs nanowires [Eis14], is a very demanding task and FTIR can yield better signal-to-noise ratios for the same integration times.

Appendix B

Transfer matrix method

The theoretical discussion of the formation and properties of the hybrid phonon-plasmon-polariton mode is based on numerical calculations of the dispersion of the coupled SiO_2/black phosphorus system. In section 2.1.1 it has been shown that the imaginary part of the Fresnel reflection coefficient r_p as a function of frequency and in-plane wavevector k_x can visualize the dispersion of coupled modes in a structure. To calculate the coefficient r_p of the multi-layered systems in this thesis, a transfer matrix approach is used [Abe50, Sal07].

Regarding forward (F) and backward (B) traveling waves in a medium i which encounter a boundary to another medium j = i + 1 (for detail see Fig. B.1) we can write the electric field distributions in medium i and i+1 as follows:

$$E_{\mathrm{F,i+1}} = t_{\mathrm{i,i+1}} E_{\mathrm{F,i}} + r_{\mathrm{i+1,i}} E_{\mathrm{B,i+1}} \tag{B.1}$$

$$E_{\mathrm{B,i}} = r_{\mathrm{i,i+1}} E_{\mathrm{F,i}} + t_{\mathrm{i+1,i}} E_{\mathrm{B,i+1}} \tag{B.2}$$

Here, $r_{\mathrm{i,j}}$ is the Fresnel reflection coefficient between layer i and j and $t_{\mathrm{i,j}}$ is the coefficient of transmission through interface i,j. The approach is indifferent to whether the perpendicular or transverse polarization component of the electric field is considered. In the experiment p-polarized light is utilized. Therefore, we consider the

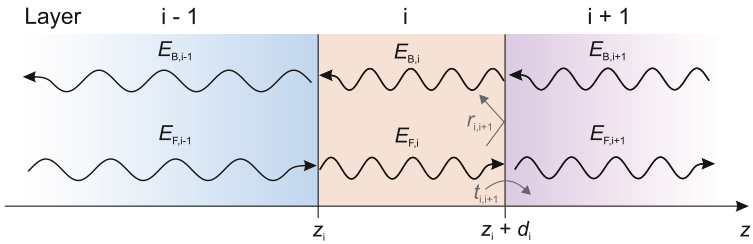

Figure B.1. | Electric field distribution inside a multilayer structure. Sketch of the forward (F) and backward (B) propagating electromagnetic waves in the layers i−1, i and i+1 of a multi-layered structure. $r_{\mathrm{i,i+1}}$ and $t_{\mathrm{i,i+1}}$ specify the reflection or transmission of electromagnetic waves at the interface between layer i and i+1, respectively.

Fresnel reflection coefficient r_{p} which is given by:

$$r_{\mathrm{i,j}} = \frac{\varepsilon_{\mathrm{j}} k_{\mathrm{z,i}} - \varepsilon_{\mathrm{i}} k_{\mathrm{z,j}}}{\varepsilon_{\mathrm{j}} k_{\mathrm{z,i}} + \varepsilon_{\mathrm{i}} k_{\mathrm{z,j}}} \tag{B.3}$$

where ε_{i} and ε_{j} are the frequency dependent dielectric functions of the materials in layer i and j (see also discussion of equation 2.14 in section 2.1.1). Furthermore, the out-of-plane wavevectors $k_{z,\mathrm{i}}$ and $k_{z,\mathrm{j}}$ in layer i and j are required, which can be calculated according to equation 2.4 in section 2.1 from the dielectric functions ε_{i} and ε_{j} in combination with the chosen in-plane wavevector k_x. Equations B.1 and B.2 can be cast in matrix form leading to one matrix $\mathbf{R}_{\mathrm{i,j}}$

$$\mathbf{R}_{\mathrm{i,j}} = \frac{1}{t_{\mathrm{i,j}}} \begin{bmatrix} 1 & r_{\mathrm{i,j}} \\ r_{\mathrm{i,j}} & 1 \end{bmatrix}, \tag{B.4}$$

which link the vector of forward and backward propagating waves in layer j to the ones in layer i via

$$\begin{pmatrix} E_{\mathrm{F,i}} \\ E_{\mathrm{B,i}} \end{pmatrix} = \mathbf{R}_{\mathrm{i,j}} \begin{pmatrix} E_{\mathrm{F,j}} \\ E_{\mathrm{B,j}} \end{pmatrix}. \tag{B.5}$$

For a multi-layered system one can use this matrix to calculate the electric fields going through all media by multiplying matrices with the according dielectric func-

tions for each layer into one effective matrix for the whole system. For this purpose, however, the thickness d_i of each layer i must be taken into account as well. Each additional slab of material adds a phase to the electric field, which it collects from one side to the other side of the material. Therefore the forward and backward traveling waves have to be adjusted using

$$E_{\mathrm{F,i}}(z + d_\mathrm{i}) = E_{\mathrm{F,i}}(z) \cdot e^{i \cdot k_{z,\mathrm{i}} d_\mathrm{i}} \tag{B.6}$$

$$E_{\mathrm{B,i}}(z) = E_{\mathrm{F,i}}(z + d_\mathrm{i}) \cdot e^{-i \cdot k_{z,\mathrm{i}} d_\mathrm{i}}. \tag{B.7}$$

For ease of use, this formula can also be recast into matrix form to use in a matrix multiplication

$$\mathbf{T}_{\mathrm{i,j}} = \begin{bmatrix} e^{ik_{z,\mathrm{i}} d_\mathrm{i}} & 0 \\ 0 & e^{-ik_{z,\mathrm{i}} d_\mathrm{i}} \end{bmatrix}. \tag{B.8}$$

This leads to the following equation for all five layers in our system (air, SiO_2, BP, SiO_2, Si, see sketch 3.1)

$$\mathbf{M} = \begin{bmatrix} M_{\mathrm{aa}} & M_{\mathrm{ab}} \\ M_{\mathrm{ba}} & M_{\mathrm{bb}} \end{bmatrix} = \left(\sum_{i=1}^{3} \mathbf{R}_{\mathrm{i,i+1}} \cdot \mathbf{T}_{\mathrm{i+1}} \right) \cdot \mathbf{R}_{4,5} \tag{B.9}$$

Note that the first and last medium are assumed to be half-infinite for which reason the phase adjustment is only done for the layers in between (i $\in \{2,3,4\}$). From this we obtain a matrix $\mathbf{M}$ which corresponds to the effective change to the electric fields in the heterostructure. Looking closely at equation B.4 one finds that the Fresnel reflection coefficient $r_{\mathrm{i,j}}$ can in return be extracted from the matrix elements M_{ba} and M_{aa} (defined in equation B.9). As the matrix $\mathbf{M}$ takes into account the complete structure, $r_{\mathrm{i,j}}$ is in this case equivalent to the Fresnel reflection coefficient of the complete sample r_p leading to

$$r_\mathrm{p} = \frac{M_{\mathrm{ba}}}{M_{\mathrm{aa}}}. \tag{B.10}$$

Appendix C

Dielectric functions used for the modeling

To accurately model the dispersion relation in the black phosphorus heterostructures, the dielectric functions of the constituents of the air/SiO_2/black phosphorus/SiO_2/silicon structures have to be determined. For air, a real valued dielectric function $\varepsilon_{\mathrm{Air}} = 1$ is used. Silicon features a flat dielectric response in the observed frequency window with a dielectric constant of $\varepsilon_{\mathrm{Si}} = 11.9$ [Mad04].

The dielectric function of silicon dioxide is determined by the phonon resonances in the Reststrahlen bands, which have also been clearly seen in the simulations (e.g. Fig. 3.12 and Fig. 3.13) and led to the intriguing interplay of the surface plasmon and phonon polaritons. To correctly describe the dielectric function, a sum of Lorentz oscillators is used

$$\varepsilon_{\mathrm{SiO_2}}(\omega) = \varepsilon_\infty + \sum_\nu \frac{\delta\varepsilon_\nu \cdot \Omega_{\mathrm{T}\nu}^2}{\Omega_{\mathrm{T}\nu}^2 - \omega^2 - i\omega\gamma_{\mathrm{T}\nu}}, \tag{C.1}$$

where the parameters of $\delta\varepsilon_\nu$, $\Omega_{\mathrm{T}\nu}$ and $\gamma_{\mathrm{T}\nu}$ are based on reference [Gun00]. To reproduce the experimental data of the same publication, a constant dielectric background of $\varepsilon_\infty = 1.3$ is added to the sum of Lorentz oscillators to account for high frequency oscillators in the visible and ultraviolet spectral range. Near-field measurements of silicon dioxide [Fei11] have shown that the resonances are sharper than suggested in reference [Gun00]. For this reason, the scattering rate of the oscillators in the simulations is decreased to $0.6 \cdot \gamma_{\mathrm{T}\nu}$ of the literature values to obtain the best

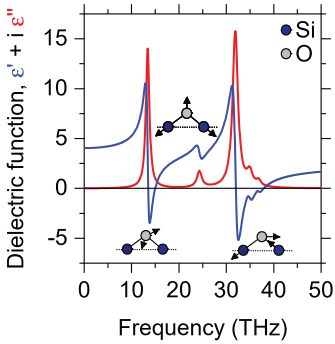

Figure C.1. | Dielectric function of silicon dioxide. Plotted is the real (ε') and imaginary (ε'') part of the dielectric function used for for the modelling of silicon dioxide within this thesis. The details of the chosen literature values are given in the text. Additionally, the three dominant phonon modes are characterized by small pictograms (see also Ref. [Kir88]).

reproduction of the data in [Fei11], while still maintaining information about all phonon resonances in a large spectral range. In reference [Woe15], a similar modification of the damping is performed to increase the visibility of the modes. The location of the modes is not strongly affected by this change. Another study on surface phonon polaritons in silicon dioxide [Huc16] uses an even lower damping of $\gamma = 10\,\mathrm{cm}^{-1}$ ($\approx 0.3\,\mathrm{THz}$) for their spectral and near-field simulations or neglect it completely. From the measurements on the heterostructures, this seems too small for the silicon dioxide layers in the experiment such that the modification of γ by a constant factor of 0.6 is kept as the most realistic description for the system in all simulations of this work. The resulting dielectric function in the frequency range from 0 to 50 THz is plotted in Fig. C.1. Both, the real part (blue curve) and the imaginary part (red part) show the several phonon modes in this spectral region. The different modes can be grouped in three different areas where a large imaginary part is visible. To each of these regions a characteristic motion of the silicon and oxygen atoms can be attributed [Gun00, Kir88]. These oscillation patterns are visualized via small pictographs in Fig. C.1. The lowest lying resonance around 13.4 THz is accompanied by a rocking motion of the oxygen atoms with respect to the silicon atoms. At $\approx 24.3\,\mathrm{THz}$ a symmetric stretching of both constituents leads to the observed resonance, which is smaller in magnitude than in the other regions. In the area around 31.9 THz, there are actually three phonon resonances close together but the dominant one is an asymmetric stretching of the oxygen atoms with respect to the silicon atoms.

In contrast to silicon dioxide, black phosphorus is not a polar material and therefore does not exhibit optical phonon resonances in the investigated spectral range. The biggest contribution is hence given by the free carriers which are photo-activated upon laser excitation. For this reason the dielectric function of black phosphorus is described via the Drude model (see equation 2.20). To estimate the scattering rate and the plasma frequency, the values reported in reference [Qia14] are used to obtain the room temperature mobilities of electrons and holes. Both carrier types are incorporated in the description by calculating a reduced mobility μ_r and a reduced mass m_r from the electron and hole mobilities and masses μ_e, μ_h and m_e, m_h, respectively, via

$$m_\mathrm{r} = (1/m_\mathrm{h} + 1/m_\mathrm{e})^{-1}$$
$$\mu_\mathrm{r} = (1/\mu_\mathrm{h} + 1/\mu_\mathrm{e})^{-1}.$$

From these quantities the scattering rate τ can be obtained via

$$\tau = \frac{m_\mathrm{r}\mu_\mathrm{r}}{e},$$

where e is the electron charge. The strong in-plane anisotropy of the material renders an exact calculation of the scattering time and carrier density challenging since the specific orientation of the crystal axes in the flakes is not known a priori. Experiments on exemplary structures have shown that characterization with Raman measurements led to a strong degradation of the flakes, which inhibited further investigations on these heterostructures.

Therefore, in the simulations the average of the in-plane effective masses has been used to obtain a coarse estimate of carrier density and scattering time. The scattering time is thus determined to be $\approx 74\,\mathrm{fs}$, which corresponds to a scattering rate of $13.5\,\mathrm{THz}$. The plasma frequency is the only free fitting parameter of the simulations and for the excited structure with a plasma frequency of $38\,\mathrm{THz}$ (e.g. Fig. 3.12b), the corresponding carrier density is in the range of $\approx 5 \cdot 10^{18}\,\mathrm{cm}^{-3}$. In comparison with literature [Woo15, Li15, Low14b], these carrier densities are on the low end of the reported values.

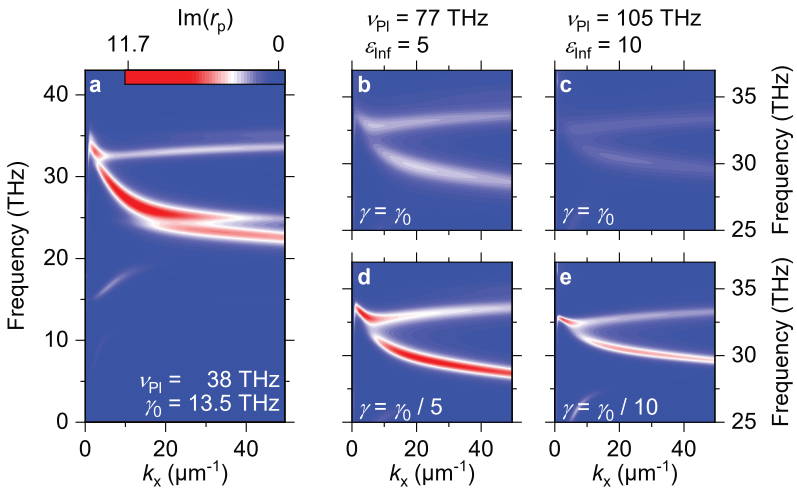

Figure C.2. | Effect of the dielectric background on the polariton dispersion. a) Dispersion diagram visualized via the imaginary part of the Fresnel reflection coefficient r_p as shown in the main text of the thesis. **b), c), d), e)** Dispersion diagrams zoomed into the region of the crossing of the surface phonon polariton and the surface plasmon polariton for different dielectric backgrounds ($\varepsilon_{Inf} = 5$ in **b, d** and $\varepsilon_{Inf} = 10$ in **c, e**) and adapted plasma frequencies for an intersection. The upper row (**b, c**) shows the dispersion without modification of the plasmon scattering rate, whereas for the lower row (**d, e**) the scattering is reduced by the inverse of the dielectric background.

The dielectric background ε_{Inf} of the black phosphorus flakes has been set to unity as in equation 2.20 to reduce the fitting parameters to one unknown value. Generally, calculations show that the dielectric background at low frequencies can reach values of up to 10 [Mor86]. Therefore, Fig. C.2, shows a comparison of an exemplary dispersion diagram for the heterostructures for three different dielectric background values of black phosphorus. In Fig. C.2a the calculated dispersion visualized via the imaginary part of r_p is shown for $\varepsilon_{Inf} = 1$ as it has been calculated in the main text. In panels b - e the dielectric background is varied to values of 5 and 10. For a dielectric background different from unity, the zero crossing of the dielectric function is no longer at the position of the bare plasma frequency as defined in section 2.1.2

but is also modified by a factor of $1/\sqrt{\varepsilon_{\mathrm{Inf}}}$. To keep the notation as in the main text, the plasma frequency given in the figure is the bare plasma frequency without correcting for the dielectric background. As a result this number must increase for $\varepsilon_{\mathrm{Inf}}$ larger than one to keep the intersection point of the surface phonon mode and the surface plasmon mode in the relevant spectral range. Accounting for this fact, it is clearly visible, that the discussed physics of the hybridization of the surface phonon polariton and the surface plasmon polariton is valid for all three different values of $\varepsilon_{\mathrm{Inf}}$, when keeping the scattering rate constant (Figs. C.2a, b, c). The increase in the dielectric background mainly influences the slope of the surface plasmon such that the intersection point shifts to slightly larger k_x values and leads to a broadening of the mode. The confinement of the hybrid mode is thereby made less visible. This effect can, however, be compensated by reducing the scattering rate of the flakes accordingly. Division of the scattering rate proportional to the dielectric background (Figs. C.2d, e) leads to a pronounced re-appearance of the hybrid mode compared to the images for the undivided scattering rate. In these cases the strong localization of the mode in frequency and momentum is conserved. Therefore, the physics of the hybridization of the surface plasmon and surface phonon polariton modes is valid also for dielectric background values $\varepsilon_{\mathrm{Inf}}$ in the range from 1 to 10.

Appendix D

Excitation energy dependence of the polaritons

The concept of ultrafast photo-activation of a hybrid mode should apply generally and not depend on the wavelength of the excitation laser. As long as the laser photon energy overcomes the bandgap of black phosphorus the activation should be possible. In other words, only the instantaneous plasma frequency should determine if the hybrid polariton can be launched, with an additional, less prominent correction due to the carrier scattering rate and effective mass. Therefore, it is a good proof of concept to change the center frequency of the pump laser and check if the standing wave pattern persists. In the experiment, a periodically-poled lithium niobate crystal is used to frequency double the pump pulses and obtain a center wavelength of 780 nm.

In a first step, the pump-probe response is tested on a heterostructure, once with the original excitation laser with a center wavelength of 1560 nm and once after frequency doubling. The results are plotted in Fig. D.1, where the scattered mid-infrared near-field intensity is shown as a function of pump-probe delay time for the two different pump configurations. The change from the baseline differs by roughly a factor of two in the peak scattered intensity. This difference can be directly related to the amount of absorbed photons in the heterostructure. Due to the higher photon energy of the 780 nm pump laser, the pulses contain only half

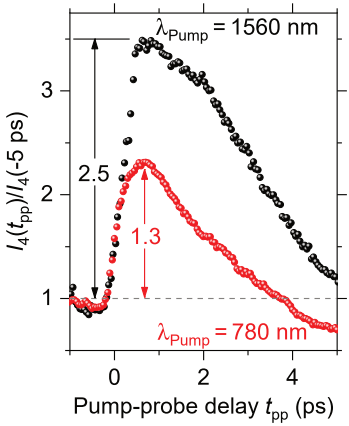

Figure D.1. | Pump-induced change for different excitation energies. The scattered mid-infrared near-field intensity is plotted as a function of delay time upon photo-excitation, once for a pump laser with a center wavelength of 1560 nm (black spheres) and once after frequency doubling of the pulses, leading to a new center wavelength of 780 nm (red spheres). The maximum change of the signal relative to the baseline is denoted with black (red) arrows and equals 2.5 (1.3) for 1560 nm (780 nm).

as many photons as the 1560 nm pump pulses, since the pump fluence has been equal for both measurements. The slight deviation from an exact factor of two can potentially be explained by slight differences in the combined density of states at the two wavelengths and the non-trivial relation of the measured near-field response on the density and effective masses of the excited carriers. The latter effect could also be the reason for the slightly different shape of the two pump-probe curves. The curve at 780 nm excitation wavelength recovers to the value of unity faster than for the longer excitation wavelength. Nevertheless, both pump wavelengths have the potential to excite free carriers in the heterostructure. As a next step the standing wave patterns in the scattered near-field intensity formed by the hybrid polariton will be investigated.

The topography of the flake measured by atomic force microscopy is shown in Fig. D.2a. Two folds at the edges of the scan are visible, as is a single distortion running at an oblique angle. The scattered near-field signal of the structure is shown in Fig. D.2b and c, for a pump wavelength of 1560 nm and 780 nm, respectively. The oblique distortion can be used to correlate the features because it appears as a dark line in the near-field scans. The image taken with the 1560 nm center wavelength pump pulses shows the well known fringe pattern of the hybrid mode. In this case, the first two fringes have merged into one bright area. Nevertheless, there are two

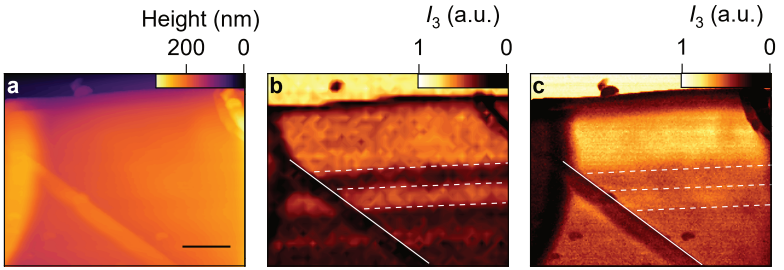

Figure D.2. | Influence of the pump pulse frequency on the polariton wavelength. a) AFM scan of an example heterostructure. The scale bar is 1 µm long. **b)** Interference pattern in the scattered near-field intensity I_3 as a function of position with a pump wavelength of 1550 nm. The solid white line highlights a topographical feature and the white dashed lines outline the polariton fringe pattern. **c)** Same scan as in **b**, only this time for a pump wavelength of 780 nm.

more stripes parallel to the edge of the flake with increased contrast. The edges of the merged fringes and of the one consecutive stripe are marked with white dashed lines. Superimposing these white dashed lines onto the image for the excitation wavelength of 780 nm shows an agreement in the fringe pattern resolved for the two pump configurations. Specifically, the second scan shows a clear bright region at the top edge of the flake and one distinctive fringe further from the edge at exactly the same locations where the analogous fringes were observed in the first scan. The contrast of the pattern is, however, weaker. This may be because the carriers excited by the different wavelengths have different scattering times: The 780 nm pump photons excite carriers into higher energetic bands than the 1560 nm pump, where the carriers may have a higher scattering rate, in addition to a modified effective mass. Furthermore, for identical pump fluences, as in Fig. D.1, the 780 nm pump photon number is half that of the 1560 nm pump, leading to a smaller plasma frequency, a lower carrier density, and potentially a modified scattering rate compared to the 1560 nm pump. The modified plasma frequency produced by the 780 nm pump is comparable to what is observed at a different pump-probe delay time or pump fluence for the 1560 nm pump. Notably, also in the cases of the 1560 nm pump, the

fringe pattern is less prominent for lower plasma frequencies (Fig. 3.7, Fig. 3.14). An increase of the pump power to compensate this effect is, however, not possible without destroying the heterostructure.

Overall, the similarity in the pattern is a convincing argument that the hybrid mode is a general property of the material and does not depend on the wavelength of the pump laser. Therefore, the alternate hypothesis that the periodic fringe pattern could be related to thin-film interference at the pump wavelength due to the heterostructure acting as a waveguide can be experimentally excluded. If this were the case, the fringe periodicity would change with the frequency of the excitation laser, but it does not. Additionally, such an effect would lead to a pattern that would most likely be visible across the whole flake, not only at the edges.

Appendix E

Finite differences method

In section 3.8, the oscillation of a photo-induced polariton with a time-dependent instantaneous frequency and damping was described by a straightforward oscillator model. The important differential equation 3.8

$$\left[\partial_t^2 + \gamma(t)\partial_t + \omega(t)\right] X(t) = 0 \tag{E.1}$$

to describe the evolution of the order parameter of the polariton oscillation in time can be solved numerically using a finite differences method[1]. In this approach, the evolution of X in time is discretized in a finite number of time steps between a starting time and an end time with a spacing Δt. The full evolution is stored in a single vector $\vec{X}$ which contains entries of X at each time step. The operators to the left-hand side of X can be cast in matrix form to act on the vector $\vec{X}$. The differential operator ∂_t can be written as a matrix by calculating the derivative at each point by the difference between neighboring points:

$$\partial_t = \frac{1}{\Delta t}\begin{pmatrix} 0 & 1 & 0 & & \dots & 0 \\ -1 & 0 & 1 & 0 & \dots & 0 \\ 0 & -1 & 0 & 1 & \dots & 0 \\ \vdots & & & \ddots & & \vdots \\ \vdots & & & & \ddots & \vdots \\ 0 & & \dots & 0 & -1 & 0 \end{pmatrix}. \tag{E.2}$$

[1] The technique is adapted from the lecture *Computational Methods in Electrical Engineering* by Dr. Raymond C. Rumpf (University of Texas at El Paso).

Applying this matrix onto $\vec{X}$ transforms every entry of the vector into the difference of its neighboring points divided by the grid spacing, which equals – to first order – the derivative at the point. For the second order derivative ∂_t^2 analogous reasoning for the curvature at each point leads to a matrix form of

$$\partial_t^2 = \frac{1}{(\Delta t)^2} \begin{pmatrix} -2 & 1 & 0 & & \dots & 0 \\ 1 & -2 & 1 & 0 & \dots & 0 \\ 0 & 1 & -2 & 1 & \dots & 0 \\ \vdots & & & \ddots & & \vdots \\ \vdots & & & & \ddots & \vdots \\ 0 & & \dots & 0 & 1 & -2 \end{pmatrix}. \tag{E.3}$$

The factors $\gamma(t)$ and $\omega(t)$ depend on the time and are known for the given problem (see section 3.8). The time dependence of the quantities must also be discretized and leads to vectors $\vec{\gamma}$ and $\vec{\omega}$ which have the same dimension as $\vec{X}$. The multiplications of these vectors with $\vec{X}$ are performed by a matrix which contains the elements of $\vec{\gamma}$ or $\vec{\omega}$, respectively, on the diagonal:

$$\gamma(t) = \begin{pmatrix} \gamma_0 & 0 & 0 & & \dots & 0 \\ 0 & \gamma_1 & 0 & 0 & \dots & 0 \\ 0 & 0 & \gamma_2 & 0 & \dots & 0 \\ \vdots & & & \ddots & & \vdots \\ \vdots & & & & \ddots & \vdots \\ 0 & & \dots & 0 & 0 & \gamma_N \end{pmatrix}. \tag{E.4}$$

From these matrizes one operator matrix can be calculated for given $\gamma(t)$ and $\omega(t)$. To obtain $\vec{X}$ the matrix must only be inverted and applied to the right-hand side of the equation. This side is equal to zero, but also contains boundary conditions. The matrices shown above assume Dirichlet-type boundaries, which means that the value of $\vec{X}$ for the initial and the final point are known. These values have to be added to the zero-vector of the right hand side of the equation. In the thesis, the amplitude at the starting time was set to one and at the final time to zero. Exemplary results for different time dependent scattering rates $\gamma(t)$ and instantaneous frequencies $\omega(t)$ are shown in Fig. 3.21 of the main text.

Appendix F

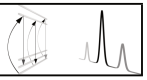

Raman measurements on a single VO_2 nanobeam

In section 4.1, the strain in the investigated vanadium dioxide nanobeam was experimentally measured on the 1-µm-scale using micro-Raman measurements. The measurements were performed with Prof. Dr. T. Korn in their Raman setup at the University of Regensburg. A continuous-wave laser with a wavelength of 532 nm is used. The laser is focused to a spot with a diameter of 1 µm on the sample via an objective with a magnification factor of 100. Further details on the Raman setup can be found in Ref. [Ple14].

To construct the two-dimensional map of the local strain (Fig. 4.3), the Raman frequency of a characteristic vanadium-oxygen phonon mode at frequency ω_O was extracted for different locations on the sample. This mode is particularly interesting, as it can be used to determine the strain in the material and also differentiate between the possible phases of insulating vanadium dioxide [Jon10, Atk12a]. Depending on the amount of tensile strain in the material, the position of the peak blueshifts and the material goes from the monoclinic M1 to the monoclinic M2 phase, passing the triclinic T phase in the process. Representative Raman spectra for a series of different amounts of tensile strain are shown in Fig. F.1. The gray lines indicate spectra taken from the literature (i.e. Ref. [Atk12a]). The blueshift of the peak from the M1 to the M2 phase can nicely be traced for increasing tensile strain.

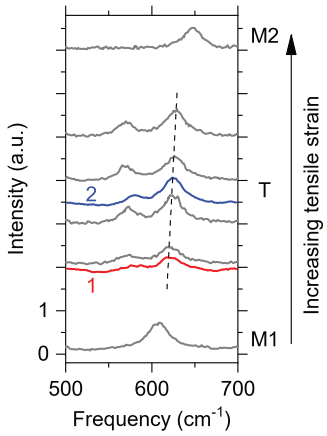

Figure F.1. | Raman spectra on vanadium dioxide. Raman spectra of different phases of vanadium dioxide taken from Ref. [Atk12a] are shown in gray. They show the location of one characteristic phonon peak for the insulating M1 and M2 phase, as well as the crossover region of the insulating T phase. In red and blue, two representative spectra taken on the nanobeam of section 4.1 are shown.

In the triclinic phase a second minor peak emerges at lower frequencies, which is, however, not essential for our extraction of the local strain on the nanobeam.

Added to the figure are two example spectra taken on the nanobeam (red and blue curves). The spectra show, that the nanobeam features the characteristic double-peak of the triclinic phase on both locations. However, apart from being in the same phase, the nanobeam shows distinctive differences in the value of the peak center position and, hence, the intrinsic tensile strain. The red curve (1) was taken right at the end of the nanobeam and the blue curve (2) corresponds to a position in the center of the single crystalline region of the beam. The main peak position at the end of the wire is at $\omega = 624\,\mathrm{cm}^{-1}$. Comparing this value with literature data (Ref. [Atk12a]), a relative tensile strain of 0.57% can be attributed to this position. This value is at the lower boundary of where the triclinic phase appears, close to the M1 phase. In the center of the single crystalline region, the peak position is at $\omega = 625\,\mathrm{cm}^{-1}$, which corresponds to a relative tensile strain of 0.6% in this region.

The change in peak position is also nicely visible in Fig. 4.3, where the center of the single crystalline part of the wire has a distinctly different color (i.e. ω_O frequency) than the ends of the single crystalline region. This shows, that the nanobeam is under less strain at both ends of the single crystalline region, which is consistent

with the observation of the ultrafast pump-probe measurements (Fig. 4.2b). At the ends of the single crystalline region, a higher pump-probe peak signal is observed, which we correlated with less tensile strain. Due to the limited spatial resolution of the (far-field) Raman measurements, the strain in the interesting sub-domains which turned metallic or stayed insulating cannot be differentiated via micro-Raman experiments but are averaged over.

Nevertheless, the ultrafast near-field microscopy measurements show a modulation in the height of the maximum pump-induced intensity signal on the scale of the heterogeneity, which can be explained by the effects of strain on the bandgap and the transition energy (see section 4.1). Combined with the added knowledge of the Raman measurements on the ends of the single crystalline region compared to the central part, we have a strong indication that the modulation indeed stems from a built-in local strain pattern.

Appendix G

Publications

Publications in Peer-reviewed journals

- M. A. Huber, F. Mooshammer, M. Plankl, L. Viti, F. Sandner, L. Z. Kastner, T. Frank, J. Fabian, M. S. Vitiello, T. L. Cocker, and R. Huber
  Femtosecond photo-switching of interface polaritons in black phosphorus heterostructures
  Nature Nanotechnology **12,** 207–211 (2017)

  This work has been featured in a News and Views article:
  D. N. Basov and M. M. Fogler
  Quantum materials: The quest for ultrafast plasmonics
  Nature Nanotechnology **12,** 187–188 (2017)

- M. A. Huber, M. Plankl, M. Eisele, R. E. Marvel, F. Sandner, T. Korn, C. Schüller, R. F. Haglund, Jr., R. Huber, and T. L. Cocker
  Ultrafast mid-infrared nanoscopy of strained vanadium dioxide nanobeams
  Nano Letters **16,** 1421–1427 (2016)

- M. Eisele, T. L. Cocker, M. A. Huber, M. Plankl, L. Viti, D. Ercolani, L. Sorba, M. S. Vitiello, and R. Huber
  Ultrafast multi-terahertz nano-spectroscopy with sub-cycle temporal resolution
  Nature Photonics **8,** 841–845 (2014)

This work has been featured in a News and Views article:
H. Shigekawa, S. Yoshida, and O. Takeuchi
Spectroscopy: Nanoscale terahertz spectroscopy
Nature Photonics **8,** 815–817 (2014)

Publications in international conference proceedings

- M. A. Huber, F. Mooshammer, M. Plankl, L. Viti, F. Sandner, L. Z. Kastner, T. Frank, J. Fabian, M. S. Vitiello, T. L. Cocker, and R. Huber
  Femtosecond switch-on of hybrid polaritons in black phosphorus heterostructures
  Proceedings IRMMW-THz (2017), DOI: 10.1109/IRMMW-THz.2017.8066876
- R. Huber, F. Langer, S. Baierl, U. Huttner, S. W. Koch, M. Kira, M. A. Huber, F. Mooshammer, M. Plankl, D. Peller, T. L. Cocker, and J. Repp
  Terahertz subcycle control: from high-harmonic generation to molecular snapshots
  Nonlinear Optics: Materials, Fundamentals and Applications, Paper# NW2A.5 (2017)
- M. A. Huber, F. Mooshammer, M. Plankl, L. Viti, F. Sandner, L. Z. Kastner, T. Frank, J. Fabian, M. S. Vitiello, T. L. Cocker, and R. Huber
  Ultrafast Photo-activation of Surface Polaritons in Black Phosphorus Heterostructures
  QELS Fundamental Science, Paper# FF2F.3 (2017)
- M. Eisele, T. L. Cocker, M. A. Huber, M. Plankl, L. Viti, D. Ercolani, L. Sorba, M. S. Vitiello, and R. Huber
  Femtosecond Infrared Nano-spectroscopy with Sub-cycle Temporal Resolution
  International Conference on Ultrafast Phenomena, Paper# UW1A.4 (2016)

- T. L. Cocker, M. A. Huber, M. Eisele, M. Plankl, L. Viti, R. E. Marvel, F. Sandner, F. Mooshammer, T. Korn, C. Schüller, D. Ercolani, L. Sorba, R. F. Haglund, Jr., M. S. Vitiello, and R. Huber
  Taking sub-cycle THz nanoscopy to the limits
  CLEO: Science and Innovations, Paper# SW1L.4 (2016)

First author contributions at international conferences

- M. A. Huber, F. Mooshammer, M. Plankl, F. Sandner, L. Viti, M. S. Vitiello, T. L. Cocker, and R. Huber,
  Femtosecond nanoscopy of collective excitations in semiconductors
  DPG spring meeting, Germany, Invited Talk (2018)
- M. A. Huber, F. Mooshammer, M. Plankl, L. Viti, F. Sandner, L. Z. Kastner, T. Frank, J. Fabian, M. S. Vitiello, T. L. Cocker, and R. Huber,
  Femtosecond Switch-On of Hybrid Polaritons in Black Phosphorus Heterostructures
  42nd International Conference on Infrared, Millimeter and Terahertz Waves, Mexico, Talk (2017)
- M. A. Huber, F. Mooshammer, M. Plankl, L. Viti, F. Sandner, L. Z. Kastner, T. Frank, J. Fabian, M. S. Vitiello, T. L. Cocker, and R. Huber,
  Ultrafast nanoscopy of plasmons in nanowires and heterostructures
  9th THz days, Dunkirk, Invited Talk (2017)
- M. A. Huber, M. Plankl, M. Eisele, R. E. Marvel, L. Viti, D. Ercolani, L. Sorba, F. Sandner, T. Korn, C. Schüller, R. F. Haglund, Jr., M. S. Vitiello, T. L. Cocker, and R. Huber,
  Ultrafast mid-infrared near-field microscopy of nanowires - from semiconductors to phase-transitions
  THz Workshop, Erice, Invited Talk (2016)
- M. A. Huber,
  Ultrafast near-field microscopy - watching electrons oscillate on the nanoscale
  66th Lindau Nobel Laureate Meeting, Germany, Invited Talk (2016)

- M. A. Huber, M. Plankl, M. Eisele, R. E. Marvel, F. Sandner, T. Korn, C. Schüller, R. F. Haglund, Jr., R. Huber, and T. L. Cocker
  Ultrafast multi-terahertz nanoscopy of strained vanadium dioxide nanobeams
  DPG Spring Meeting, Germany, Talk (2016)
- M. A. Huber, T. L. Cocker, M. Eisele, M. Plankl, C. Pöllmann, P. Steinleitner, P. Nagler, G. Plechinger, M. Porer, R. Bratschitsch, C. Schüller, T. Korn, and R. Huber
  Ultrafast terahertz dynamics in 2D systems
  International Conference on 'Single-Molecule Electronics', Germany, Poster (2015)
- M. A. Huber, M. Eisele, T. L. Cocker, M. Plankl, L. Viti, D. Ercolani, L. Sorba, M. S. Vitiello, and R. Huber
  Ultrafast field-resolved multi-terahertz nano-spectroscopy
  CLEO®/Europe - EQEC 2015, Germany, Talk (2015)
- M. A. Huber, M. Eisele, T. L. Cocker, M. Plankl, L. Viti, D. Ercolani, L. Sorba, M. S. Vitiello, and R. Huber
  Ultrafast sub-cycle terahertz nano-spectroscopy
  Winter School on Ultrafast Processes in Condensed Matter, Germany, Talk (2015)

Bibliography

[Abb73] E. Abbe, *Beiträge zur Theorie des Mikroskops und der mikroskopischen Wahrnehmung*, Archiv für Mikroskopische Anatomie **9**, 413–418 (1873).

[Abe50] F. Abelès, *La théorie générale des couches minces*, Journal de Physique et le Radium **11**, 307–309 (1950).

[Abr12] E. Abreu, M. Liu, J. Lu, K. G. West, S. Kittiwatanakul, W. Yin, S. A. Wolf, and R. D. Averitt, *THz spectroscopy of VO_2 epitaxial films: controlling the anisotropic properties through strain engineering*, New Journal of Physics **14**, 083026 (2012).

[AG14] P. Alonso-González, A. Y. Nikitin, F. Golmar, A. Centeno, A. Pesquera, S. Vélez, J. Chen, G. Navickaite, F. Koppens, A. Zurutuza, F. Casanova, L. E. Hueso, and R. Hillenbrand, *Controlling graphene plasmons with resonant metal antennas and spatial conductivity patterns*, Science **344**, 1369–1373 (2014).

[AG16] P. Alonso-González, A. Y. Nikitin, Y. Gao, A. Woessner, M. B. Lundeberg, A. Principi, N. Forcellini, W. Yan, S. Vélez, A. J. Huber, K. Watanabe, T. Taniguchi, F. Casanova, L. E. Hueso, M. Polini, J. Hone, F. H. L. Koppens, and R. Hillenbrand, *Acoustic terahertz graphene plasmons revealed by photocurrent nanoscopy*, Nature Nanotechnology **12**, 31–35 (2016).

[Aiz08] J. Aizpurua, T. Taubner, F. J. García de Abajo, M. Brehm, and R. Hillenbrand, *Substrate-enhanced infrared near-field spectroscopy*, Optics Express **16**, 1529–1545 (2008).

[And13] Y. Ando, *Topological Insulator Materials*, Journal of the Physical Society of Japan **82**, 102001 (2013).

[Ank08] J. N. Anker, W. P. Hall, O. Lyandres, N. C. Shah, J. Zhao, and R. P. Van Duyne, *Biosensing with plasmonic nanosensors*, Nature Materials **7**, 442–453 (2008).

[Atk12a] J. M. Atkin, S. Berweger, E. K. Chavez, M. B. Raschke, J. Cao, W. Fan, and J. Wu, *Strain and temperature dependence of the insulating phases of VO_2 near the metal-insulator transition*, Physical Review B **85**, 020101 (2012).

[Atk12b] J. M. Atkin, S. Berweger, A. C. Jones, and M. B. Raschke, *Nano-optical imaging and spectroscopy of order, phases, and domains in complex solids*, Advances in Physics **61**, 745–842 (2012).

[Bal17] F. Balzarotti, Y. Eilers, K. C. Gwosch, A. H. Gynnå, V. Westphal, F. D. Stefani, J. Elf, and S. W. Hell, *Nanometer resolution imaging and tracking of fluorescent molecules with minimal photon fluxes*, Science **355**, 606–612 (2017).

[Bar03] W. L. Barnes, A. Dereux, and T. W. Ebbesen, *Surface plasmon subwavelength optics*, Nature **424**, 824–830 (2003).

[Bas16] D. N. Basov, M. M. Fogler, and F. J. García de Abajo, *Polaritons in van der Waals materials*, Science **354**, aag1992–aag1992 (2016).

[Bas17] D. N. Basov and M. M. Fogler, *The quest for ultrafast plasmonics*, Nature Nanotechnology **12**, 187–188 (2017).

[Bie05] S. Biermann, A. Poteryaev, A. I. Lichtenstein, and A. Georges, *Dynamical Singlets and Correlation-Assisted Peierls Transition in VO_2*, Physical Review Letters **94**, 026404 (2005).

[Bro82] A. D. Broadman, *Electromagnetic Surface Modes*, John Wiley & Sons, Ltd., Chichester, New York, Brisbane, Toronto, Singapore, 1982.

[Bro03] M. L. Brongersma, *Nanoscale photonics: Nanoshells: gifts in a gold wrapper*, Nature Materials **2**, 296–297 (2003).

[Cal15] J. D. Caldwell, L. Lindsay, V. Giannini, I. Vurgaftman, T. L. Reinecke, S. A. Maier, and O. J. Glembocki, *Low-loss, infrared and terahertz nanophotonics using surface phonon polaritons*, Nanophotonics **4**, 44–68 (2015).

[Cal16] J. D. Caldwell, I. Vurgaftman, J. G. Tischler, O. J. Glembocki, J. C. Owrutsky, and T. L. Reinecke, *Atomic-scale photonic hybrids for mid-infrared and terahertz nanophotonics*, Nature Nanotechnology **11**, 9–15 (2016).

[Cav04] A. Cavalleri, T. Dekorsy, H. H. W. Chong, J. C. Kieffer, and R. W. Schoenlein, *Evidence for a structurally-driven insulator-to-metal transition in VO_2: A view from the ultrafast timescale*, Physical Review B **70**, 161102 (2004).

[CG14a] A. Castellanos-Gomez, M. Buscema, R. Molenaar, V. Singh, L. Janssen, H. S. J. van der Zant, and G. A. Steele, *Deterministic transfer of two-dimensional materials by all-dry viscoelastic stamping*, 2D Materials **1**, 011002 (2014).

[CG14b] A. Castellanos-Gomez, L. Vicarelli, E. Prada, J. O. Island, K. L. Narasimha-Acharya, S. I. Blanter, D. J. Groenendijk, M. Buscema, G. A. Steele, J. V. Alvarez, H. W. Zandbergen, J. J. Palacios, and H. S. J. van der Zant, *Isolation and characterization of few-layer black phosphorus*, 2D Materials **1**, 025001 (2014).

[CG15] A. Castellanos-Gomez, *Black Phosphorus: Narrow Gap, Wide Applications*, The Journal of Physical Chemistry Letters **6**, 4280–4291 (2015).

[Che12] J. Chen, M. Badioli, P. Alonso-González, S. Thongrattanasiri, F. Huth, J. Osmond, M. Spasenović, A. Centeno, A. Pesquera, P. Godignon, A. Zu-

rutuza Elorza, N. Camara, F. J. García de Abajo, R. Hillenbrand, and F. H. L. Koppens, *Optical nano-imaging of gate-tunable graphene plasmons*, Nature **487**, 77–81 (2012).

[Che14] A. Chernikov, T. C. Berkelbach, H. M. Hill, A. Rigosi, Y. Li, O. B. Aslan, D. R. Reichman, M. S. Hybertsen, and T. F. Heinz, *Exciton Binding Energy and Nonhydrogenic Rydberg Series in Monolayer WS_2*, Physical Review Letters **113**, 076802 (2014).

[Coc12] T. L. Cocker, L. V. Titova, S. Fourmaux, G. Holloway, H.-C. Bandulet, D. Brassard, J.-C. Kieffer, M. A. El Khakani, and F. A. Hegmann, *Phase diagram of the ultrafast photoinduced insulator-metal transition in vanadium dioxide*, Physical Review B **85**, 155120 (2012).

[Coc13] T. L. Cocker, V. Jelic, M. Gupta, S. J. Molesky, J. A. J. Burgess, G. D. L. Reyes, L. V. Titova, Y. Y. Tsui, M. R. Freeman, and F. A. Hegmann, *An ultrafast terahertz scanning tunnelling microscope*, Nature Photonics **7**, 620–625 (2013).

[Coc16] T. L. Cocker, D. Peller, P. Yu, J. Repp, and R. Huber, *Tracking the ultrafast motion of a single molecule by femtosecond orbital imaging*, Nature **539**, 263–267 (2016).

[Dąb17] M. Dąbrowski, Y. Dai, and H. Petek, *Ultrafast Microscopy: Imaging Light with Photoelectrons on the Nano–Femto Scale*, The Journal of Physical Chemistry Letters **8**, 4446–4455 (2017).

[Dai14] S. Dai, Z. Fei, Q. Ma, A. S. Rodin, M. Wagner, A. S. McLeod, M. K. Liu, W. Gannett, W. Regan, K. Watanabe, T. Taniguchi, M. Thiemens, G. Dominguez, A. H. C. Neto, A. Zettl, F. Keilmann, P. Jarillo-Herrero, M. M. Fogler, and D. N. Basov, *Tunable Phonon Polaritons in Atomically Thin van der Waals Crystals of Boron Nitride*, Science **343**, 1125–1129 (2014).

[Dai15] S. Dai, Q. Ma, M. K. Liu, T. Andersen, Z. Fei, M. D. Goldflam, M. Wagner, K. Watanabe, T. Taniguchi, M. Thiemens, F. Keilmann, G. C. A. M.

Janssen, S.-E. Zhu, P. Jarillo-Herrero, M. M. Fogler, and D. N. Basov, *Graphene on hexagonal boron nitride as a tunable hyperbolic metamaterial*, Nature Nanotechnology **10**, 682–686 (2015).

[Dai17] S. Dai, Q. Ma, Y. Yang, J. Rosenfeld, M. D. Goldflam, A. McLeod, Z. Sun, T. I. Andersen, Z. Fei, M. Liu, Y. Shao, K. Watanabe, T. Taniguchi, M. Thiemens, F. Keilmann, P. Jarillo-Herrero, M. M. Fogler, and D. N. Basov, *Efficiency of Launching Highly Confined Polaritons by Infrared Light Incident on a Hyperbolic Material*, Nano Letters **17**, 5285–5290 (2017).

[Di 13] P. Di Pietro, M. Ortolani, O. Limaj, A. Di Gaspare, V. Giliberti, F. Giorgianni, M. Brahlek, N. Bansal, N. Koirala, S. Oh, P. Calvani, and S. Lupi, *Observation of Dirac plasmons in a topological insulator*, Nature Nanotechnology **8**, 556–560 (2013).

[Dog15] R. A. Doganov, E. C. T. O'Farrell, S. P. Koenig, Y. Yeo, A. Ziletti, A. Carvalho, D. K. Campbell, D. F. Coker, K. Watanabe, T. Taniguchi, A. H. C. Neto, and B. Özyilmaz, *Transport properties of pristine few-layer black phosphorus by van der Waals passivation in an inert atmosphere*, Nature Communications **6**, 6647 (2015).

[Dru00] P. Drude, *Zur Elektronentheorie der Metalle*, Annalen der Physik **306**, 566–613 (1900).

[Eco69] E. N. Economou, *Surface Plasmons in Thin Films*, Physical Review **182**, 539–554 (1969).

[Eis14] M. Eisele, T. L. Cocker, M. A. Huber, M. Plankl, L. Viti, D. Ercolani, L. Sorba, M. S. Vitiello, and R. Huber, *Ultrafast multi-terahertz nano-spectroscopy with sub-cycle temporal resolution*, Nature Photonics **8**, 841–845 (2014).

[Eis15] M. Eisele, *Ultrafast multi-terahertz nano-spectroscopy with sub-cycle temporal resolution*, Doctoral thesis, University of Regensburg (2015).

[Emm15] M. Emmrich, F. Huber, F. Pielmeier, J. Welker, T. Hofmann, M. Schneiderbauer, D. Meuer, S. Polesya, S. Mankovsky, D. Kodderitzsch, H. Ebert, and F. J. Giessibl, *Subatomic resolution force microscopy reveals internal structure and adsorption sites of small iron clusters*, Science **348**, 308–311 (2015).

[Fan41] U. Fano, *The Theory of Anomalous Diffraction Gratings and of Quasi-Stationary Waves on Metallic Surfaces (Sommerfeld's Waves)*, Journal of the Optical Society of America **31**, 213–222 (1941).

[Feh15] M. Fehrenbacher, S. Winnerl, H. Schneider, J. Döring, S. C. Kehr, L. M. Eng, Y. Huo, O. G. Schmidt, K. Yao, Y. Liu, and M. Helm, *Plasmonic Superlensing in Doped GaAs*, Nano Letters **15**, 1057–1061 (2015).

[Fei11] Z. Fei, G. O. Andreev, W. Bao, L. M. Zhang, A. S. McLeod, C. Wang, M. K. Stewart, Z. Zhao, G. Dominguez, M. Thiemens, M. M. Fogler, M. J. Tauber, A. H. C. Neto, C. N. Lau, F. Keilmann, and D. N. Basov, *Infrared Nanoscopy of Dirac Plasmons at the Graphene–SiO_2 Interface*, Nano Letters **11**, 4701–4705 (2011).

[Fei12] Z. Fei, A. S. Rodin, G. O. Andreev, W. Bao, A. S. McLeod, M. Wagner, L. M. Zhang, Z. Zhao, M. Thiemens, G. Dominguez, M. M. Fogler, A. H. C. Neto, C. N. Lau, F. Keilmann, and D. N. Basov, *Gate-tuning of graphene plasmons revealed by infrared nano-imaging*, Nature **487**, 82–85 (2012).

[Fei15] A. Feist, K. E. Echternkamp, J. Schauss, S. V. Yalunin, S. Schäfer, and C. Ropers, *Quantum coherent optical phase modulation in an ultrafast transmission electron microscope*, Nature **521**, 200–203 (2015).

[Fox10] M. Fox, *Optical Properties of Solids*, 2nd ed., Oxford University Press, Oxford, 2010.

[Gam16] S. Gamage, Z. Li, V. S. Yakovlev, C. Lewis, H. Wang, S. B. Cronin, and Y. Abate, *Nanoscopy of Black Phosphorus Degradation*, Advanced Materials Interfaces **3**, 1600121 (2016).

[Gei13] A. K. Geim and I. V. Grigorieva, *Van der Waals heterostructures*, Nature **499**, 419–425 (2013).

[Gog82] V. V. Gogh, *Letters To Theo Van Gogh*, The Hague, Sunday, 22. Oct. (1882).

[Gon15] Y. Gong, A. G. Joly, D. Hu, P. Z. El-Khoury, and W. P. Hess, *Ultrafast Imaging of Surface Plasmons Propagating on a Gold Surface*, Nano Letters **15**, 3472–3478 (2015).

[Goo71] J. B. Goodenough, *The two components of the crystallographic transition in VO_2*, Journal of Solid State Chemistry **3**, 490–500 (1971).

[Gov13] A. A. Govyadinov, I. Amenabar, F. Huth, P. S. Carney, and R. Hillenbrand, *Quantitative Measurement of Local Infrared Absorption and Dielectric Function with Tip-Enhanced Near-Field Microscopy*, The Journal of Physical Chemistry Letters **4**, 1526–1531 (2013).

[Gov14] A. A. Govyadinov, S. Mastel, F. Golmar, A. Chuvilin, P. S. Carney, and R. Hillenbrand, *Recovery of Permittivity and Depth from Near-Field Data as a Step toward Infrared Nanotomography*, ACS Nano **8**, 6911–6921 (2014).

[Gri12] A. N. Grigorenko, M. Polini, and K. S. Novoselov, *Graphene plasmonics*, Nature Photonics **6**, 749–758 (2012).

[Gun00] M. K. Gunde, *Vibrational modes in amorphous silicon dioxide*, Physica B: Condensed Matter **292**, 286–295 (2000).

[Guo12] X. Guo, *Surface plasmon resonance based biosensor technique: A review*, Journal of Biophotonics **5**, 483–501 (2012).

[He14] K. He, N. Kumar, L. Zhao, Z. Wang, K. F. Mak, H. Zhao, and J. Shan, *Tightly Bound Excitons in Monolayer WSe_2*, Physical Review Letters **113**, 026803 (2014).

[Hes12] O. Hess, J. B. Pendry, S. A. Maier, R. F. Oulton, J. M. Hamm, and K. L. Tsakmakidis, *Active nanoplasmonic metamaterials*, Nature Materials **11**, 573–584 (2012).

[Hil02] R. Hillenbrand, T. Taubner, and F. Keilmann, *Phonon-enhanced light–matter interaction at the nanometre scale*, Nature **418**, 159–162 (2002).

[Hil07] D. J. Hilton, R. P. Prasankumar, S. Fourmaux, A. Cavalleri, D. Brassard, M. A. El Khakani, J. C. Kieffer, A. J. Taylor, and R. D. Averitt, *Enhanced Photosusceptibility near T_c for the Light-Induced Insulator-to-Metal Phase Transition in Vanadium Dioxide*, Physical Review Letters **99**, 226401 (2007).

[Hub01] R. Huber, F. Tauser, A. Brodschelm, M. Bichler, G. Abstreiter, and A. Leitenstorfer, *How many-particle interactions develop after ultrafast excitation of an electron–hole plasma*, Nature **414**, 286–289 (2001).

[Hub05] R. Huber, C. Kübler, S. Tübel, A. Leitenstorfer, Q. T. Vu, H. Haug, F. Köhler, and M.-C. Amann, *Femtosecond Formation of Coupled Phonon-Plasmon Modes in InP: Ultrabroadband THz Experiment and Quantum Kinetic Theory*, Physical Review Letters **94**, 027401 (2005).

[Hub08] A. J. Huber, B. Deutsch, L. Novotny, and R. Hillenbrand, *Focusing of surface phonon polaritons*, Applied Physics Letters **92**, 203104 (2008).

[Hub09] A. J. Huber, A. Ziegler, T. Köck, and R. Hillenbrand, *Infrared nanoscopy of strained semiconductors*, Nature Nanotechnology **4**, 153–157 (2009).

[Hub14] M. A. Huber, *Ultrafast terahertz nanoscopy with sub-cycle temporal resolution*, Master thesis, University of Regensburg (2014).

[Hub16] M. A. Huber, M. Plankl, M. Eisele, R. E. Marvel, F. Sandner, T. Korn, C. Schüller, R. F. Haglund, R. Huber, and T. L. Cocker, *Ultrafast Mid-Infrared Nanoscopy of Strained Vanadium Dioxide Nanobeams*, Nano Letters **16**, 1421–1427 (2016).

[Hub17] M. A. Huber, F. Mooshammer, M. Plankl, L. Viti, F. Sandner, L. Z. Kastner, T. Frank, J. Fabian, M. S. Vitiello, T. L. Cocker, and R. Huber, *Femtosecond photo-switching of interface polaritons in black phosphorus heterostructures*, Nature Nanotechnology **12**, 207–211 (2017).

[Huc16] C. Huck, J. Vogt, T. Neuman, T. Nagao, R. Hillenbrand, J. Aizpurua, A. Pucci, and F. Neubrech, *Strong coupling between phonon-polaritons and plasmonic nanorods*, Optics Express **24**, 25528 (2016).

[Jah15] J. Jahng, J. Brocious, D. A. Fishman, S. Yampolsky, D. Nowak, F. Huang, V. A. Apkarian, H. K. Wickramasinghe, and E. O. Potma, *Ultrafast pump-probe force microscopy with nanoscale resolution*, Applied Physics Letters **106**, 083113 (2015).

[Jia17] B.-Y. Jiang, G.-X. Ni, Z. Addison, J. K. Shi, X. Liu, S. Y. F. Zhao, P. Kim, E. J. Mele, D. N. Basov, and M. M. Fogler, *Plasmon Reflections by Topological Electronic Boundaries in Bilayer Graphene*, Nano Letters **17**, 7080–7085 (2017).

[Jon10] A. C. Jones, S. Berweger, J. Wei, D. Cobden, and M. B. Raschke, *Nano-optical Investigations of the Metal-Insulator Phase Behavior of Individual VO_2 Microcrystals*, Nano Letters **10**, 1574–1581 (2010).

[Kah14] P. Kahl, S. Wall, C. Witt, C. Schneider, D. Bayer, A. Fischer, P. Melchior, M. Horn-von Hoegen, M. Aeschlimann, and F.-J. Meyer zu Heringdorf, *Normal-Incidence Photoemission Electron Microscopy (NI-PEEM) for Imaging Surface Plasmon Polaritons*, Plasmonics **9**, 1401–1407 (2014).

[Kei04] F. Keilmann and R. Hillenbrand, *Near-field microscopy by elastic light scattering from a tip*, Philosophical Transactions of the Royal Society A: Mathematical, Physical and Engineering Sciences **362**, 787–805 (2004).

[Kim06] H.-T. Kim, Y. W. Lee, B.-J. Kim, B.-G. Chae, S. J. Yun, K.-Y. Kang, K.-J. Han, K.-J. Yee, and Y.-S. Lim, *Monoclinic and Correlated Metal Phase in VO_2 as Evidence of the Mott Transition: Coherent Phonon Analysis*, Physical Review Letters **97**, 266401 (2006).

[Kin09] A. Kinkhabwala, Z. Yu, S. Fan, Y. Avlasevich, K. Müllen, and W. E. Moerner, *Large single-molecule fluorescence enhancements produced by a bowtie nanoantenna*, Nature Photonics **3**, 654–657 (2009).

[Kir88] C. T. Kirk, *Quantitative analysis of the effect of disorder-induced mode coupling on infrared absorption in silica*, Physical Review B **38**, 1255–1273 (1988).

[Kit96] C. Kittel, *Introduction to Solid State Physics*, 7 ed., John Wiley & Sons, Inc., New York, Chichester, Brisbane, Toronto, Singapore, 1996.

[Kno99] B. Knoll and F. Keilmann, *Near-field probing of vibrational absorption for chemical microscopy*, Nature **399**, 134–137 (1999).

[Kre71] E. Kretschmann, *Die Bestimmung optischer Konstanten von Metallen durch Anregung von Oberflächenplasmaschwingungen*, Zeitschrift für Physik A Hadrons and Nuclei **241**, 313–324 (1971).

[Kru12] R. Krutokhvostov, A. A. Govyadinov, J. M. Stiegler, F. Huth, A. Chuvilin, P. S. Carney, and R. Hillenbrand, *Enhanced resolution in subsurface near-field optical microscopy*, Optics Express **20**, 593–600 (2012).

[Küb07] C. Kübler, H. Ehrke, R. Huber, R. Lopez, A. Halabica, R. F. Haglund, and A. Leitenstorfer, *Coherent Structural Dynamics and Electronic Correlations during an Ultrafast Insulator-to-Metal Phase Transition in VO_2*, Physical Review Letters **99**, 116401 (2007).

[Lai14] Y.-P. Lai, I.-T. Lin, K.-H. Wu, and J.-M. Liu, *Plasmonics in Topological Insulators*, Nanomaterials and Nanotechnology **4**, 13 (2014).

[Leo07] U. Leonhardt, *Optical metamaterials: Invisibility cup*, Nature Photonics **1**, 207–208 (2007).

[Li14] L. Li, Y. Yu, G. J. Ye, Q. Ge, X. Ou, H. Wu, D. Feng, X. H. Chen, and Y. Zhang, *Black phosphorus field-effect transistors*, Nature Nanotechnology **9**, 372–377 (2014).

[Li15] D. Li, H. Jussila, L. Karvonen, G. Ye, H. Lipsanen, X. Chen, and Z. Sun, *Polarization and Thickness Dependent Absorption Properties of Black Phosphorus: New Saturable Absorber for Ultrafast Pulse Generation*, Scientific reports **5**, 15899 (2015).

[Li16] P. Li, X. Yang, T. W. W. Maß, J. Hanss, M. Lewin, A.-K. U. Michel, M. Wuttig, and T. Taubner, *Reversible optical switching of highly confined phonon–polaritons with an ultrathin phase-change material*, Nature Materials **15**, 870–875 (2016).

[Lin15] X. Ling, H. Wang, S. Huang, F. Xia, and M. S. Dresselhaus, *The renaissance of black phosphorus*, Proceedings of the National Academy of Sciences **112**, 4523–4530 (2015).

[Liu13] M. K. Liu, M. Wagner, E. Abreu, S. Kittiwatanakul, A. McLeod, Z. Fei, M. Goldflam, S. Dai, M. M. Fogler, J. Lu, S. A. Wolf, R. D. Averitt, and D. N. Basov, *Anisotropic Electronic State via Spontaneous Phase Separation in Strained Vanadium Dioxide Films*, Physical Review Letters **111**, 096602 (2013).

[Liu14] M. Liu, M. Wagner, J. Zhang, A. McLeod, S. Kittiwatanakul, Z. Fei, E. Abreu, M. Goldflam, A. J. Sternbach, S. Dai, K. G. West, J. Lu, S. A. Wolf, R. D. Averitt, and D. N. Basov, *Symmetry breaking and geometric confinement in VO_2 : Results from a three-dimensional infrared nano-imaging*, Applied Physics Letters **104**, 121905 (2014).

[Liu15] M. Liu, A. J. Sternbach, M. Wagner, T. V. Slusar, T. Kong, S. L. Bud'ko, S. Kittiwatanakul, M. M. Qazilbash, A. McLeod, Z. Fei, E. Abreu, J. Zhang, M. Goldflam, S. Dai, G.-X. Ni, J. Lu, H. A. Bechtel, M. C. Martin, M. B. Raschke, R. D. Averitt, S. A. Wolf, H.-T. Kim, P. C. Canfield, and D. N. Basov, *Phase transition in bulk single crystals and thin films of VO_2 by nanoscale infrared spectroscopy and imaging*, Physical Review B **91**, 245155 (2015).

[Low14a] T. Low and P. Avouris, *Graphene Plasmonics for Terahertz to Mid-Infrared Applications*, ACS Nano **8**, 1086–1101 (2014).

[Low14b] T. Low, A. S. Rodin, A. Carvalho, Y. Jiang, H. Wang, F. Xia, and A. H. C. Neto, *Tunable optical properties of multilayer black phosphorus thin films*, Physical Review B **90**, 075434 (2014).

[Low17] T. Low, A. Chaves, J. D. Caldwell, A. Kumar, N. X. Fang, P. Avouris, T. F. Heinz, F. Guinea, L. Martin-Moreno, and F. Koppens, *Polaritons in layered two-dimensional materials*, Nature Materials **16**, 182–194 (2017).

[Mac09] K. F. MacDonald, Z. L. Sámson, M. I. Stockman, and N. I. Zheludev, *Ultrafast active plasmonics*, Nature Photonics **3**, 55–58 (2009).

[Mad04] O. Madelung, *Semiconductors: Data Handbook*, Springer Berlin Heidelberg, Berlin, Heidelberg, 2004.

[Mai07] S. A. Maier, *Plasmonics: Fundamentals and Applications*, Springer US, New York, New York, 2007.

[Mak10] K. F. Mak, C. Lee, J. Hone, J. Shan, and T. F. Heinz, *Atomically Thin MoS_2 : A New Direct-Gap Semiconductor*, Physical Review Letters **105**, 136805 (2010).

[Mie08] G. Mie, *Beiträge zur Optik trüber Medien, speziell kolloidaler Metallösungen*, Annalen der Physik **330**, 377–445 (1908).

[Mor59] F. J. Morin, *Oxides Which Show a Metal-to-Insulator Transition at the Neel Temperature*, Physical Review Letters **3**, 34–36 (1959).

[Mor86] A. Morita, *Semiconducting black phosphorus*, Applied Physics A Solids and Surfaces **39**, 227–242 (1986).

[Mor14] V. R. Morrison, R. P. Chatelain, K. L. Tiwari, A. Hendaoui, A. Bruhacs, M. Chaker, and B. J. Siwick, *A photoinduced metal-like phase of monoclinic VO_2 revealed by ultrafast electron diffraction*, Science **346**, 445–448 (2014).

[Mor18] Y. Morimoto and P. Baum, *Diffraction and microscopy with attosecond electron pulse trains*, Nature Physics **14**, 252–256 (2018).

[Nag12] J. Nag, R. F. Haglund, E. Andrew Payzant, and K. L. More, *Non-congruence of thermally driven structural and electronic transitions in VO_2*, Journal of Applied Physics **112**, 103532 (2012).

[Nag17] P. Nagler, M. V. Ballottin, A. A. Mitioglu, F. Mooshammer, N. Paradiso, C. Strunk, R. Huber, A. Chernikov, P. C. M. Christianen, C. Schüller, and T. Korn, *Giant magnetic splitting inducing near-unity valley polarization in van der Waals heterostructures*, Nature Communications **8**, 1551 (2017).

[Ni16] G. X. Ni, L. Wang, M. D. Goldflam, M. Wagner, Z. Fei, A. S. McLeod, M. K. Liu, F. Keilmann, B. Özyilmaz, A. H. C. Neto, J. Hone, M. M. Fogler, and D. N. Basov, *Ultrafast optical switching of infrared plasmon polaritons in high-mobility graphene*, Nature Photonics **10**, 244–247 (2016).

[Ni18] G. X. Ni, A. S. McLeod, Z. Sun, L. Wang, L. Xiong, K. W. Post, S. S. Sunku, B.-Y. Jiang, J. Hone, C. R. Dean, M. M. Fogler, and D. N. Basov, *Fundamental limits to graphene plasmonics*, Nature **557**, 530–533 (2018).

[Nik16] A. Y. Nikitin, E. Yoxall, M. Schnell, S. Vélez, I. Dolado, P. Alonso-González, F. Casanova, L. E. Hueso, and R. Hillenbrand, *Nanofocusing of Hyperbolic Phonon Polaritons in a Tapered Boron Nitride Slab*, ACS Photonics **3**, 924–929 (2016).

[Nov05] K. S. Novoselov, D. Jiang, F. Schedin, T. J. Booth, V. V. Khotkevich, S. V. Morozov, and A. K. Geim, *Two-dimensional atomic crystals*, Proceedings of the National Academy of Sciences **102**, 10451–10453 (2005).

[Nov06] L. Novotny and B. Hecht, *Principles of Nano-Optics*, 2 ed., Cambridge University Press, Cambridge, 2006.

[Ott68] A. Otto, *Excitation of nonradiative surface plasma waves in silver by the method of frustrated total reflection*, Zeitschrift für Physik A Hadrons and Nuclei **216**, 398–410 (1968).

[Par13] J. H. Park, J. M. Coy, T. S. Kasirga, C. Huang, Z. Fei, S. Hunter, and D. H. Cobden, *Measurement of a solid-state triple point at the metal–insulator transition in VO_2*, Nature **500**, 431–434 (2013).

[Pel08] M. Pelton, J. Aizpurua, and G. Bryant, *Metal-nanoparticle plasmonics*, Laser & Photonics Review **2**, 136–159 (2008).

[Ple14] G. Plechinger, J. Mann, E. Preciado, D. Barroso, A. Nguyen, J. Eroms, C. Schüller, L. Bartels, and T. Korn, *A direct comparison of CVD-grown and exfoliated MoS_2 using optical spectroscopy*, Semiconductor Science and Technology **29**, 064008 (2014).

[Pri17] K. E. Priebe, C. Rathje, S. V. Yalunin, T. Hohage, A. Feist, S. Schäfer, and C. Ropers, *Attosecond electron pulse trains and quantum state reconstruction in ultrafast transmission electron microscopy*, Nature Photonics **11**, 793–797 (2017).

[Qaz07] M. M. Qazilbash, M. Brehm, B.-G. Chae, P.-C. Ho, G. O. Andreev, B.-J. Kim, S. J. Yun, A. V. Balatsky, M. B. Maple, F. Keilmann, H.-T. Kim, and D. N. Basov, *Mott Transition in VO_2 Revealed by Infrared Spectroscopy and Nano-Imaging*, Science **318**, 1750–1753 (2007).

[Qia14] J. Qiao, X. Kong, Z.-X. Hu, F. Yang, and W. Ji, *High-mobility transport anisotropy and linear dichroism in few-layer black phosphorus*, Nature Communications **5**, 4475 (2014).

[Ras03] M. B. Raschke and C. Lienau, *Apertureless near-field optical microscopy: Tip–sample coupling in elastic light scattering*, Applied Physics Letters **83**, 5089–5091 (2003).

[Rod15] D. Rodrigo, O. Limaj, D. Janner, D. Etezadi, F. J. García de Abajo, V. Pruneri, and H. Altug, *Mid-infrared plasmonic biosensing with graphene*, Science **349**, 165–168 (2015).

[Ros13] J. S. Ross, S. Wu, H. Yu, N. J. Ghimire, A. M. Jones, G. Aivazian, J. Yan, D. G. Mandrus, D. Xiao, W. Yao, and X. Xu, *Electrical control*

of neutral and charged excitons in a monolayer semiconductor, Nature Communications **4**, 1474 (2013).

[Sal07] B. E. A. Saleh and M. C. Teich, *Fundamentals of Photonics*, 2 ed., John Wiley & Sons, Inc., Hoboken, New Jersey, 2007.

[Sch10] J. A. Schuller, E. S. Barnard, W. Cai, Y. C. Jun, J. S. White, and M. L. Brongersma, *Plasmonics for extreme light concentration and manipulation*, Nature Materials **9**, 193–204 (2010).

[Spe15] G. Spektor, A. David, G. Bartal, M. Orenstein, and A. Hayat, *Spin-patterned plasmonics: towards optical access to topological-insulator surface states*, Optics Express **23**, 32759 (2015).

[Ste18] P. Steinleitner, P. Merkl, A. Graf, P. Nagler, K. Watanabe, T. Taniguchi, J. Zipfel, C. Schüller, T. Korn, A. Chernikov, S. Brem, M. Selig, G. Berghäuser, E. Malic, and R. Huber, *Dielectric Engineering of Electronic Correlations in a van der Waals Heterostructure*, Nano Letters **18**, 1402–1409 (2018).

[Sti10] J. M. Stiegler, A. J. Huber, S. L. Diedenhofen, J. Gómez Rivas, R. E. Algra, E. P. A. M. Bakkers, and R. Hillenbrand, *Nanoscale Free-Carrier Profiling of Individual Semiconductor Nanowires by Infrared Near-Field Nanoscopy*, Nano Letters **10**, 1387–1392 (2010).

[Sun16] Z. Sun, D. N. Basov, and M. M. Fogler, *Adiabatic Amplification of Plasmons and Demons in 2D Systems*, Physical Review Letters **117**, 076805 (2016).

[Sur16] A. Surrente, A. A. Mitioglu, K. Galkowski, W. Tabis, D. K. Maude, and P. Plochocka, *Excitons in atomically thin black phosphorus*, Physical Review B **93**, 121405 (2016).

[Tre97] R. Trebino, K. W. DeLong, D. N. Fittinghoff, J. N. Sweetser, M. A. Krumbügel, B. A. Richman, and D. J. Kane, *Measuring ultrashort laser pulses in the time-frequency domain using frequency-resolved optical gating*, Review of Scientific Instruments **68**, 3277–3295 (1997).

[vdV02] N. C. J. van der Valk and P. C. M. Planken, *Electro-optic detection of subwavelength terahertz spot sizes in the near field of a metal tip*, Applied Physics Letters **81**, 1558–1560 (2002).

[Vit15] L. Viti, J. Hu, D. Coquillat, W. Knap, A. Tredicucci, A. Politano, and M. S. Vitiello, *Black Phosphorus Terahertz Photodetectors*, Advanced Materials **27**, 5567–5572 (2015).

[Vit16] L. Viti, J. Hu, D. Coquillat, A. Politano, W. Knap, and M. S. Vitiello, *Efficient Terahertz detection in black-phosphorus nano-transistors with selective and controllable plasma-wave, bolometric and thermoelectric response*, Scientific Reports **6**, 20474 (2016).

[Wag14a] M. Wagner, Z. Fei, A. S. McLeod, A. S. Rodin, W. Bao, E. G. Iwinski, Z. Zhao, M. Goldflam, M. Liu, G. Dominguez, M. Thiemens, M. M. Fogler, A. H. C. Neto, C. N. Lau, S. Amarie, F. Keilmann, and D. N. Basov, *Ultrafast and Nanoscale Plasmonic Phenomena in Exfoliated Graphene Revealed by Infrared Pump–Probe Nanoscopy*, Nano Letters **14**, 894–900 (2014).

[Wag14b] M. Wagner, A. S. McLeod, S. J. Maddox, Z. Fei, M. Liu, R. D. Averitt, M. M. Fogler, S. R. Bank, F. Keilmann, and D. N. Basov, *Ultrafast Dynamics of Surface Plasmons in InAs by Time-Resolved Infrared Nanospectroscopy*, Nano Letters **14**, 4529–4534 (2014).

[Wan15a] L. Wang and X. G. Xu, *Scattering-type scanning near-field optical microscopy with reconstruction of vertical interaction*, Nature Communications **6**, 8973 (2015).

[Wan15b] X. Wang, A. M. Jones, K. L. Seyler, V. Tran, Y. Jia, H. Zhao, H. Wang, L. Yang, X. Xu, and F. Xia, *Highly anisotropic and robust excitons in monolayer black phosphorus*, Nature Nanotechnology **10**, 517–521 (2015).

[Woe15] A. Woessner, M. B. Lundeberg, Y. Gao, A. Principi, P. Alonso-González, M. Carrega, K. Watanabe, T. Taniguchi, G. Vignale, M. Polini, J. Hone, R. Hillenbrand, and F. H. L. Koppens, *Highly confined low-loss plasmons*

in graphene–boron nitride heterostructures, Nature Materials **14**, 421–425 (2015).

[Woo14] J. D. Wood, S. A. Wells, D. Jariwala, K.-S. Chen, E. Cho, V. K. Sangwan, X. Liu, L. J. Lauhon, T. J. Marks, and M. C. Hersam, *Effective Passivation of Exfoliated Black Phosphorus Transistors against Ambient Degradation*, Nano Letters **14**, 6964–6970 (2014).

[Woo15] A. H. Woomer, T. W. Farnsworth, J. Hu, R. A. Wells, C. L. Donley, and S. C. Warren, *Phosphorene: Synthesis, Scale-Up, and Quantitative Optical Spectroscopy*, ACS Nano **9**, 8869–8884 (2015).

[Xia14] F. Xia, H. Wang, D. Xiao, M. Dubey, and A. Ramasubramaniam, *Two-dimensional material nanophotonics*, Nature Photonics **8**, 899–907 (2014).

[Yan15] J. Yang, R. Xu, J. Pei, Y. W. Myint, F. Wang, Z. Wang, S. Zhang, Z. Yu, and Y. Lu, *Optical tuning of exciton and trion emissions in monolayer phosphorene*, Light: Science & Applications **4**, e312 (2015).

[Yox15] E. Yoxall, M. Schnell, A. Y. Nikitin, O. Txoperena, A. Woessner, M. B. Lundeberg, F. Casanova, L. E. Hueso, F. H. L. Koppens, and R. Hillenbrand, *Direct observation of ultraslow hyperbolic polariton propagation with negative phase velocity*, Nature Photonics **9**, 674–678 (2015).

[Zew10] A. H. Zewail, *Four-Dimensional Electron Microscopy*, Science **328**, 187–193 (2010).

[Zha09a] H. Zhang, C.-X. Liu, X.-L. Qi, X. Dai, Z. Fang, and S.-C. Zhang, *Topological insulators in Bi_2Se_3, Bi_2Te_3 and Sb_2Te_2 with a single Dirac cone on the surface*, Nature Physics **5**, 438–442 (2009).

[Zha09b] T. Zhang, P. Cheng, X. Chen, J.-F. Jia, X. Ma, K. He, L. Wang, H. Zhang, X. Dai, Z. Fang, X. Xie, and Q.-K. Xue, *Experimental Demonstration of Topological Surface States Protected by Time-Reversal Symmetry*, Physical Review Letters **103**, 266803 (2009).

[Zha11] J. Zhang, C.-Z. Chang, Z. Zhang, J. Wen, X. Feng, K. Li, M. Liu, K. He, L. Wang, X. Chen, Q.-K. Xue, X. Ma, and Y. Wang, *Band structure engineering in $(Bi_{1-x}Sb_x)_2Te_3$ ternary topological insulators*, Nature Communications **2**, 574 (2011).

[Zha14] S. Zhang, J. Yang, R. Xu, F. Wang, W. Li, M. Ghufran, Y.-W. Zhang, Z. Yu, G. Zhang, Q. Qin, and Y. Lu, *Extraordinary Photoluminescence and Strong Temperature/Angle-Dependent Raman Responses in Few-Layer Phosphorene*, ACS Nano **8**, 9590–9596 (2014).

[Zyl75] A. Zylbersztejn and N. F. Mott, *Metal-insulator transition in vanadium dioxide*, Physical Review B **11**, 4383–4395 (1975).

Acknowledgements

This work would not have been completed without the support of many people who helped me in various ways along my path. I especially want to thank

- Prof. Dr. **Rupert Huber** for his supervision of my work, the strong direct interaction on the interpretation of the experimental results and great ideas for further studies as well as the helpful discussions on all physics-related topics.
- Dr. **Tyler L. Cocker** for the great teamwork at the near-field setup and the many discussions and corrections on our work in my masters and doctoral research.
- Dr. **Max Eisele** for the nice tutoring in my masters time, teaching me the basics of near-field microscopy together with Tyler and creating the ultrafast near-field microscope I worked with.
- **Markus Plankl** for his great companionship in the lab and as a friend.
- **Fabian Mooshammer** for the extensive help and physical discussions in the last two years of my thesis when we collaborated to track down the ultrafast excitation of the hybrid polariton.
- **Fabian Sandner** and **Lukas Z. Kastner** for joining the near-field gang and contributing to my projects as well as letting me tutor their bachelor and master thesis.
- Prof. Dr. **Miriam S. Vitiello** and her group for the great samples of indium arsenide nanowires and black phosphorus heterostructures which led to two publications.

- Prof. Dr. **Richard F. Haglund, Jr.** and **Robert E. Marvel** for the vanadium dioxide samples, which I studied in the beginning of my doctoral work.
- Prof. Dr. **Christian Schüller** and Prof. Dr. **Tobias Korn** for the good collaboration on the strained vanadium dioxide nanobeams.
- Dr. **Gregor Mussler**, Dr. **Matthias Kronseder**, Prof. Dr. **Dominique Bougeard**, Prof. Dr. **Christian Back** and **Anton Frank** for the very direct interaction and sample preparation for the measurements on topological insulators.
- Prof. Dr. **Jaroslav Fabian** and **Tobias Frank** for the collaboration and discussions on the black phosphorus dielectric function.
- Dr. **Fritz Wünsch** for his help regarding all EDP related issues, providing a platform to teach my programming courses and showing me the physics department before my studies started.
- **Martin Furthmeier** for his assistance and competent help regarding technical questions and in the design of new opto-mechanics and electronics for the setup.
- **Imke Gronwald** for her guidance in the chemistry lab, the quick design and fabrication of test samples and interesting complementary insights in the nanoworld using the scanning electron microscope.
- **Ulla Franzke** for her great help regarding all organizational and bureaucratic questions.
- **The whole team** at Rupert Huber's chair for the great atmosphere.
- **My family** for the great support without which I could not have managed to put such a strong focus on my scientific work.

Additionally, special thanks to
Fabian Mooshammer, Fabian Sandner, Philipp Faltermeier & Tyler L. Cocker
for proof-reading this thesis.